

Understanding Magnesium-ion Electrochemistry
through Modification of Lewis Acid/Base Pairs

By

Emily G. Nelson

A dissertation submitted in partial fulfillment
Of the requirements for the degree of
Doctor of Philosophy
(Chemistry)
in the University of Michigan
2015

Doctoral Committee

Associate Professor Bart M. Bartlett
Assistant Professor Charles W. Monroe
Professor Vincent L. Pecoraro
Assistant Professor Nathaniel Szymczak

The storage battery is, in my opinion, a catchpenny, a sensation, a mechanism for swindling the public by stock companies. The storage battery is one of those peculiar things which appeals to the imagination, and no more perfect thing could be desired by stock swindlers than that very selfsame thing. ...Just as soon as a man gets working on the secondary battery it brings out his latent capacity for lying.

Thomas Edison
The Electrician (London) 1883 pg. 329

© Emily G. Nelson 2015

To my family and Karen J. Muyskens

ACKNOWLEDGEMENTS

Edison was incorrect on the feasibility of the storage battery but not so on the desire to exaggerate or withhold results when reporting research which holds the possibility for far reaching applicability.

Hopefully there is no exaggeration, swindling, or lying in the pages to follow and for that I would like to thank my research advisor. You are an incredible teacher and I was blessed to have you in class as well as a mentor. In research you have always stressed the importance and necessity of allowing the data to speak for itself, even when it made no sense, depressingly showed a non-functioning system, and, perhaps most importantly, when it suggested something exciting this way comes. As a graduate student it seems impossible not to be somewhat emotionally invested in the research, and while I have a tendency to view my data with a pessimistic eye, you have always shown the importance of ensuring emotion did not cloud data interpretation, either for the positive or negative, and for that I am very grateful. Thank you for your support and guidance through the very tough early years and the slightly less tough later years. Also, thank you for allowing me the opportunity to spend a semester at Toyota, not only was it a valuable learning opportunity but also instilled a much greater sense of confidence in the scientific skills I have learned under your guidance.

Thank you to my committee members; Professor Pecoraro thank you for giving me my first experience in a graduate research and for your continued suggestions and feedback. Professor Szymczak thank you for your considerable feedback and assistance in the early days of proton reduction catalysis and your continued feedback since. Professor Monroe, thank for agreeing to be a late addition to my committee and for your input as I started the Mg-ion project and for the collaboration with your students, from whom I have learned much.

I owe a deep sense of gratitude to every member of the Bartlett lab. First, I would like to thank the postdocs: Andrea Geyer, Brendan Liddle, Yenting Kuo, and

Vinodkumar Etacheri, thank your help and guidance in all the different stages of my research. To my contemporaries and peers, you are a wonderful group I could not have asked for better people to work with for the last 5 years. You have made the lows bearable and celebrated the highs. Tanya, thank you so much for the early management of the lab (it would have been so tough without you) and for the early morning chats about research and life. You have given me great advice on a wide range of topics and I am not sure I would have chosen to stick it out were it not for you. Kayla, thanks for the wonderful years as your apartment and lab mate, thank you for the great conversations about science and life, for the laughs and the evenings of just hanging out. I could not have asked for a better comrade in the trenches. Joe, thank you for your creativity, passion for science, for all the laughs and support through everything. I am so glad we ended up as lab mates. Xiao, you are the best, thanks for all the fun and for all the assistance once I finally switched over to batteries just like you always said I should. Ben, thanks for being the best desk mate. Thank you for all the great questions and suggestions, you have been a great asset to the lab. Jimmy, thanks for being my last semester desk mate, for the talks, laughs, and making sure we made time for Angelo's breakfast, always condign retreats (#supereloquentlab). Charles, you are so very strange, but aren't we all, thanks for coming to "hang out" and for doing all my soldering. Frances and Sam, best of luck in the future, and Frances thanks for being my new morning companion. Adam, without your excitement and eagerness to learn about Mg battery chemistry this last year would not have been so much fun, thank you and good luck as you continue on. I also want to thank my undergrads Aaron and Scott, you guys have always made me smile and think, thanks for working and learning with me as the projects took their twists and turns. Michael, Ryan, Andrew, Mark, Scott T., Elayne, Joel, Kris and Wes; you can always make me smile, thanks for always keeping things fun and unpredictable. Josh, I have to give you a special thanks. You were the undergraduate who was in our lab the longest, it has been so much fun getting to know you and watching you "grow up" in the lab. I fondly remember the way you sang all the time and kept me up to date with the hit songs on the radio.

Thank you to everyone I meet at Toyota during my internship. Especially Rana and Oscar, thank you for all you taught me and all the advice you gave during that short semester, professionally and personally.

I would also like to thank Kathleen Nolta, Ginger Shultze and Mosato Koreeda, for your support and giving me great teaching opportunities. Thank you for giving me the opportunity to give full lectures and write my own lesson plans. Roy Wentz, thank you for your words of wisdom and taking the time to chat when I needed to think about anything except what was happening in lab. Thank you to rest of the chemistry staff; Anna, Margarita, Jon, Tracy, Liz, Cornelius, Pat, and the numerous other staff members who have assisted me throughout the years. A special thanks to the custodial ladies of floor 2, thanks for your kindness and dealing with me always being in the way.

Thank you to all the friends I have made outside of the Bartlett Lab; Amy Klepser, Evonne Koo, Alaina DeToma, Laura Thoma, Joey Braymer, Sabrina Peczonczyk, Jeremy Feldblyum, Sean Eddy, Junsi Gu, David Chow, Cameron Moore, Sameer Phadke, Chelsea Huff, Betsy Brown, Gulin Vardar, James Saraidaridis (SBox), and many more, thank you for the friendship, words of encouragement and advice.

Lastly, though definitely not least, I need to thank my family. Pater, you are the tops and I cannot thank you enough for the support you have given not just me, but all us kids though the fallout and beyond, none of what we have done would be possible without you. Thank you for all the eccentric questions and conversations on the weekends, I love you. Elliot, Whitney, Poppy, Sawyer, and all the extended family, thanks for the matrices, runs, listening ears, video games, swims, late night talks, late night movies, volleyball, beaches, and so much more. We have the best of times, thanks for everything.

TABLE OF CONTENTS

| | |
|---|-----------|
| DEDICATION..... | ii |
| ACKNOWLEDGEMENTS..... | iii |
| LIST OF SCHEMES..... | x |
| LIST OF FIGURES..... | xi |
| LIST OF TABLES..... | xvii |
| LIST OF ABBREVIATIONS..... | xviii |
| ABSTRACT..... | xix |
| | |
| CHAPTER 1 Introduction..... | 1 |
| 1.1 The Need for Sustainable Energy / Batteries..... | 1 |
| 1.2 Current Battery Technology..... | 1 |
| 1.3 Next Generation Battery Technology..... | 4 |
| 1.4 Magnesium-ion Batteries..... | 6 |
| 1.5 Cathode materials for Mg-ion Batteries..... | 7 |
| 1.6 Scope of this Thesis..... | 8 |
| 1.7 References..... | 8 |
| | |
| CHAPTER 2 Enhanced Oxidative Stability of non-Grignard Magnesium Electrolytes through Ligand Modification..... | 12 |
| 2.1 Introduction..... | 12 |
| 2.2 Synthesis and Characterization..... | 14 |
| 2.3 Electrochemical Performance..... | 21 |

| | |
|---|-----------|
| 2.4 Conclusion..... | 28 |
| 2.5 Experimental | 28 |
| 2.5.1 General considerations..... | 28 |
| 2.5.2 NMR Data..... | 29 |
| 2.5.3 X-ray Structure Determination for $C_{62}H_{82}Cl_2Mg_5O_{18}$ (CCDC # 962673)..... | 29 |
| 2.5.4 X-ray Structure Determination for $C_{31}H_{52}F_3O_7Mg_2AlCl_6$ (CCDC # 962674)... | 31 |
| 2.5.5 Electrochemistry | 32 |
| 2.5.6 Synthesis | 33 |
| 2.6 References | 33 |
| | |
| CHAPTER 3 Magnesium-ion Electrolyte Exhibiting Wide Potential Window and Reduced Stainless Steel Corrosion | 36 |
| 3.1 Introduction | 36 |
| 3.2 Results and Discussion..... | 37 |
| 3.3 Conclusion..... | 48 |
| 3.4 Experimental | 48 |
| 3.4.1 General Considerations..... | 48 |
| 3.4.2 Synthesis | 49 |
| 3.4.3 Electrochemistry | 49 |
| 3.5 X-ray Structure Determination for $C_{28}H_{42}O_6Mg_2Cl_2$ (CCDC # 999561)..... | 50 |
| 3.6 X-ray Structure Determination for $C_{60}H_{78}O_{12}Mg_4Cl_2$ (CCDC # 999562) | 51 |
| 3.7 References | 53 |
| | |
| CHAPTER 4 Surface and Electrochemical Characterization of Carbon Passivation Layer | 55 |
| 4.1 Introduction | 55 |

| | |
|---|-----------|
| 4.2 Results and Discussion | 56 |
| 4.3 Conclusion..... | 65 |
| 4.4 Experimental | 65 |
| 4.4.1 General Considerations..... | 65 |
| 4.4.2 Synthesis | 66 |
| 4.4.3 Electrochemistry | 66 |
| 4.5 References | 66 |
| CHAPTER 5 Molybdenum-Oxo Complex for Proton Reduction..... | 68 |
| 5.1 Introduction | 68 |
| 5.2 Results and Discussion..... | 69 |
| 5.3 Conclusion..... | 83 |
| 5.4 Materials and Methods | 84 |
| 5.4.1 General Considerations..... | 84 |
| 5.4.2 Synthesis of bis(2,2'-bipyridine) dioxomolybdenum (VI) $[\text{MoO}_2(\text{bpy})_2][\text{OH}]_2$, (1) | 84 |
| 5.4.3 Synthesis of bis(2,2'-bipyridine) oxomolybdenum (IV) $[\text{MoO}(\text{bpy})_2][\text{PF}_6]_2$, (2) | 84 |
| 5.4.4 Electrochemistry | 85 |
| 5.4.5 Mass Spectrometric analysis of electrolysis-cell headspace..... | 85 |
| 5.5 References | 85 |
| CHAPTER 6 Perspectives and Conclusion | 88 |
| 6.1 Introduction | 88 |
| 6.2 Perspectives..... | 88 |
| 6.2.1 Air Stable Electrolyte Systems | 88 |
| 6.2.2 Non-corrosive Electrolyte Systems..... | 89 |

| | |
|--|----|
| 6.2.3 Electrolyte/ Electrode Interfaces..... | 91 |
| 6.3 Conclusion..... | 92 |
| 6.4 References | 93 |

LIST OF SCHEMES

- Scheme 2.1** Decomposition mechanism of Grignard reagents in the presence of air and moisture..... 13
- Scheme 2.2** Proposed equilibrium reactions between substituted phenols and AlCl_3 . The top equation shows the reactants and products, the equilibrium steps are shown below. 19

LIST OF FIGURES

| | |
|---|----|
| Figure 1.1 Cartoon showing the general layout of a secondary Li-ion intercalation battery. | 3 |
| Figure 1.2 Capacities and reduction potentials of various metal anodes. | 5 |
| Figure 1.3 Elemental abundance in the Earth’s crust..... | 6 |
| Figure 2.1 X-ray crystal structure of $Mg_5Cl_2C_{62}H_{82}O_{18}$ crystallized from the $(MPMC)_2-AlCl_3/THF$ electrolyte solution. | 17 |
| Figure 2.2 X-ray crystal structures of the molecular ions $[Mg_2Cl_3(THF)_6]^+$ and $[(FMP)AlCl_3]^-$ crystallized from the $(FMPMC)_2-AlCl_3/THF$ electrolyte solution..... | 18 |
| Figure 2.3 Raman spectra of $(FMPMC)_2-AlCl_3/THF$ electrolyte. | 18 |
| Figure 2.4 ^{27}Al NMR spectra taken at 50, 25, 0, -20,-40,-60, and -80 °C. The identity of the peaks are labeled in the 50 °C spectra. | 19 |
| Figure 2.5 Van’t Hoff plot for the reaction between $AlCl_3$ and 4- CF_3 -PhMgCl. | 21 |
| Figure 2.6 Cyclic voltammograms of a) $(FMPMC)_2-AlCl_3/THF$, b) $(BPMC)_2-AlCl_3/THF$, c) $(PMC)_2-AlCl_3/THF$, d) $(BMPMC)_2-AlCl_3/THF$ e) $(MePMC)_2-AlCl_3/THF$, f) $(MPMC)_2-AlCl_3/THF$. The scan rate is 25 mV/s. The best previously reported electrolyte $[(2-tert-butyl-4-methyl-phenolate\ magnesium\ chloride)_2AlCl_3/THF, (BMPMC)_2AlCl_3/THF]^{\dagger}$ was prepared and is included below for comparison. The phenolate ligands and dashed lines are shown for clarity..... | 22 |
| Figure 2.7 Steady-state cyclic voltammogram of $(FMPMC)_2-AlCl_3/THF$ performed at a scan rate of 1 mV/s. | 23 |
| Figure 2.8 Hammett plot of para-substituted phenols vs oxidation onset potential of non-Grignard electrolytes..... | 24 |
| Figure 2.9 Hammett plot of anodic current at 3 V vs. $Mg^{2+/0}$ vs. σ^+ values of p-substituted phenols..... | 24 |
| Figure 2.10 Cyclic voltammograms of $(FMPMC)_2-AlCl_3/THF$ (—) and after (- - -) exposure to air for 6 hours. | 25 |

| | |
|---|----|
| Figure 2.11 ²⁷ Al NMR spectra of a.) APC electrolyte as synthesized top, and after 6 hour air exposure bottom b.) (FMPMC) ₂ -AlCl ₃ /THF electrolyte as synthesized top, and after 6 hour air exposure bottom. | 26 |
| Figure 2.12 Cyclic voltammograms of Pt electrodes in 0.5 M a) (FMPMC) ₂ -AlCl ₃ /THF and b) (PFPMC) ₂ -AlCl ₃ /THF solutions. The scan rate is 25 mV/s and the dashed line is added as a guide to the eye. | 26 |
| Figure 2.13 a) Reversible galvanostatic cycling of Mo ₆ S ₈ vs Mg-foil in 0.5 M (FMPMC) ₂ -AlCl ₃ /THF electrolyte at C/5. b) Discharge curves of Mo ₆ S ₈ vs. Mg-foil in (FMPMC) ₄ -AlCl ₃ /THF electrolyte. | 27 |
| Figure 2.14 ²⁷ Al NMR spectra of (FMPMC) ₂ -AlCl ₃ /THF a) before and b) after electrolysis at 3.5 V vs. Mg ^{2+/0} for 90 minutes. | 28 |
| Figure 3.1 CV scan of a solution of 0.5 M Al(OPh) ₃ /PhMgCl in THF on a Pt working electrode at a scan rate of 25 mV/s. Inset shows close up of oxidation potential..... | 37 |
| Figure 3.2 Charge balance of Mg deposition/stripping showing an ~98% coulombic efficiency..... | 38 |
| Figure 3.3 SEM and EDX of deposited Mg on Cu foil..... | 38 |
| Figure 3.4 Typical charge/discharge profiles for a rechargeable battery with Al (OPh) ₃ /PhMgCl in THF, a Mg anode, a WSe ₂ cathode at cycles 5 (black), 10 (red), 20 (blue), and 50 (green)..... | 39 |
| Figure 3.5 Typical charge/discharge profiles for a rechargeable battery with Al (OPh) ₃ /PhMgCl in THF, an Mg anode, a Mo ₆ S ₈ cathode at a rate of C/20 (10 μA/cm ²) cycles 1 (black), 2 (red), 10 (navy), 20 (olive), 40 (violet), 60 (orange), 80 (wine), and 100 (dark yellow). | 40 |
| Figure 3.6 SEM image of solid state synthesized WSe ₂ | 40 |
| Figure 3.7 Cyclic voltammogram of an electrolyte solution of 0.5 M Al(OPh) ₃ /PhMgCl in THF recorded on a 316 stainless steel micro-working electrode at a scan rate of 25 mV/s..... | 41 |
| Figure 3.8 SEM images of stainless steel a) before exposure to Mg electrolyte; b) after one CV cycle from 0 – 5.0 V in Al(OPh) ₃ /PhMgCl; c) after electrolysis at 4.5 V for 96 hours in Al(OPh) ₃ /PhMgCl; d) after one CV cycle from 0 – 4.0 V in APC; e) after | |

| | |
|--|----|
| electrolysis at 4.0 V for 24 hours in APC; f) after electrolysis at 4.0 V for 24 hours in APC..... | 42 |
| Figure 3.9 EDX map of stainless steel after CV cycling in APC | 43 |
| Figure 3.10 SEM images of stainless steel a) before and b) after cycling LiMn_2O_4 with 0.5 M $\text{Al}(\text{OPh})_3/\text{PhMgCl}$ in THF containing 0.5 M LiPF_6 for 100 cycles. | 43 |
| Figure 3.11 ^{27}Al NMR spectra of $\text{Al}(\text{OPh})_3/\text{PhMgCl}$ in THF giving one peak corresponding to $\text{Al}(\text{Ph})_4^-$ (131 ppm)..... | 44 |
| Figure 3.12 ^{13}C NMR spectrum of $\text{Al}(\text{OPh})_3/\text{PhMgCl}$ in THF; peak assignments are listed in Table 3-1. | 45 |
| Figure 3.13 Electrospray ionization mass spectra in negative ionization mode of $\text{Al}(\text{OPh})_3/\text{PhMgCl}$ giving $\text{Al}(\text{Ph})_4^-$ (m/z 335), upon magnification the following species are found: $\text{Al}(\text{Ph})_3\text{Cl}^-$ (294), $\text{Al}(\text{Ph})_3(\text{OPh})^-$ (352)..... | 46 |
| Figure 3.14 Electrospray ionization mass spectra positive ionization mode of $\text{Al}(\text{OPh})_3/\text{PhMgCl}$ giving the following species: $\text{Mg}_2\text{Cl}_3(\text{THF})_4^+$ (446), $\text{Mg}_2(\text{OPh})_3\text{Cl}(\text{THF})_2^+$ (508), $\text{Mg}_2\text{Cl}_3(\text{THF})_5^+$ (518) | 46 |
| Figure 3.15 One X-ray crystal structure of the neutral Mg species, $\text{C}_{28}\text{H}_{42}\text{Cl}_2\text{Mg}_2\text{O}_6$ isolated from a 1:4 $\text{Al}(\text{OPh})_3/\text{PhMgCl}$ electrolyte solution..... | 47 |
| Figure 3.16 Second X-ray crystal structure of the neutral Mg species, $\text{C}_{60}\text{H}_{78}\text{Cl}_2\text{Mg}_4\text{O}_{12}$ isolated from a 1:4 $\text{Al}(\text{OPh})_3/\text{PhMgCl}$ electrolyte solution..... | 47 |
| Figure 4.1 Open-circuit energy diagram of a battery system..... | 56 |
| Figure 4.2 a.) Al 2s XP spectra of Pt soaked in THF for 20 minutes; b.) Al 2s XP spectra of Pt after cycling 20 times in $\text{Al}(\text{OPh})_3:4\text{PhMgCl}$ electrolyte from 0-5V. | 57 |
| Figure 4.3 a.) Pt 4f XP spectra of Pt after cycling 20 times in $\text{Al}(\text{OPh})_3:4\text{PhMgCl}$ electrolyte from 0-5 V; b.) Pt 4f XP spectra of Pt soaked in THF for 20 minutes. | 57 |
| Figure 4.4 a.) C 1s XP spectra of Pt soaked in THF for 20 minutes, b.) C 1s XP spectra of Pt after cycling 20 times in $\text{Al}(\text{OPh})_3:4\text{PhMgCl}$ electrolyte from 0-5 V. | 58 |
| Figure 4.5 a.) C 1s XPS spectra of stainless steel soaked in THF for 20 minutes; b.) C 1s XPS spectra of stainless steel after cycling 20 times in $\text{Al}(\text{OPh})_3:4\text{PhMgCl}$ electrolyte from 0-5 V..... | 59 |
| Figure 4.6 CV trace of 0.5 M LiPF_6 with 0.5 M $\text{Al}(\text{OPh})_3/\text{PhMgCl}$ in THF..... | 59 |

| | |
|--|----|
| Figure 4.7 CV cycles of APC electrolyte with the addition of a.) benzene and b.) phenyl lithium with Mg foil counter and reference electrode, Pt working and scan rate of 25 mV/s..... | 60 |
| Figure 4.8 CV trace of 0.5 M PhMgCl in THF on a Pt electrode a) to 3 V and b) to 5V, the initial scan is shown in black, last scan in red, and middle scans in grey..... | 61 |
| Figure 4.9 Efficiency of Mg deposition and stripping from 0.5 M PhMgCl as the electrolyte is cycled from -1 to 5 V vs $\text{Mg}^{2+/0}$ | 62 |
| Figure 4.10 a.) CV curves of 0.5 M LiPF_6 added to 0.5 M PhMgCl after completing ten cycles prior to the addition of LiPF_6 b.) Coulombic efficiency of Mg deposition and stripping. | 63 |
| Figure 4.11 a.) CV trace of 0.5 M PhMgCl/ LiPF_6 in THF on a Pt electrode 5V, the initial scan is shown in black, last scan in red, and middle scans in grey b.) Coulombic efficiency of Mg deposition and stripping. | 63 |
| Figure 4.12 Typical charge/discharge profiles for a rechargeable battery with a LiMn_2O_4 cathode, 0.5 M $\text{Al}(\text{OPh})_3/\text{PhMgCl}$ in THF with 0.5 M LiPF_6 , a Mg anode at cycles 1 (black), 5 (red), and 20 (blue). | 64 |
| Figure 5.1 Infrared spectrum of $[(\text{bpy})_2\text{MoO}_2](\text{OH})_2$ (1) (gray) and $[(\text{bpy})_2\text{MoO}_2](\text{PF}_6)_2$ (2) (red). The Mo–O vibrational stretches for the dioxo and mono-oxo are noted. | 70 |
| Figure 5.2 Cyclic voltammogram of a 0.5 M solution of 2 in DMSO containing 0.1 M Bu_4NPF_6 using a scan rate of 50 mV/s with a 1 mm diameter glass carbon working electrode. The concentration of TsOH increases from 0 mM (black), 25 mM (blue) and 50 mM (red). Intermediate concentrations 0.5, 1, 2.5, 5, 12.5 mM are shown in gray with the final concentration of 62.5 mM shown in black, overlaying with 50 mM [TsOH].... | 71 |
| Figure 5.3 Plot of first reduction potential, $E_p/2$, versus pH of 0.5 mM (2) in DMSO with a scan rate of 0.5 mV/s. The linear least-squares fitted slope is 123 mV. | 72 |
| Figure 5.4 Cyclic voltammogram of a 0.5 mM 2 showing no change in behavior as NaOTs concentration is varied from 1 mM (black) to 25 mM (red). Overlapping traces in gray represent 2.5, 5, and 12.5 mM NaOTs..... | 73 |
| Figure 5.5 Background cyclic voltammetry of a TsOH solution in DMSO and electrolyte at a glassy carbon working electrode. The concentration of TsOH increases from 0 mM | |

| | |
|--|----|
| (black) to 50 mM (red) with intermediate concentrations 1, 5, and 10 mM shown in gray. | 74 |
| Figure 5.6 UV–Vis spectroelectrochemistry of 5 mM 2 in a solution of 0.1 M TBAPF ₆ in DMSO with 1.5 mmol tosic acid during the cathodic scan of a cyclic voltammogram with a scan rate of 10 mV/s with a mercury–gold mesh amalgam working electrode. Spectra were recorded every 10 second..... | 75 |
| Figure 5.7 DFT of 2 , showing large metal character in LUMO. | 75 |
| Figure 5.8 Proposed mechanism for reduction of H ⁺ to H ₂ by catalyst (2). | 76 |
| Figure 5.9 <i>i_c/i_p</i> vs. acid concentration of 0.1 mM 2 in a 0.1 M solution of TBAPF ₆ in DMSO..... | 78 |
| Figure 5.10 Rate of 2 in a solution of 0.1 M TBAPF ₆ in DMSO as a function of the catalyst concentration..... | 78 |
| Figure 5.11 Bulk electrolysis of 0.5 M 2 in solution of 0.1 M TBAPF ₆ and 50 mM TsOH in DMSO. Electrolysis was done at a potential of –1.8 V vs. Fc ⁺⁰ with a carbon felt working electrode, platinum mesh counter electrode and SCE reference electrode..... | 79 |
| Figure 5.12 Bulk electrolysis of 0.5 mM 1 (black), MoO ₂ (acac) ₂ (blue), and 2 (red) in solution of 0.1 M TBAPF ₆ and 50 mM TsOH in DMSO. Electrolysis was done at a potential of –1.8 V vs. Fc ⁺⁰ with a carbon felt working electrode, platinum mesh counter electrode and SCE reference electrode. | 80 |
| Figure 5.13 Hydrogen evolution over a 3 hour electrolysis of 0.5 mM 2 in a solution of 0.1 M TBAPF ₆ and 100 mM TsOH in DMSO. Electrolysis was done at a potential of –1.8 V vs. Fc ⁺⁰ with a carbon felt working electrode, platinum mesh counter electrode and SCE reference electrode. The red line shows the expected hydrogen evolution based on the charge passed during electrolysis..... | 80 |
| Figure 5.14 Infrared spectrum of tetrabutylammoniumcyanide (gray) and [(bpy) ₂ MoO ₂ CN](PF ₆) ₂ (3) (red). The C≡N vibrational stretches for the bound and unbound cyanide are noted. | 81 |
| Figure 5.15 Cyclic voltammogram of a 0.5 M solution of 3 in DMSO containing 0.1 M Bu ₄ NPF ₆ using a scan rate of 50 mV/s with a 1 mm diameter glass carbon working electrode. The concentration of TsOH increases from 0 mM (black), 25 mM (blue) and | |

50 mM (green). Intermediate concentrations 0.5, 1, 2.5, 5, 12.5 mM are shown in gray with the final concentration of 62.5 mM shown in red..... 82

Figure 5.16 Bulk electrolysis of 0.5 M **3** in solution of 0.1 M TBAPF₆ and 50 mM TsOH in DMSO. Electrolysis was done at a potential of -1.8 V vs. Fc⁺⁰ with a carbon felt working electrode, platinum mesh counter electrode and SCE reference electrode..... 83

LIST OF TABLES

| | |
|--|----|
| Table 2-1 ^{27}Al NMR assignments and shifts for $(\text{FMPMC})_x\text{-AlCl}_3/\text{THF}$ at various Lewis acid-to-base ratios..... | 15 |
| Table 2-2 ^{27}Al NMR assignments for 0.5 M electrolyte solutions..... | 16 |
| Table 2-3. Conductivity, voltage, anodic current, and Hammett σ^+ values for the substituted phenolate electrolyte complexes..... | 23 |
| Table 2-4 Crystal data and structure refinement for en5055 (CCDC # 962673) | 30 |
| Table 2-5 Crystal data and structure refinement for en51302a (CCDC # 962674) | 31 |
| Table 3-1 Summary of ^{13}C NMR spectra of $\text{Al}(\text{OPh})_3/\text{PhMgCl}$ electrolyte in THF. | 45 |
| Table 3-2 Crystal data and structure refinement for en52 (CCDC #999561) | 50 |
| Table 3-3 Crystal data and structure refinement for en5153 (CCDC # 999562) | 52 |

LIST OF ABBREVIATIONS

| | |
|-----------------|---|
| APC | Aurbach's all phenyl chloride electrolyte |
| BE | Bulk electrolysis |
| CV | Cyclic voltammetry |
| ES | Electron spray |
| HEV | Hybrid electric vehicle |
| HOMO | Highest occupied molecular orbital |
| LUMO | Lowest unoccupied molecular orbital |
| MS | Mass spectrometry |
| NHE | Normal hydrogen electrode |
| NMR | Nuclear magnetic resonance |
| PEV | Plug-in electric vehicle |
| XPS | X-ray photoelectron spectroscopy |
| μ_A | Anode electrochemical potential |
| μ_C | Cathode electrochemical potential |
| O _{Ph} | Phenolate |
| Ph | Phenyl |
| V | Voltage |

ABSTRACT

Lithium-ion batteries have long attracted attention for cultivation of portable energy storage devices. For larger portable applications such as hybrid electric or plug in vehicles the current Li-ion technology does not currently provide the power and energy required to meet the demands of these applications. Of the proposed post-Li ion technology, magnesium shows a good balance between redox potential, volumetric capacity, safety and abundance. This thesis focuses on electrolytes exhibiting high Mg-ion conductivity and analysis of how Lewis acid/ base pairings contribute to the physical and electrochemical properties of these electrolyte systems.

Early electrolytes capable of reversible Mg deposition and stripping contained Grignard components. Later, it was discovered the incorporation of a Lewis acid, commonly AlCl_3 , improved Mg deposition and stripping and oxidative stability. The presence of the Grignard in these electrolyte systems created safety concerns due to their flammability. Incorporating phenols in the place of the Grignard component has been shown to decrease unwanted reactivity towards air and moisture. To understand how para- substituted phenols contribute to the performance of the electrolyte, a series of non-Grignard electrolytes were synthesized. The increasing electron withdrawing ability of the para-substituent resulted in a shift of the anodic stability of the electrolyte by ~600 mV with para- CF_3 substituted phenolate exhibiting the highest stability of 2.9 V vs Mg. This stability is close to the oxidative stability of the common Grignard based electrolytes. The speciation of the electrolyte was examined using a number of spectroscopic techniques in an effort to infer relationships between the composition of the electrolyte and its electrochemical performance.

The commercialization of Mg battery technology is hindered by the presence of parasitic current on non-noble metal current collector. This electrochemical corrosion of the current collector by the high concentration of chloride ions. Removing the chloride from the Lewis acid resulted in an electrolyte with decreased detrimental corrosion on

stainless steel. This electrolyte also exhibits a surprisingly wide window of electrochemical stability, with electrolyte oxidation not occurring until ~ 5 V vs $\text{Mg}^{2+/0}$. This stability is attributed to the formation of an electrochemical quasi-passivation layer primarily composed of phenyl groups.

CHAPTER 1

Introduction

1.1 The Need for Sustainable Energy / Batteries

The global energy consumption in 2008 was estimated at 1.4 PWh and is predicted to rise by 40% in the next 25 years.¹ The total reserve of fossil fuels, such as coal and oil, is capable of generating 12.2 PWh. As a result, the world faces two main challenges on the energy frontier: shifting electricity production from burning fuel to sustainable sources, and moving ground transportation towards electrical propulsion. The transition away from fossil fuels as the main global energy source will bring diversification into alternative green energy sources; such as direct solar, thermal, hydroelectric, and wind energy capture. The shift will require the fostering of new high energy storage technologies able to compensate for the intermittent characteristics of alternative energy and provide constant power on demand, similar to that provided by the electrical grid driven by current energy sources.² Impressive progress has been seen in the genesis of technology for harvesting energy yet energy storage devices still lag behind. Batteries that can store energy with long term stability, prolonged cycle life, and environmental benignity is an important challenge for modern electrochemistry.³ The most convenient form of energy storage is portable chemical energy. Batteries provide the same portability of chemical energy as well as the ability to deliver stored energy in the form of electrical energy with high efficiency and without gaseous exhaust. Of particular interest is a battery consisting of low cost materials, safe, rechargeable (secondary), high voltage and capacity, and high rate capability.

1.2 Current Battery Technology

Primary commercial targets for rechargeable batteries are portable electronics, power tools, electric vehicles and stationary storage for grid applications. The first two of

these targets have been commercialized by the advent of Li-ion rechargeable batteries. The production of batteries for small electric vehicles (EV's) has received some commercial success with the Tesla, Nissan Leaf, and Chevy Spark, to name a few. Nonetheless, additional formulation is still required for safe, rechargeable batteries for larger EV's, vehicles with larger driving range, faster charge rates and lower cost. The implementation of stationary electrical energy storage for the grid also requires greater research and exploration.

Primary Li batteries first became a commercial reality during the 1970s. Attempts to actualize secondary Li batteries with Li-metal anodes received some near commercial production during the 1990s but most systems had inherent safety concerns, which prevented their large-scale use. The technological evolution that allowed for a safe, high energy density battery capable of commercial success was the replacement of the Li-metal anode with graphite and the use of lithiated transition metal oxide (LiMO_2) as a cathode material.⁴ The graphite- LiCoO_2 became the leading Li-ion battery system that currently powers most portable electronic devices such as cellular phones, laptops, digital cameras, etc.

Figure 1.1 shows the basic Li battery system prevalent in the current battery market. The main cell reactions are reversible Li-ion intercalation-de-intercalation cycles between the two layered compounds. The first process in the cell is charging, oxidation and delithiation of the cathode, in parallel to the reduction and lithiation of graphite. A battery converts chemical energy stored in its two electrodes (the anode is the reductant and the cathode is the oxidant) into a discharge electrical current $I=I_{\text{dis}}$ at a voltage $V=V_{\text{dis}}$ for a time $\Delta t=\Delta t_{\text{dis}}$, and a rechargeable battery restores the chemical energy by the application of a charging current I_{ch} at a voltage V_{ch} over a time Δt_{ch} . The capacity of a battery to deliver a current I_{dis} is the total amount of electrical current $Q(I)$ transported to the cathode over time Δt_{dis} for a complete discharge of the chemical energy available at I_{dis} . The resistances R_b of the working ion across the electrode/electrolyte interfaces, within the electrolyte, and within the electrodes result in a voltage loss $IR_b=\eta=V_{\text{OC}}-V$, where the open circuit potential $V_{\text{OC}}=(\mu_A-\mu_B)/e$ is the difference of the electrochemical potentials between the anode and cathode and e is the magnitude of the electrical charge. At $I=0$, transport of the ions inside the cell from the anode to the cathode is not compensated by

and external electronic charge. As a result a positive potential is created at the cathode and a negative potential at the anode until the internal electric field prevents flow of the working ion.⁵

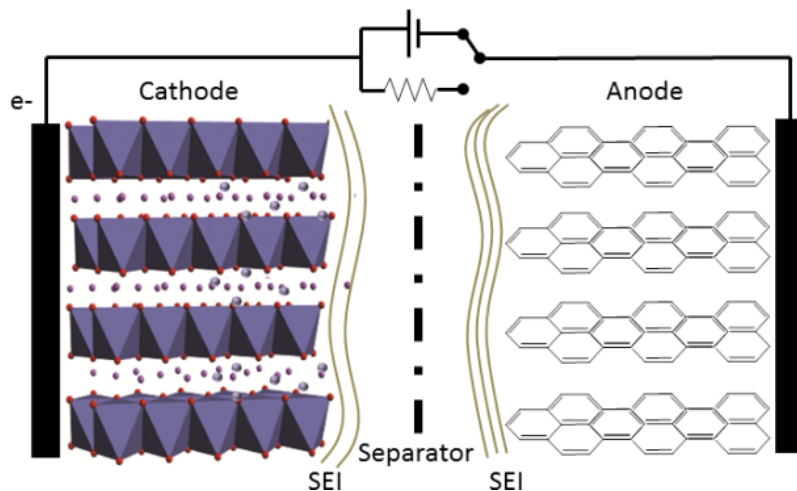


Figure 1.1 Cartoon showing the general layout of a secondary Li-ion intercalation battery.

A key issue related to the operation of Li-ion batteries is the choice of the electrolyte solutions. Carbonate solvents, mainly a mixture of ethylene carbonate (EC) and dimethyl carbonate (DMC), ethyl methyl carbonate (EMC) or diethyl carbonate (DEC), and LiPF_6 as the lithium salt is now considered the standard electrolyte solution for Li-ion batteries.^{6,7} When trace amounts of solvents are reduced, Li ions react with the products creating insoluble lithium compounds that precipitate on Li-metal, non-active metals or polarized carbon electrodes at low potentials. This forms thin surface films, or solid electrolyte interphase (SEI), that block electron transport but allow for continued Li-ion transport.^{8,9} The formation of the SEI serves as an effective passivation for both Li and fully lithiated graphite, allowing research to focus on more bothersome issues such as safety and increased energy density.

Safety concerns are related to the flammability of the electrolyte, the rate of charge and discharge, and the development of a short circuit due to lithium dendrite formation from repeated plating and stripping over the course of battery cycling. A greater energy density requires both a larger voltage (V) and larger charge-storage capacity (Q). To generate the required energy density to meet the energy demands of competitive EV's and grid electrical energy storage at an acceptable cost it will be necessary to move

beyond the present strategies. The exploration of inexpensive electrodes and electrolytes having long cycle life, and high capacity is a challenge for future research and will require imaginative material design.¹⁰

1.3 Next Generation Battery Technology

Post-lithium-ion batteries are considered batteries that hold the promise of a higher theoretical energy density than the existing lithium-ion batteries, containing a lithium metal oxide cathode and carbon anode, and have densities around 2000 Wh/L depending on the metal oxide. One route towards this end is replacing the graphite anode in current lithium ion batteries with a Li metal anode due to its high volumetric capacity (2060 Ah/L) and negative reduction potential of -3.04 V vs SHE. However, the inherent kinetic instability of lithium metal, especially during the charge cycle when lithium is redeposited on the anode at low overpotential, 0.2 V, creates safety concerns.¹¹⁻¹³ The tendency of lithium to redeposit in a dendritic morphology can result in short circuits, leading to internal heating and thermal runaway due to exothermic chemical reactions inside the battery. One approach to avoiding thermal runaway is the origination of new electrolytes or electrolyte additives to assist in a more uniform lithium deposition. These additives, such as chloro-silanes, -phosphanes, and -boranes work by forming a protective layer on the anode which appears to stabilize the electrochemical cycling of lithium.^{12,14,15}

Another alternative is to foster cathodes and anodes with higher capacities. Some high voltage lithium cathodes of great interest are sulfur and air cathodes. Sulfur has a theoretical capacity of 1672 mAh/g, and is a cheap, abundant material making it a promising alternative to metal oxide cathodes. Despite its promise, sulfur cathodes are plagued with a number of complications including low conductivity, large volume expansion of 80%, and rapid capacity fade. The low conductivity can be overcome with mixing the active sulfur with conductive substrates such as carbon, as is commonly done with the metal oxide cathodes. The rapid capacity fade is due to the generation of polysulfide anions upon the reduction of the cathode, which are soluble in the common carbonate solvents. The engineering of core-shell as well as other frameworks to

minimize this dissolution has met with some success, but often require rather complex, though very creative, synthetic steps.¹⁶

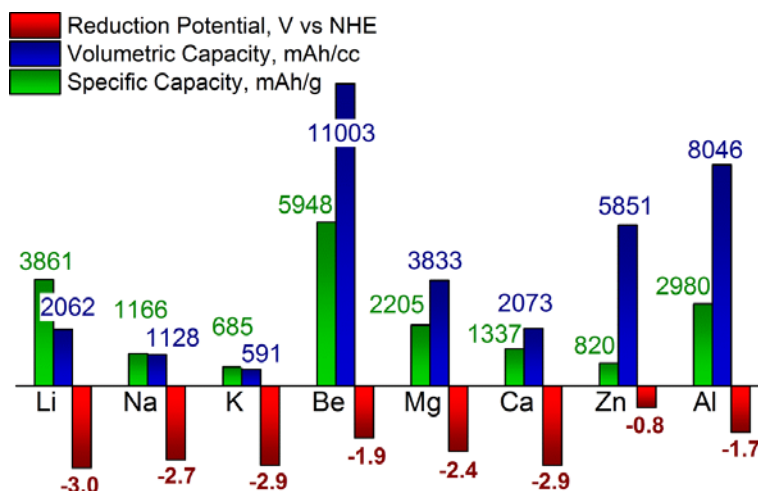


Figure 1.2 Capacities and reduction potentials of various metal anodes.

Another approach is the formulation of cathodes that undergo two electron chemistry on a single metal center.¹⁷⁻²⁰ This strategy would allow for a doubling of the capacity, but requires the insertion of two lithium atoms per metal site. The large volume expansion accompanying the insertion of two lithium atoms is a considerable complication for continued cultivation. This volume expansion can be minimized through the insertion of a single multivalent cation. Figure 1.2 shows the capacities and reductive potentials for some metal anodes which have been of interest for post-lithium ion batteries. Research has been done exploring many of these alternative metal ions. Aluminum and zinc give the promise of very high volumetric capacities, but suffer from reduction potentials that are much less negative than lithium. Magnesium, on the other hand, has a good balance between reduction potential, volumetric and gravimetric capacity and relative abundance in the earth's crust, Figure 1.3, and is the focus of this thesis.

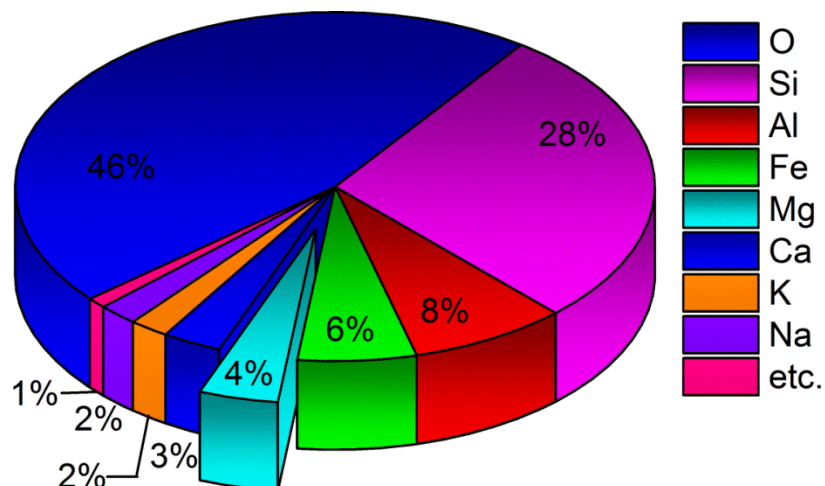


Figure 1.3 Elemental abundance in the Earth's crust.

1.4 Magnesium-ion Batteries

Magnesium possesses many characteristics that rank it as a propitious metal anode for high-density batteries. Its bivalency gives it a high theoretical volumetric capacity (3833 mAh/cm³), nearly double that of lithium. The standard reduction potential of -2.4 V vs NHE is slightly smaller than that of lithium at -3.0 V vs NHE, but is more negative than many other promising ions such as zinc (-0.8 V vs NHE) and aluminum (-1.7 V vs NHE). Magnesium is significantly less expensive (1/25th the cost of lithium) as well as more prevalent (5th most abundant metal in the earth's crust at 4%, compared to Li at 18 ppm). In addition, Mg is much easier to process than is Li, is more stable, and appears not to be plagued by dendrite formation upon cycling of the anode.²¹⁻²³

Despite these advantages, the cultivation of rechargeable magnesium ion battery technology has been limited by several bottlenecks, one of which is the preparation of a suitable electrolyte. Although lithium ion batteries work with carbonate based solvents, these solvents (as well as other polar aprotic solvents) form a passivating film on the magnesium surface that appear to prevent the conduction of Mg²⁺, preventing the reversible electrochemical deposition.

Successful Mg electrodeposition processes were first reported in Grignard reagents in ether solvents in the early part of the 20th century.^{24,25} However, these systems proved unusable for batteries due to poor oxidative stability.²⁵ The first breakthrough in the preparation of anodically stable, ion conducting electrolyte solution was demonstrated by

Gregory in 1990 with Mg salts based on organo-borate and organo-aluminate anions in ether solvents.^{26,27} These electrolyte systems were also explored with various metal oxide cathodes, including RuO₂ and Co₃O₄.

The second breakthrough took place a decade later, by Aurbach, with the synthesis of magnesium halo-alkyl aluminate complex compounds in ethereal solvents.²⁸ These electrolytes are synthesized *in situ* by mixing a R₂Mg Grignard reagent with a AlCl_{3-n}R_n Lewis acid. The optimized composition (AlCl₃-(PhMgCl)₂) exhibited an anodic stability to 3.3 V vs. Mg^{2+/0}.²⁹ However, these electrolytes are nucleophilic and quite sensitive to air and moisture due to the Grignard components (RMgX and MgR₂). These drawbacks decrease the likelihood of their adoption in battery production and exclude their potential application in next-generation Mg/S and Mg/O batteries.³⁰ The speciation in these electrolytes is quite complex, and the nature of the magnesium complex at the electrode during deposition is not well understood. Early work provided the hypothesis that the active Mg²⁺ deposition species is the magnesium dimer [Mg₂Cl₃(THF)₆]⁺, which is commonly crystallized from electrolyte solutions. This belief led to the main synthetic efforts that focus on chloride. However, recent work suggests this dimer is converted to another Mg²⁺ species prior to deposition.³¹ Although this intermediate species is unknown, creating electrolytes that do not require the dimer for reversible magnesium deposition has opened synthetic options towards more creative and diverse Mg electrolyte targets. Some of these new targets include the use of amine bases (Hauser bases), boron ligands (including borohydrides, carboranes, and phenylboranes), phenolates, alkoxides, as well as thiolates.³²⁻³⁶ Despite many of these electrolytes displaying impressive deposition and stripping coulombic efficiencies as well as oxidative stabilities, a commercial battery system has not yet been realized due to the absence of a viable cathode material for Mg-ion intercalation.

1.5 Cathode materials for Mg-ion Batteries

As mentioned earlier, some of the first work on Mg-ion cathodes was performed by Gregory *et al.* on simple binary metal oxides, sulfides and borides. The compounds Co₃O₄, Mn₂O₂, RuO₂, and ZrS₂ were found to be the most promising candidates from this report. Aurbach also published the use of the Chevrel phase of molybdenum sulfide

(Mo₆S₈) and showed excellent cyclability and low capacity fade over 1000 cycles. This material has since become the standard cathode used to determine the viability of any new magnesium electrolyte. The Chevrel Mo₆S₈, however, has a very low cycling voltage of ~1.7 V vs Mg^{2+/0}, limiting its use for higher energy density applications. Recent work in this area has produced some higher voltage cathode materials including WSe₂, V₂O₅, and MgFeSiO₄.³⁷⁻³⁹ Most research done to explore higher voltage materials are done in three electrode solution configurations instead of traditional battery testing configurations. This is due to the incompatibility of most electrolytes with stainless steel, a main component of battery current collecting systems. Additional fabrication of cathode materials will require the evolution of electrolytes with better stainless steel compatibility.

1.6 Scope of this Thesis

This thesis is focused on the production and characterization of Mg-ion conducting electrolytes for Mg battery applications by exploring various Lewis acid/base pairings. Chapter 2 presents the characterization of an electrolyte with decreased reactivity to air exposure synthesized through mixing magnesium phenolates with aluminum chloride. Chapter 3 presents the replacement of aluminum chloride with aluminum phenolates to generate an electrolyte with increased compatibility with stainless steel. This electrolyte also shows a very wide apparent oxidation potential of ~5 V vs Mg^{2+/0}. Chapter 4 focuses on exploring the nature and role of passivation layer formed in the presence of the PhMgCl/Al(OPh)₃ electrolyte. The surface of the electrodes were probed through XP spectroscopy and electrochemical methods. Electrolyte performance was measured quantitatively by the oxidative stability, efficiency of deposition and stripping reactions, as well as the solution conductivity. Chapter 5 is a departure, and discusses early work concerning the exploration of a molybdenum-oxo catalyst for the electrochemical reduction of protons from an organic solvent. Chapter 6 gives my outlook on the work done in this thesis as well as the current work in the field, along with my views on what continuing research will contribute greatest to the expansion of magnesium ion research.

1.7 References

- 1 Conti, J., Holtberg, P., *International Energy Outlook 2010*, U.S. Energy Information Administration, DOE/AIE-0484, **2011**
- 2 Armand, M, Tarascon, J. Building Better Batteries, *Nature*, **2008**, *451*, 652-657
- 3 Etacheri, V., Marom, R., Elazari, R., Salitra G., Aurach, D., Challenges in the Development of Advanced Li-Ion Batteries: A Review, *Energy Environ., Sci.*, **2011**, *11*, 3242-3262
- 4 Scrosati, B. *Electrochemistry of Novel Materials*, VCH Publishers, **1993**
- 5 Goodenough, J.B., Kim, Y. Challenges for Rechargeable Batteries, *Journal of Power Sources*, **2011**, *196*, 6688-6694
- 6 Guyomard, D., Tarascon, J.M. Li Metal-Free Rechargeable LiMn₂O₄/ Carbon Cells: Their Understanding and Optimization, *J. Electrochem. Soc.* **1992**, *139*, 937-948
- 7 Tarascon, J.M., McKinnon, W. R., Coowar, F., Bowner, T.N., Amatucci, G., Guyomard, D. Synthesis Conditions and Oxygen Stoichiometry Effects on Li Insertion into the Spinel LiMn₂O₄, *J Electrochem. Soc.*, **1994**, *141*, 1421-1431
- 8 Gabano, J.P., *Lithium Batteries*, Academic Press, London, **1983**
- 9 Balbuena, P.B., Wang, Y. *Lithium-Ion Batteries: Solid-Electrolyte Interphase*, Imperial College Press, **2004**
- 10 Goodenough, J.B., Kim, Y., Challenges for Rechargeable Li Batteries, *Chem. Mater.* **2010**, *22*, 587-603
- 11 Scrosati, B., Hassoun, J., Sun, Y.K. Lithium-ion Batteries: A Look into the Future, *Energy Environ. Sci.*, **2011**, *4*, 3287-3295
- 12 Crowther, O., West, A. C. Effect of Electrolyte Composition on Lithium Dendrite Growth, *J. Electrochem. Soc.*, **2008**, *155*, A806-A811
- 13 Xu, K. Nonaqueous Liquid Electrolytes for Lithium-Based Rechargeable Batteries, *Chem. Rev.*, **2004**, *104*, 4303-4418
- 14 Thompson, R. S., Schroeder, D. J., Lopez, C. M., Neuhold, S., Vaughey, J. T. Stabilization of Lithium Metal Anodes using Silane-Based Coatings, *Electrochemistry Communications*, **2011**, *13*, 1369-1372
- 15 Marchioni, F., Star, K., Menke, E., Buffeteau, T., Servant, L., Dunn, B., Wudl, F. Protection of Lithium Metal Surfaces Using Chlorosilanes, *Langmuir*, **2007**, *23*, 11597-11602
- 16 She, Z. W., Li, W., Cha, J. J., Zheng, G., Yang, Y., McDowell, M. T., Hsu, P. C., Cui, Y. Sulphur-TiO₂ Yolk-Shell Nanoarchitecture with Internal Void Space for Long-Cycle Lithium-Sulphur Batteries, *Nature Communications*, **2013**, *4*, 1331
- 17 Whittingham, M. S. Lithium Batteries and Cathode Materials, *Chem. Rev.*, **2004**, *104*, 4271-4302
- 18 Ellis, B. L., Makahnouk, W. T. M., Makimura, T., Toghiani, K., Nazar, L. F. A Multifunctional 3.5 V Iron-based Phosphate Cathode for Rechargeable Batteries, *Nat. Mater.*, **2007**, *6*, 749-753
- 19 Zhou, H., Upreti, S., Chernova, N. A., Hautier, G., Ceder, G., Whittingham, M. S. Iron and Manganese Pyrophosphates as Cathodes for Lithium-ion Batteries, *Chem. Mater.*, **2011**, *23*, 293-300
- 20 Islam, M. S., Dominko, R., Masquelier, C., Sirisopanaporn, C., Armstrong, A. T., Bruce, P. G. Silicate Cathodes for Lithium Batteries: Alternatives to Phosphates?, *J. Mater. Chem.*, **2011**, *21*, 9811-9818

- 21 Aurbach, D., Zinigrad, E., Cohen, Y., Teller, H. A Short Review of Failure Mechanisms for Lithium Metal and Lithiated Graphite Anodes in Liquid Electrolyte Solutions, *Solid State Ionics*, **2002**, *148*, 405-416
- 22 Gweraud, L., Grugeon, S., Laruelle, S., Yrieix, B., Tarascon, J. M. Lithium Metal Stripping/Plating Mechanism Studies: A Metallurgical Approach, *Electrochemistry Communications*, **2006**, *8*, 1639-1649
- 23 Yamaki, J., Tobishima, S., Hayashi, K., Saito, Keiichi, Nemoto, Y., Arakawa, M. J. A Consideration of the Morphology of Electrochemically Deposited Lithium in an Organic Electrolyte, *J. Power Sources*, **1998**, *74*, 219-227
- 24 Jolibois, P. Mg. Sur la Formule du Derive Organomagnésien et Sur L'hydrure de Magnésium, *C. R. Chim.*, **1912**, *155*, 353.
- 25 Gaddum, L. W., French, H. E. The Electrolysis of Grignard Solutions, *J. Am. Chem. Soc.*, **1927**, *49*, 1295-1299
- 26 Gregory, T.D., Hoffman, R.J., Winterton, R.C. Nonaqueous Electrochemistry of Magnesium Applications to Energy Storage, *J. Electrochem. Soc.*, **1990**, *137*, 775-780.
- 27 Genders, J. D., Pletcher, D. J. Studies using Microelectrodes of the Mg(II)/Mg Couple in Tetrahydrofuran and Propylene Carbonate, *J. Electroanal. Chem. Interfacial Electrochem.*, **1986**, *199*, 93-100
- 28 Aurbach, D., Lu, Z., Schechter, A., Gofer, Y., Gizbar, H., Turgeman, R., Cohen, Y., Moshkovich, M., Levi, E. Prototype Systems for Rechargeable Magnesium Batteries, *Nature*, **2000**, *407*, 724-727
- 29 Mizrahi, O., Amir, N., Pollak, E., Chusid, O., Marks, V., Gottlieb, H., Larush, L., Zinigrad, E., Aurbach, D. Electrolyte Solutions with a Wide Electrochemical Window for Rechargeable Magnesium Batteries, *J. Electrochem. Soc.* **2008**, *155*, A103-A109
- 30 Muldoon, J., Bucur, C. B., Oliver, A. G., Sugimoto, T., Matsui, M., Kim, H. S., Allred, G. D., Zajicek, J., Kotani, Y., Electrolyte Roadblocks to a Magnesium Rechargeable Battery, *Energy Environ. Sci.* **2012**, *5*, 5941-5950
- 31 Benmayza, A., Ramanathan, M., Arthur, T., Guo, J., Glans, P., Prakash, J. Effect of Electrolytic Properties of a Magnesium Organohaloaluminate Electrolyte on Magnesium Deposition, *J. Phys. Chem. C.*, **2013**, *117*, 26881-26888
- 32 Kim, H. S., Arthur, T. S., Allred, G. D., Zajicek, J., Newman, J. G., Rodnysansky, A. E., Oliver, A. G., Boggess, W. C., Muldoon, J. Structure and Compatibility of a Magnesium Electrolyte with a Sulphur Cathode, *Nat. Commun.*, **2011**, *2*, 427
- 33 Liebenow, C., Yang, Z., Lobitz, P. The Electrodeposition of Magnesium using Solutions of Organomagnesium Halides, Amidomagnesium Halides and Magnesium Organoborates, *Electrochemistry Communications* **2000**, *3*, 641-645
- 34 Mohtadi, R., Matsui, M., Arthur, T. S., Hwang, S. J. Magnesium Borohydride: From Hydrogen Storage to Magnesium Battery, *Angew. Chem., Int. Ed.*, **2012**, *51*, 9780-9783
- 35 Wang, F., Guo, Y., Yang, J., Nuli, Y., Hirano, S. A Novel Electrolyte System without a Grignard Reagent for Rechargeable Magnesium Batteries, *Chem. Commun.*, **2012**, *48*, 10763-10765
- 36 Guo, Y., Zhang, F., Yang, J., Wang, F., Nuli, Y., Hirano, S. Boron-based Electrolyte Solutions with Wide Electrochemical Windows for Rechargeable Magnesium Batteries, *Energy Environ. Sci.*, **2012**, *5*, 9100-9106

- 37 Orikasa, Y., Masese, T., Koyama, Y., Mori, T., Hattori, M., Yamamoto, K., Okado, T., Huang, Z. D., Minato, T., Tasse, C., Kim, J., Kobayashi, Y., Abe, T., Kageyama, H., Uchimoto, Y. High Energy Density Rechargeable Magnesium Battery using Earth-Abundant and Non-Toxic Elements, *Scientific Reports*, **2014**, *4*, 5622
- 38 Levi, E., Gofer, Y., Aurbach, D. On the Way to Rechargeable Mg Batteries: The Challenge of New Cathode Materials, *Chem. Mater.*, **2010**, *22*, 860-868
- 39 Liu, B., Luo, T., Mu, G., Wang, X., Chen, D., Shen, G., Rechargeable Mg-Ion Batteries Based on WSe₂ Nanowire Cathode, *ACS Nano*, **2013**, *7*, 8051-8058

CHAPTER 2

Enhanced Oxidative Stability of non-Grignard Magnesium Electrolytes through Ligand Modification

Portions of this chapter have been published:

Nelson, E. G.; Kampf, J. W.; Bartlett, B. M. *Chem. Commun.*, 2014, **50**, 5193-5195.

Reproduced by permission of the Royal Chemical Society

<http://pubs.rsc.org/en/content/articlelanding/2014/cc/c3cc47277a>

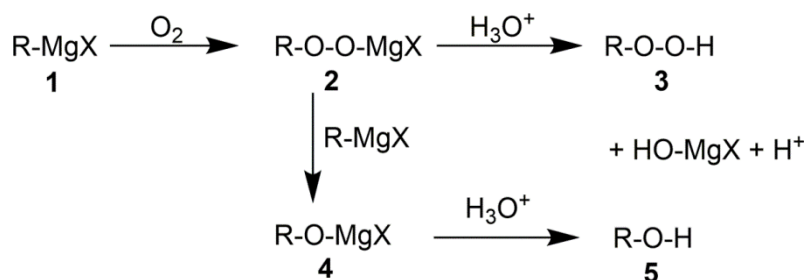
2.1 Introduction

One of the goals of this thesis is to increase the connection between electrochemical performance and the chemical species in solution. Mg-ion electrolyte chemistry is considerably more complex than Li-ion, due mostly to the fact that a simple Mg salt does not have all required electrochemical characteristics to perform as an electrolyte (mainly reversible Mg^0 deposition and high electrochemical oxidation potentials). Simple Li salts, most notably LiPF_6 , do show these properties, but working Mg electrolytes are usually comprised of Grignard based Lewis bases and aluminum Lewis acids. The downfall of this approach is in the use of Grignard reagents (EtMgCl , PhMgCl , ect.) which are pyrophoric. These compounds, coupled with the volatile solvent THF, in which most Mg-ion electrolytes are dissolved, increases the safety hazard associated with commercial implementation of these electrolyte systems. Grignard compounds are also nucleophilic. When electrolytes composed of Grignard compounds are coupled to high energy density cathodes such as sulfur or oxygen, unwanted chemical side reactions occur. For example, examining a sulfur cathode after cycling reveal the formation of phenylsulfide and diphenylsulfide byproducts.

One approach to solving the mismatch between electrolyte and cathode to use non-nucleophilic bases in electrolytes, such as Hauser bases. Compared to organomagnesium

compounds, Hauser bases, amide-magnesium halides, generally have higher oxidative stabilities because of the greater electronegativity of nitrogen. Due to this, Lobitz *et al.* suggested the use of hexamethyldisilazide magnesium chloride (HMDSMgCl) as an electrolyte. The electron rich Si-N-Si core was postulated to delocalize the electron pairs on the nitrogen and result in higher stability versus oxidation. However, the width of the electrochemical window of HMDSMgCl was only ~2.0 V.⁴⁰ Following the work of Aurbach, Muldoon and co-workers reacted the Lewis base precursor, HMDSMgCl, and the Lewis acid, AlCl₃, creating the non-nucleophilic electrolyte, [Mg₂Cl₃(THF)₆][HMDSAAlCl₃]. Purifying the complex by crystallization gave an electrolyte exhibiting a potential stability window of ~3.2 V. X-ray photoelectron spectroscopy analysis of a sulfur cathode after cycling with this electrolyte confirmed the electrochemical conversion between sulfur and magnesium sulfide was successfully performed.⁴¹ Analysis after cycling suggested the main cause of capacity fade was polysulfide or sulfur dissolution, which is a well-known hurdle in Li/S battery systems.^{42,43}

Another approach has been the incorporation of oxygen into the ligand in the electrolyte system. The decomposition of Grignard reagents in the presence of air and moisture is shown in Figure 2.1. Designing an electrolyte that starts with compound **4**, should yield an electrolyte with decreased reactivity to oxygen and atmospheric moisture.



Scheme 2.1 Decomposition mechanism of Grignard reagents in the presence of air and moisture.

Initial efforts in non-Grignard reagents based on phenolate Mg salts show good anodic stability to 2.6 V vs. Mg^{2+/0}, reversible Mg deposition-dissolution, and chemical compatibility with the Mo₆S₈ Chevrel-phase cathode.⁴⁴ The electrolyte also shows resistance to air/moisture decomposition as expected, with no loss in anodic stability after

stirring in air for 3 hours. The authors used three different phenol starting ligands, 2-tert-butyl-4-methylphenol, 2,6-ditert-butylphenol, and phenol, and acknowledge an influence of alkyl substituents on the electrochemical performance with the 2-tert-butyl-4-methylphenol based electrolyte exhibiting the best performance. They do not, however, provide a hypothesis or predictive model to guide new synthesis.

In this chapter, we build a model using physical organic chemistry and detailed characterization of solution speciation using NMR spectroscopy and mass spectrometry to elucidate the role of the ligand in enhancing electrochemical stability. We show that by increasing the electron withdrawing nature of the substituents, we can expand the electrochemical window of these air stable electrolytes by 400 mV, bringing them close to the wide stability window of air-sensitive Grignard-based electrolytes.

2.2 Synthesis and Characterization

A series of six ROMgCl salts were synthesized with various electron withdrawing and electron donating properties: [RO = 4-methoxy-phenolate (MPMC), phenolate (PMC), 4-methyl-phenolate (MePMC), 4-tert-butyl-phenolate (BPMC), 4-(trifluoromethyl)-phenolate (FMPMC), and pentafluorophenolate (PFPMC)] by reacting the appropriate phenols with the Grignard reagent, EtMgCl. These phenolate salts were then reacted with an AlCl₃-THF solution to form the electrolytes. The detailed synthesis is presented in Section 2.5.

Investigation of the electrolyte solution by multinuclear NMR spectroscopy shows a mixture of complexes is present in a dynamic equilibrium, as previously reported for aluminum alkoxides.^{45,46} The solution speciation and structures are determined by combining ¹H, ¹³C, ¹⁹F, and ²⁷Al NMR spectroscopy, (¹H,¹³C, and ¹⁹F NMR data is presented in Section 2.5). ¹H,¹³C, and ¹⁹F spectra were not as useful for determination of the components in solution due to similar shifts of the compounds and overlapping peaks, so ²⁷Al NMR spectra was used for determination of symmetry and binding environment of the molecular species.⁴⁷

Table 2-1 ^{27}Al NMR assignments and shifts for $(\text{FMPMC})_x\text{-AlCl}_3/\text{THF}$ at various Lewis acid-to-base ratios.

| Solution | Peak Shift (ppm) | Assignment |
|----------------------------------|------------------|--|
| 4:1 FMPMC–AlCl ₃ /THF | 51 | (FMP) ₄ Al |
| 2:1 FMPMC–AlCl ₃ /THF | 51 | (FMP) ₄ Al |
| | 62 | (FMP) ₃ AlCl ⁽⁻⁾ /(FMP) ₃ Al |
| | 74 | (FMP) ₂ AlCl ₂ ⁽⁻⁾ /(FMP) ₂ AlCl |
| | 88 | (FMP)AlCl ₃ ⁽⁻⁾ /(FMP)AlCl ₂ |
| | 102 | Al ₂ Cl ₆ |
| 3:2 FMPMC–AlCl ₃ /THF | 51 | (FMP) ₄ Al |
| | 62 | (FMP) ₃ AlCl ⁽⁻⁾ /(FMP) ₃ Al |
| | 74 | (FMP) ₂ AlCl ₂ ⁽⁻⁾ /(FMP) ₂ AlCl |
| | 87 | (FMP)AlCl ₃ ⁽⁻⁾ /(FMP)AlCl ₂ |
| | 91 | (FMP) ₂ Al ₂ Cl ₄ |
| | 102 | Al ₂ Cl ₆ |
| 1:4 FMPMC–AlCl ₃ /THF | 63 | AlCl ₃ |
| | 91 | (FMP) ₂ Al ₂ Cl ₄ |
| | 102 | Al ₂ Cl ₆ |
| AlCl ₃ /THF | 62 | AlCl ₃ |
| | 102 | Al ₂ Cl ₆ |

In an effort to assign the ^{27}Al NMR spectra of the as-synthesized electrolyte, a series of solutions comprised of differing ratios between the Lewis acid (AlCl_3) and base (FMPMC) was prepared. At high base-to-acid ratios, the main solution species should be the tetrakisphenolate $[\text{Al}(\text{FMP})_4]^-$. Accordingly, the NMR spectrum of $(\text{FMPMC})_4\text{-AlCl}_3/\text{THF}$ shows a single sharp peak at 51 ppm (referenced to AlCl_3 in HCl), expected for the tetrahedral anion and has a very similar shift to independently synthesized $\text{Li}[\text{Al}(\text{FMP})_4]^-$ which shows up at 50.42 ppm. As the ratio of base to acid decreases, three additional broader peaks are observed at 60, 73, and 86 ppm. These peaks are attributed to a sequential loss of ligand, $\text{Al}(\text{FMP})_3\text{Cl}$, $\text{Al}(\text{FMP})_2\text{Cl}_2^-$, and $\text{Al}(\text{FMP})\text{Cl}_3^-$ respectively. These spectra also exhibited a sharp peak at 102 ppm, which was assigned as Al_2Cl_6 and used as an internal standard.⁴⁸ At high acid-to-base ratios of the electrolyte $[(\text{FMPMC})\text{-}(\text{AlCl}_3)_4/\text{THF}]$, the spectra show the expected AlCl_3 peak at 63 ppm and a second sharp peak at 91 ppm. The sharpness of the 91 ppm peak suggests that aluminum is

tetrahedrally coordinated, while its upfield shift with respect to the dimer Al_2Cl_6 (102 ppm) suggests an increased number of organic ligands and so the 91 ppm shift is assigned to $\text{Al}_2(\text{FMP})_2\text{Cl}_4$. The similarity in shift to $\text{Al}(\text{FMP})\text{Cl}_3^-$ (86 ppm) supports the assignment of a single organic ligand on each metal center, and such organochloroaluminate dimers have been previously reported.⁴⁹ A complete table of ^{27}Al NMR shifts at the differing acid base ratios and their assignments are presented in Table 2-1.

Table 2-2 ^{27}Al NMR assignments for 0.5 M electrolyte solutions.

| Solution | Peak Shift (ppm) | Assignment |
|---|------------------|---|
| $(\text{FMPMC})_2\text{-AlCl}_3/\text{THF}$ | 51 | $(\text{FMP})_4\text{Al}$ |
| | 62 | $(\text{FMP})_3\text{AlCl}^{(-)}/(\text{FMP})_3\text{Al}$ |
| | 74 | $(\text{FMP})_2\text{AlCl}_2^{(-)}/(\text{FMP})_2\text{AlCl}$ |
| | 88 | $(\text{FMP})\text{AlCl}_3^{(-)}/(\text{FMP})\text{AlCl}_2$ |
| | 102 | Al_2Cl_6 |
| $(\text{PMC})_2\text{-AlCl}_2/\text{THF}$ | 60 | $(\text{P})_3\text{AlCl}^{(-)}/(\text{P})_3\text{Al}$ |
| | 73 | $(\text{P})_2\text{AlCl}_2^{(-)}/(\text{P})_2\text{AlCl}$ |
| | 86 | $(\text{P})\text{AlCl}_3^{(-)}/(\text{P})\text{Al}_2$ |
| | 102 | Al_2Cl_6 |
| $(\text{MPMC})_2\text{-AlCl}_3/\text{THF}$ | 71 | $(\text{MP})_2\text{AlCl}_2^{(-)}/(\text{MP})_2\text{AlCl}$ |
| | 87 | $(\text{MP})\text{AlCl}_3^{(-)}/(\text{MP})\text{AlCl}_2$ |
| | 102 | Al_2Cl_6 |
| $(\text{BPMC})_2\text{-AlCl}_3/\text{THF}$ | 72 | $(\text{BP})_2\text{AlCl}_2^{(-)}/(\text{BP})_2\text{AlCl}$ |
| | 86 | $(\text{BP})\text{AlCl}_3^{(-)}/(\text{BP})\text{AlCl}_2$ |
| | 102 | Al_2Cl_6 |
| $(\text{MePMC})_2\text{-AlCl}_3/\text{THF}$ | 71 | $(\text{MeP})_2\text{AlCl}_2^{(-)}/(\text{MeP})_2\text{AlCl}$ |
| | 87 | $(\text{MeP})\text{AlCl}_3^{(-)}/(\text{MeP})\text{AlCl}_2$ |
| | 102 | Al_2Cl_6 |
| $(\text{PFPMC})_2\text{-AlCl}_3/\text{THF}$ | 45 | $(\text{PFP})_4\text{Al}$ |
| | 60 | $(\text{PFP})_3\text{AlCl}^{(-)}/(\text{PFP})_3\text{Al}$ |
| | 74 | $(\text{PFP})_2\text{AlCl}_2^{(-)}/(\text{PFP})_2\text{AlCl}$ |
| | 88 | $(\text{PFP})\text{AlCl}_3^{(-)}/(\text{PFP})\text{AlCl}_2$ |
| | 102 | Al_2Cl_6 |

With this understanding of the ^{27}Al NMR spectra, the solution speciation of the as synthesized electrolytes can be determined. The electron-withdrawing complexes

(FMPMC)₂-AlCl₃/THF and (PFPMC)₂-AlCl₃/THF show the greatest number of species in solution, with the tetrakis-to-mono- ligated aluminium species present in both electrolytes. The remaining electrolytes do not show the tetrakis-ligated aluminium species. The ²⁷Al NMR spectrum of the most electron-donating complex (MPMC)₂-AlCl₃/THF shows only the bis- and mono-ligated complexes in smaller intensities relative to the Al₂Cl₆ species (Table 2-2).

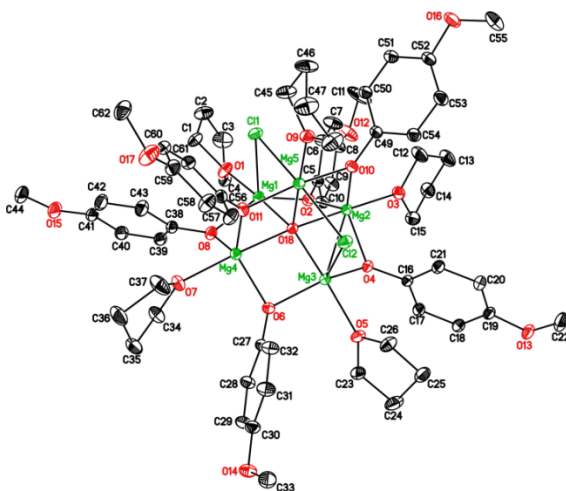


Figure 2.1 X-ray crystal structure of Mg₅Cl₂C₆₂H₈₂O₁₈ crystallized from the (MPMC)₂-AlCl₃/THF electrolyte solution.

One possible explanation for this observation is the ligand exchange between MPMC and AlCl₃ is slower or incomplete. Allowing the mixture to stir for an additional 24 hours, however, results in no difference in the NMR spectra. The X-ray crystal structure of the compound crystallized from (MPMC)₂-AlCl₃/THF (Figure 2.2) further supports incomplete ligand exchange, with a Mg cubane-like structure with bridging methoxyphenolate ligands. The electron-donating substituent may increase the softness of the phenolate base enough to lower the affinity for the hard Lewis acid AlCl₃, resulting in this crystal structure and incomplete ligand exchange.

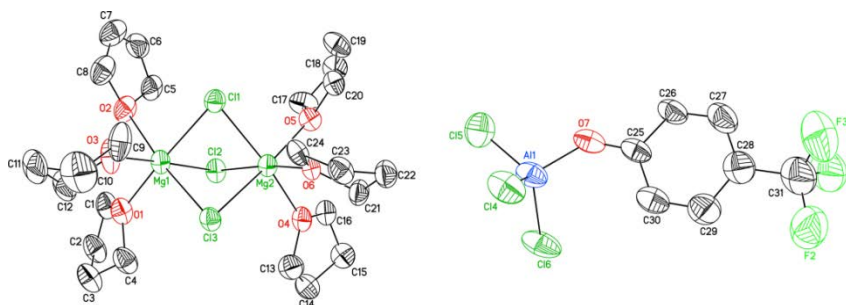


Figure 2.2 X-ray crystal structures of the molecular ions $[\text{Mg}_2\text{Cl}_3(\text{THF})_6]^+$ and $[(\text{FMP})\text{AlCl}_3]^-$ crystallized from the $(\text{FMPMC})_2\text{-AlCl}_3/\text{THF}$ electrolyte solution.

In contrast, the X-ray crystal structure of $(\text{FMPMC})_2\text{-AlCl}_3/\text{THF}$ shows the expected ligand exchange reaction forming $[\text{Mg}_2\text{Cl}_3(\text{THF})_6]^+$ cation and $[(\text{FMP})\text{AlCl}_3]^-$ anion (Figure 2.3). The ^{27}Al NMR assignments are supported by the mass spectrometry and by Raman spectra (assignments based on prior work^{50–52} and are presented in Figure 2.3).

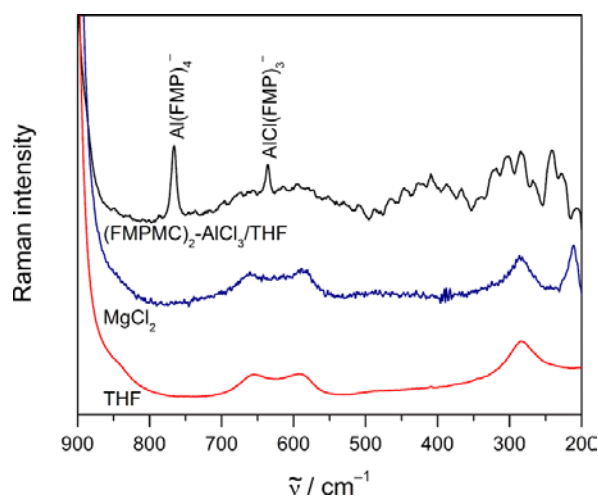


Figure 2.3 Raman spectra of $(\text{FMPMC})_2\text{-AlCl}_3/\text{THF}$ electrolyte.

The presence of multiple species in the ^{27}Al NMR spectrum and the crystallization of only one of the solution species bring up the possibility of the presence of equilibrium in solution between the aluminium complexes.

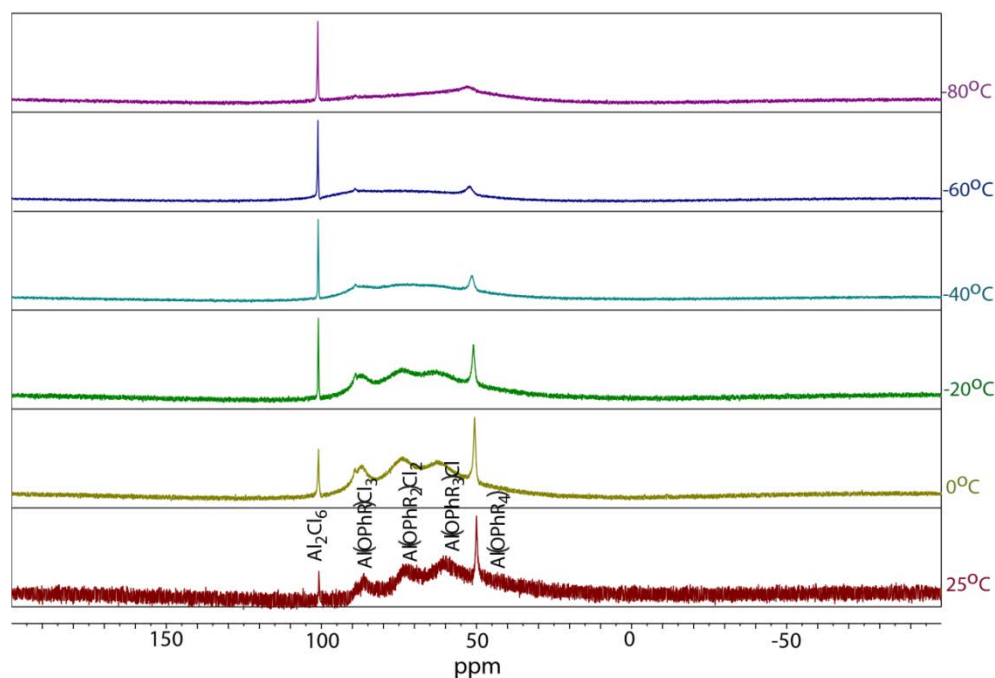
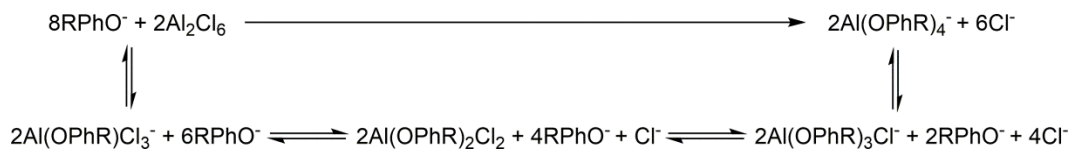


Figure 2.4 ^{27}Al NMR spectra taken at 50, 25, 0, -20, -40, -60, and -80 °C. The identity of the peaks are labeled in the 50 °C spectra.

To test the possibility of a thermodynamic equilibrium, ^{27}Al NMR spectra were recorded at various temperatures to determine if a shift in the species concentration was observed, illustrated for a 0.5 M (FMPMC) $_2$ - AlCl_3 /THF solution in Figure 2.5. As the temperature decreases the intensity of the mixed phenolate/ chloride aluminium complex peaks ($[(\text{FMP})\text{AlCl}_3]^-$, $[(\text{FMP})_2\text{AlCl}_2]^-$ and $[(\text{FMP})_3\text{AlCl}]^-$) also decrease and the Al_2Cl_6 and $[(\text{FMP})_4\text{Al}]^-$ peaks increase. The peak corresponding to $[(\text{FMP})_4\text{Al}]^-$ also shows a large peak broadening at lower temperatures which is a result of increased interaction with the solvent THF molecules.



Scheme 2.2 Proposed equilibrium reactions between substituted phenols and AlCl_3 . The top equation shows the reactants and products, the equilibrium steps are shown below.

At low temperatures, the only species observable in ^{27}Al NMR spectra are the Al_2Cl_6 and $[(\text{FMP})_4\text{Al}]^-$, which suggests the overall equilibrium takes place between FMP, Al_2Cl_6 and $[(\text{FMP})_4\text{Al}]^-$.

Adding an internal standard allows for integrating the ^{27}Al NMR spectrum and calculating the equilibrium constant at various temperatures. To ensure that the standard chosen, $\text{Li}(\text{AlPh}_4)$, was unreactive towards the aluminium complexes of interest, solutions of AlCl_3 , $\text{Li}(\text{AlOPh}_4)$, and the electrolyte were mixed with $\text{Li}(\text{AlPh}_4)$ for a week to verify there was no change in relative intensities of the species.

$$\Delta G = \Delta H - T\Delta S \quad (2-1)$$

$$\Delta G = -RT\ln(K_{eq}) \quad (2-2)$$

Combining the definition of Gibbs free energy (eq. 2-1), where S is the entropy of the system and H is enthalpy, and the Gibbs free energy isotherm (eq. 2-2), where R is the gas constant, gives the Van't Hoff equation (eq. 2-3).

$$\ln K_{eq} = \frac{-\Delta H}{R} \frac{1}{T} + \frac{\Delta S}{R} \quad (2-3)$$

Plotting the natural log of the equilibrium constant vs the inverse temperature gives the plot shown in Figure 2.6. The slope of the line, when multiplied by the gas constant, gives the standard enthalpy change of the reaction, and the intercept, also when multiplied by R , gives the standard entropy change for the reaction. The negative slope shows the reaction is endothermic, with a ΔH of 5.8 kJ/mol, and a ΔS of 1.91 J/mol.

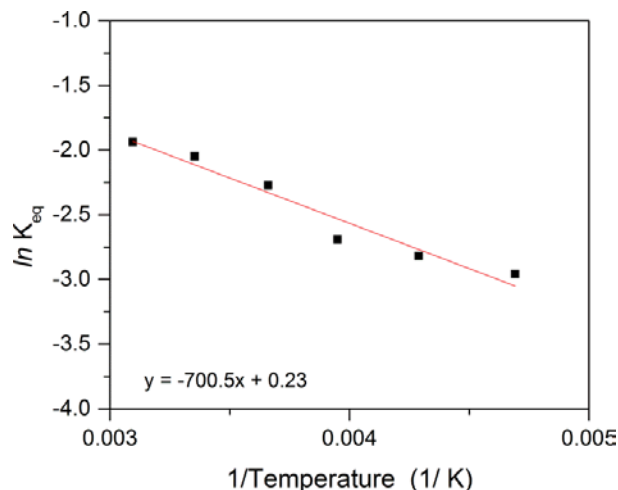


Figure 2.5 Van't Hoff plot for the reaction between AlCl_3 and 4- CF_3 -PhMgCl.

2.3 Electrochemical Performance

Initial electrochemical chemical characterization of electrolytes is done with cyclic voltammetry (CV) to determine oxidative stability and verify the electrolyte shows reversible magnesium deposition and stripping. Figure 2.6 presents the cyclic voltammograms of the synthesized phenolate electrolytes at a scan rate of 25 mV/s. The voltammogram of $(\text{FMPMC})_2\text{-AlCl}_3/\text{THF}$ is also recorded under near steady-state conditions (scan rate of 1 mV/s) Figure 2.7, and no new features emerged. Reversible Mg deposition-dissolution is observed for all electrolytes with the exception of $(\text{MPMC})_2\text{-AlCl}_3/\text{THF}$. The irreversibility of the $(\text{MPMC})_2\text{-AlCl}_3/\text{THF}$ electrolyte may be due to the incomplete ligand exchange and the formation of the cubane type structure (Figure 2.1). The anodic stability of the solutions (shown in Table 2-3) ranks as: $(\text{FMPMC})_2\text{-AlCl}_3/\text{THF} > (\text{BPMC})_2\text{-AlCl}_3/\text{THF} > (\text{PMC})_2\text{-AlCl}_3/\text{THF} > (\text{MePMC})_2\text{-AlCl}_3/\text{THF} > (\text{MPMC})_2\text{-AlCl}_3/\text{THF}$. The measured conductivity of the electrolyte solutions, presented in Table 2-3, does not follow this trend; rather, all were $\sim 1 \text{ mS cm}^{-1}$ with the exception of the electron-withdrawing substituted $(\text{FMPMC})_2\text{-AlCl}_3/\text{THF}$, which exhibits conductivity more than twice the others at 2.24 mS cm^{-1} . The higher conductivity is likely due to the stabilization of the overall negative charge on the aluminate anion, creating a weaker ion pair.

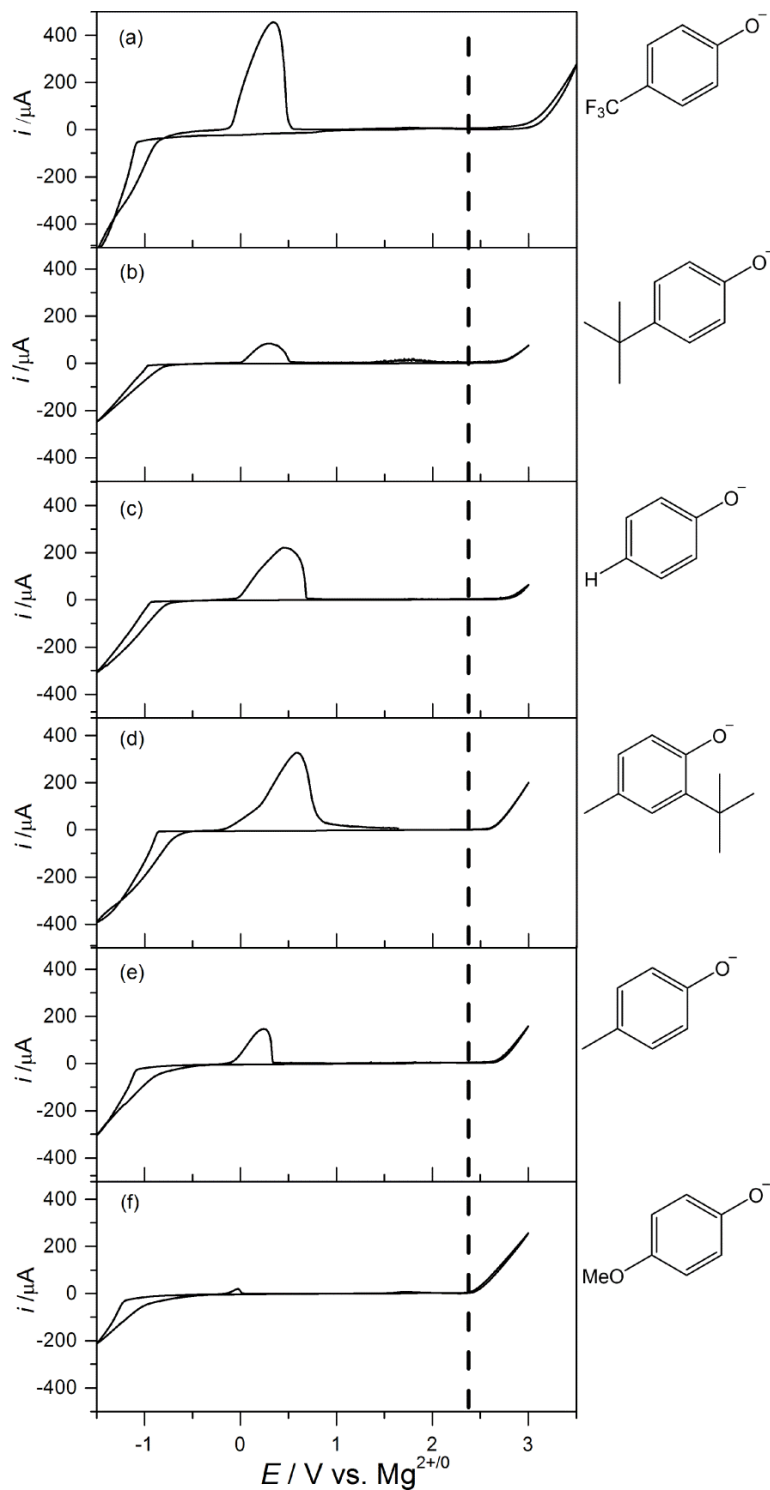


Figure 2.6 Cyclic voltammograms of a) $(\text{FMPMC})_2\text{-AlCl}_3/\text{THF}$, b) $(\text{BPMC})_2\text{-AlCl}_3/\text{THF}$, c) $(\text{PMC})_2\text{-AlCl}_3/\text{THF}$, d) $(\text{BMPMC})_2\text{-AlCl}_3/\text{THF}$ e) $(\text{MePMC})_2\text{-AlCl}_3/\text{THF}$, f) $(\text{MPMC})_2\text{-AlCl}_3/\text{THF}$. The scan rate is 25 mV/s. The best previously reported electrolyte $[(2\text{-tert-butyl-4-methyl-phenolate magnesium chloride})_2\text{AlCl}_3/\text{THF}]^{[53]}$ was prepared and is included below for comparison. The phenolate ligands and dashed lines are shown for clarity.

Table 2-3. Conductivity, voltage, anodic current, and Hammett σ^+ values for the substituted phenolate electrolyte complexes.

| Substituent | σ^+ value | $E_{\text{on}}^{[a]} / \text{V}$ | $I_a^{[b]} / \mu\text{A}$ | $\rho / \mu\text{S cm}^{-1[c]}$ |
|-----------------|------------------|----------------------------------|---------------------------|----------------------------------|
| OMe | -0.78 | 2.31 | 257.08 | 1052 |
| Me | -0.31 | 2.58 | 158.94 | 1119 |
| t-Bu | -0.26 | 2.74 | 74.95 | 736 |
| H | 0 | 2.71 | 64.66 | 877 |
| CF ₃ | 0.61 | 2.90 | 9.474 | 2240 |
| F ₅ | — | 3.05 | 3.90 | 2448 |

[a] Potential vs $\text{Mg}^{2+/0}$ at which the onset of anodic current is first observed. [b] Anodic current at 3 V vs $\text{Mg}^{2+/0}$. [c] Conductivity measured at 25 °C at 0.5 M (based on Mg^{2+})

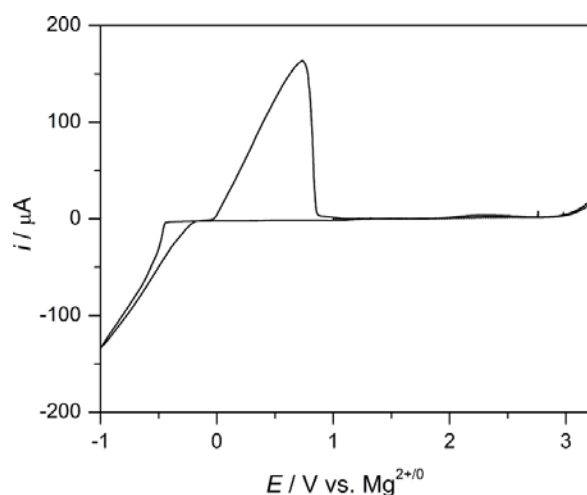


Figure 2.7 Steady-state cyclic voltammogram of $(\text{FMPMC})_2\text{-AlCl}_3/\text{THF}$ performed at a scan rate of 1 mV/s.

The electrochemistry illustrates the strong dependence of phenolate substitution on electrical performance. The Hammett plot in Figure 2.8 of onset potential vs. σ^+ values (σ^+ representing Hammett parameters for phenol) shows a linear negative slope, consistent with positive charge build up during oxidation.⁵⁴ Withdrawing groups destabilize positive charge increasing the difficulty of oxidation, and thus increasing the oxidation potential of the electrolyte.⁵⁵

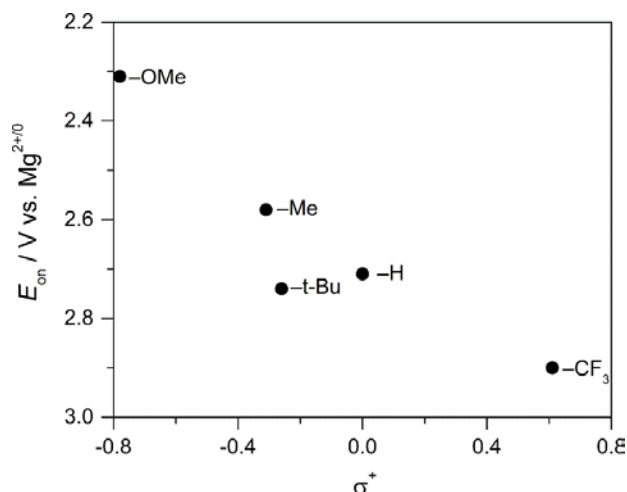


Figure 2.8 Hammett plot of para-substituted phenols vs oxidation onset potential of non-Grignard electrolytes.

This trend has been unfurled for Grignard reagents where the addition of fluorinated groups to RMgBr in THF results in a wider electrochemical window (~ 2.4 V) and a 1.5 times enhancement of the ionic conductivity,⁵⁶ but not explored for the non-Grignard congeners. This same trend is observed with the anodic current recorded at 3 V vs. $\text{Mg}^{2+/0}$ (Figure 2.9). The $(\text{BPMC})_2\text{-AlCl}_3/\text{THF}$ electrolyte does not follow the main trend of σ^+ values, suggesting that the steric bulk or other currently unknown factor of the alkyl substituents enhances oxidative stability, though incorporating additional alkyl substituents is needed to confirm this postulation.

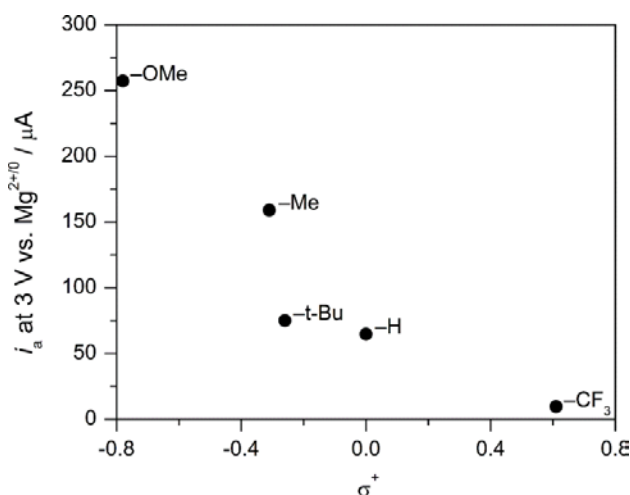


Figure 2.9 Hammett plot of anodic current at 3 V vs. $\text{Mg}^{2+/0}$ vs. σ^+ values of p-substituted phenols.

To test the stability of the electrolyte to air and moisture, a solution of the electrolyte was exposed to air for 6 hours. Figure 2.10 shows that the oxidative stability of the electrolyte $(\text{FMPMC})_2\text{-AlCl}_3/\text{THF}$ remains the same, and reversible Mg deposition-dissolution is still observed. However, the decrease in efficiency and increased polarization is likely due to the slow oxidation of the Mg–Cl bonds, as has been previously reported.⁴⁴

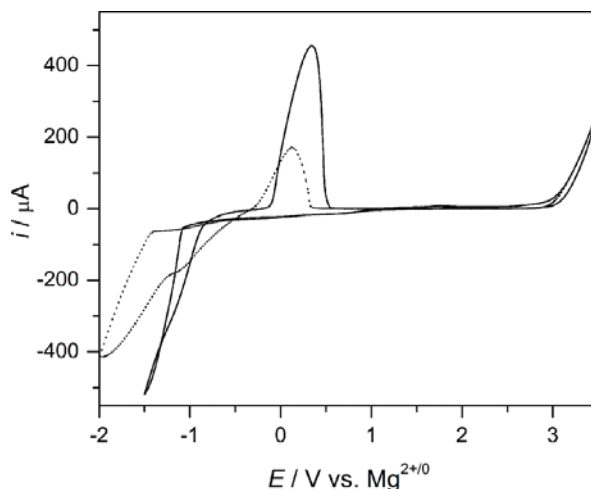


Figure 2.10 Cyclic voltammograms of $(\text{FMPMC})_2\text{-AlCl}_3/\text{THF}$ (—) and after (- - -) exposure to air for 6 hours.

²⁷Al NMR spectra recorded from the APC sample after air exposure shows the complete disappearance of the $\text{Al}(\text{Ph})_4^-$ species at 131 ppm and the appearance of at least three additional reaction products. The sample of $(\text{FMPMC})_2\text{-AlCl}_3/\text{THF}$ on the other hand looks largely unchanged with the exception of two additional peaks at 115 ppm and 125 ppm, matching the two most downfield peaks in the APC sample. This suggests the phenolate electrolyte system reacts more slowly with moisture in ambient air, with minimal by-products forming a passivating layer on the electrode that results in the increased polarization and decreased efficiency. The ability to characterize and analyse the magnesium species as well as the interaction between the electrolyte and electrode surface would enable the verification of how air/moisture change the Mg deposition chemistry.

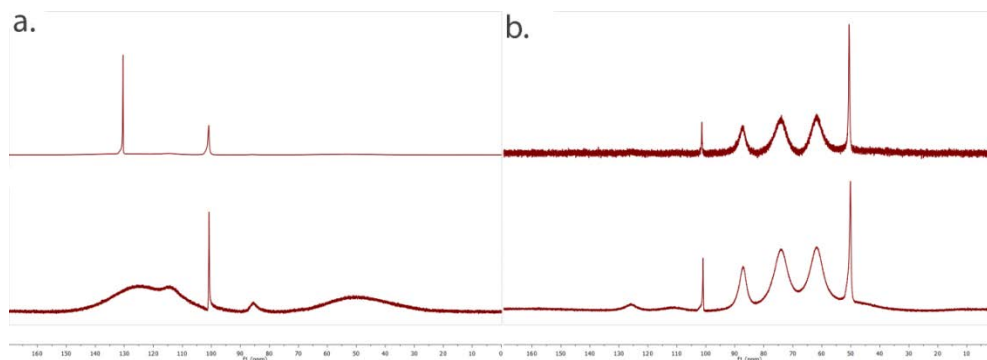


Figure 2.11 ^{27}Al NMR spectra of a.) APC electrolyte as synthesized top, and after 6 hour air exposure bottom b.) $(\text{FMPMC})_2\text{-AlCl}_3/\text{THF}$ electrolyte as synthesized top, and after 6 hour air exposure bottom.

To expand the application of physical organic principles to these types of electrolyte systems, the pentafluorophenolate complex was synthesized. Although the σ^+ Hammett values for all positions on the phenol ring are not known, the increased number of electron-withdrawing groups results in a ~ 100 mV enhancement in the anodic stability, increasing the electro-chemical window to 3 V for non-Grignard magnesium electrolytes (Figure 2.12). This result represents the largest stability window for non-Grignard electrolytes, and is 400 mV more positive than what has been previously reported, moving the non-Grignard systems close to the stability window of the Grignard electrolytes. The conductivity of $(\text{PFPMC})_2\text{-AlCl}_3/\text{THF}$ is 2.44 mS cm^{-1} , similar to that of $(\text{FMPMC})_2\text{-AlCl}_3/\text{THF}$.

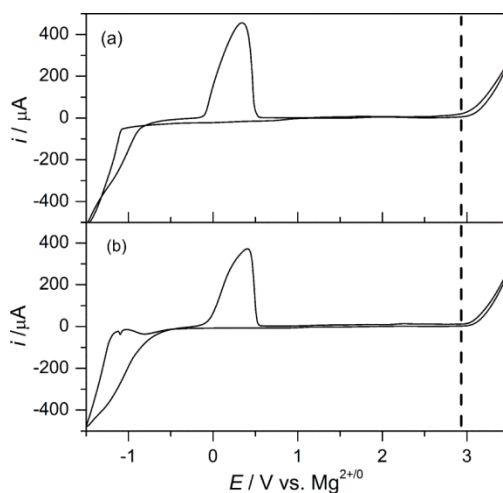


Figure 2.12 Cyclic voltammograms of Pt electrodes in 0.5 M a) $(\text{FMPMC})_2\text{-AlCl}_3/\text{THF}$ and b) $(\text{PFPMC})_2\text{-AlCl}_3/\text{THF}$ solutions. The scan rate is 25 mV/s and the dashed line is added as a guide to the eye.

In order to verify the compatibility of the $(\text{FMPMC})_2\text{-AlCl}_3/\text{THF}$ electrolyte with a Mg-ion intercalation cathode, Mo_6S_8 was synthesized by a known solid-state method⁵⁷ and galvanostatic cycling ($C/5$ rate = $50 \mu\text{A}/\text{cm}^2$) versus a Mg-foil auxiliary electrode shows reversible cycling in Figure 2.13

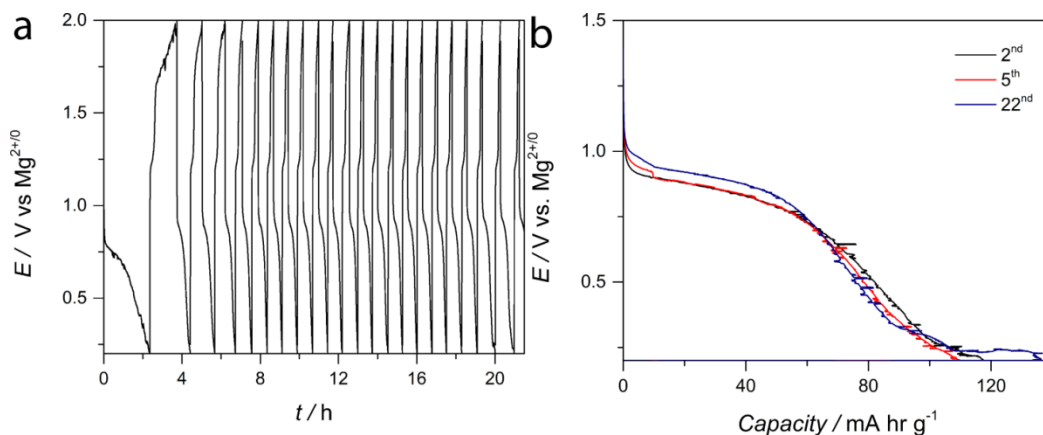


Figure 2.13 a) Reversible galvanostatic cycling of Mo_6S_8 vs Mg-foil in $0.5 \text{ M } (\text{FMPMC})_2\text{-AlCl}_3/\text{THF}$ electrolyte at $C/5$. b) Discharge curves of Mo_6S_8 vs. Mg-foil in $(\text{FMPMC})_4\text{-AlCl}_3/\text{THF}$ electrolyte.

In an effort to distinguish which solution species is responsible for the wider potential window, bulk electrolysis of $(\text{FMPMC})_2\text{-AlCl}_3$ was carried out at $3.5 \text{ V vs. Mg}^{2+/0}$ for 90 minutes. Comparing the ^{27}Al NMR spectra before and after electrolysis shows decomposition of the *in situ* formed aluminium complex (Figure 2.14). The change in relative intensities between $\text{Al}(\text{FMP})_4^-$ and Al_2Cl_6 suggests the Lewis acid, specifically the tetraphenolated aluminium complex is the main contributor to the anodic stability of these non-Grignard electrolytes. The Lewis acid is often postulated to be responsible for the oxidative stability of the Grignard congeners.⁵⁸

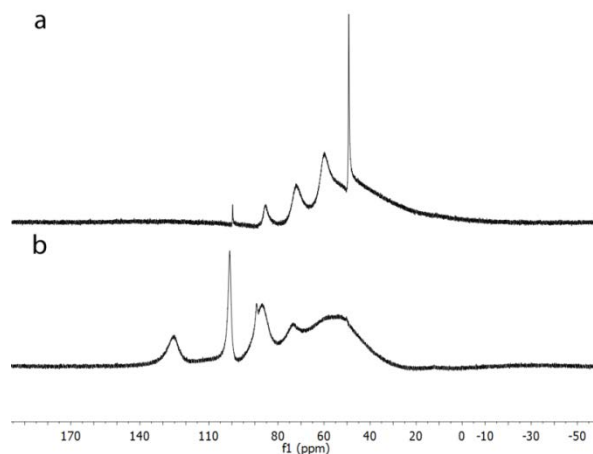


Figure 2.14 ^{27}Al NMR spectra of $(\text{FMPMC})_2\text{-AlCl}_3/\text{THF}$ a) before and b) after electrolysis at 3.5 V vs. $\text{Mg}^{2+/0}$ for 90 minutes.

2.4 Conclusion

In summary, through a controlled exploration of substituted phenols, we have shown that the anodic stability of $\text{ROMgCl}:\text{AlCl}_3\text{-THF}$ non-Grignard electrolytes can be pushed ~ 400 mV past the phenolate electrolytes previously published by placing very electron-withdrawing substituents on the phenolate ring. This potential brings these non-Grignard electrolyte systems close to the stability of previously published Grignard based electrolytes. Using phenolate ligands allows for improved stability in air and lower nucleophilicity, opening the door to exploring high density cathodes such as Mg-air and Mg-sulfur. The use of physical organic design principles and a general synthesis method will allow us to widen the stability window of these types of Mg electrolytes.

2.5 Experimental

2.5.1 General considerations

Ethylmagnesium chloride and all phenols were purchased from Sigma Aldrich, and used as received. Tetrahydrofuran solvent was purchased from VWR, and distilled over sodium with a benzophenone-ketyl indicator. ^{27}Al NMR spectroscopy was performed on a Varian VNMRS-700 MHz spectrometer in THF with chemical shifts reported relative to a solution of AlCl_3 in D_2O with a drop of concentrated HCl. ^1H , ^{13}C , and ^{19}F NMR

spectroscopy was performed on a Varian MR-400 MHz spectrometer in THF. Conductivity measurements were carried out using a YSI Model 3200 conductivity meter equipped with a 3253 conductivity cell at room temperature. Mass spectrometry was performed on a Micromass LCT Time-of-Flight mass spectrometer with electrospray ionization. Raman spectra were collected using a Renishaw Raman microscope with a Leica microscope, RenCam CCD detector, 785 nm laser, 1200 lines/mm grating, and 50 μm slit. The spectra were collected in extended scan mode (10 second scan with 100 accumulations) in the range of 2000 – 200 cm^{-1} .

2.5.2 NMR Data

(FMPMC)₂-AlCl₃/THF – ¹H 7.4 – 6.9(m) ¹³C 163.8, 163.5, 163.2, 126.8, 126.07, 126.04, 126.00, 124.1, 119.76, 119.69, 119.62 ¹⁹F –62.7, –62.9.

(BPMC)₂-AlCl₃/THF – ¹H 7.0 – 6.6(m), 1.21, 1.20 ¹³C 157.5, 156.1, 154.9, 141.1, 138.6, 128.6, 127.9, 125.3, 125.2, 125.1, 124.7, 119.0, 118.9, 118.8, 118.7, 33.43, 33.39, 33.29, 31.1, 31.0, 30.9.

(PMC)₂-AlCl₃/THF – ¹H 7.1–6.5(m) ¹³C 160.3, 160.2, 160.1, 128.8, 128.6, 128.5, 128.3, 128.2, 120.0, 119.9, 119.8, 119.7, 119.6, 117.1, 116.8.

(MePMC)₂-AlCl₃/THF ¹H 6.8–6.6 (m) ¹³C 157.7, 157.4, 155.5, 155.3, 129.39, 129.34, 129.24, 129.19, 129.10, 129.05, 128.84, 128.79, 125.27, 119.62, 119.55, 119.50, 119.31, 119.25, 114.95, 114.92, 19.92, 19.89, 19.87.

(MPMC)₂-AlCl₃/THF ¹H 6.91–6.57 (m) ¹³C 154.87, 154.39, 154.30, 154.14, 152.99, 152.79, 121.35, 121.31, 120.86, 120.75, 116.80, 115.44, 115.16, 115.13, 114.97, 114.92, 56.19, 56.19, 56.16, 56.12, 56.07.

(PFPMC)₂-AlCl₃/THF ¹³C 141.84, 139.45, 139.05, 136.63, 135.08, 134.24, 131.84 ¹⁹F – 162.45, –163.4, –164.4, –165.4, –171.3, –178.6.

2.5.3 X-ray Structure Determination for C₆₂H₈₂Cl₂Mg₅O₁₈ (CCDC # 962673)

Colorless needles of en5055 were grown from a tetrahydrofuran/hexane solution at 23 °C. A crystal of dimensions 0.44 x 0.30 x 0.23 mm was mounted on a Bruker SMART APEX-I CCD-based X-ray diffractometer equipped with a low temperature device and fine focus Mo-target X-ray tube ($\lambda = 0.71073 \text{ \AA}$) operated at 1500 W power

(50 kV, 30 mA). The X-ray intensities were measured at 85(1) K; the detector was placed at a distance 5.081 cm from the crystal. A total of 4905 frames were collected with a scan width of 0.5° in ω and 0.45° in ϕ with an exposure time of 20 s/frame. The integration of the data yielded a total of 351974 reflections to a maximum 2θ value of 70.00° of which 29000 were independent and 23284 were greater than $2\sigma(I)$. The final cell constants (Table S3) were based on the xyz centroids of 9459 reflections above $10\sigma(I)$. Analysis of the data showed negligible decay during data collection; the data were processed with SADABS and corrected for absorption. The structure was solved and refined with the Bruker SHELXTL (version 2008/4) software package, using the space group $P2(1)/c$ with $Z = 4$ for the formula $C_{62}H_{82}Cl_2Mg_5O_{18}$. All non-hydrogen atoms were refined anisotropically with the hydrogen atoms placed in idealized positions. Full matrix least-squares refinement based on F^2 converged at $R1 = 0.0423$ and $wR2 = 0.1067$ [based on $I > 2\sigma(I)$], $R1 = 0.0575$ and $wR2 = 0.1178$ for all data. Two THF ligands and one phenolate ligand are disordered and were refined with partial occupancy orientations constrained to sum to one. Additional details are presented in Table S3 and are given as Supporting Information in a CIF file.^{59–61}

Table 2-4 Crystal data and structure refinement for en5055 (CCDC # 962673)

| | |
|------------------------------------|---|
| Identification code | en5055 |
| Empirical formula | $C_{62}H_{82}Cl_2Mg_5O_{18}$ |
| Formula weight | 1307.73 |
| Temperature | 85(2) K |
| Wavelength | 0.71073 Å |
| Crystal system, space group | Monoclinic, $P2_1/c$ |
| Unit cell dimensions | $a = 14.4018(5)$ Å $b = 24.2154(8)$ Å $\beta = 104.534(1)^\circ$ $c = 19.5295(7)$ Å |
| Volume | $6592.6(4)$ Å ³ |
| Z , ρ_{calc} | 4, 1.318 g/cm ³ |
| Absorption coefficient | 0.214 mm ⁻¹ |
| $F(000)$ | 2768 |
| Crystal size | $0.44 \times 0.30 \times 0.23$ mm |
| θ range for data collection | $1.37 - 35.00^\circ$ |
| Limiting indices | $-23 \leq h \leq 23$ $-38 \leq k \leq 38$ $-31 \leq l \leq 31$ |
| Reflections collected/unique | 351974 / 29000 [$R(\text{int}) = 0.0626$] |

| | |
|--|------------------------------------|
| Completeness to $\theta = 35.00^\circ$ | 99.9% |
| Absorption correction | Semi-empirical from equivalents |
| Max. and min. Transmission | 0.9524 and 0.9116 |
| Refinement method | Full-matrix least-squares on F^2 |
| Data / restraints / parameters | 29000 / 165 / 878 |
| $G.o.F.$ on F^2 | 1.006 |
| Final R indices [$I > 2\sigma(I)$] | $R1 = 0.0423$; $wR2 = 0.1067$ |
| R indices (all data) | $R1 = 0.0575$, $wR2 = 0.1178$ |
| Largest diff. peak and hole | 1.238 and -0.275 eA^{-3} |

2.5.4 X-ray Structure Determination for $\text{C}_{31}\text{H}_{52}\text{F}_3\text{O}_7\text{Mg}_2\text{AlCl}_6$ (CCDC # 962674)

Colorless blocks of en51302a were grown from a hexane/tetrahydrofuran solution of the compound at 23°C . A crystal of dimensions $0.18 \times 0.10 \times 0.10 \text{ mm}$ was mounted on a Rigaku AFC10K Saturn 944+ CCD-based X-ray diffractometer equipped with a low temperature device and Micromax-007HF Cu-target micro-focus rotating anode ($\lambda = 1.54187 \text{ \AA}$) operated at 1.2 kW power (40 kV, 30 mA). The X-ray intensities were measured at 85(1) K with the detector placed at a distance 42.00 mm from the crystal. A total of 4336 images were collected with an oscillation width of 1.0° in ω . The exposure time was 1 sec. for the low angle images, 5 sec. for high angle. The integration of the data yielded a total of 243483 reflections to a maximum 2θ value of 136.46° of which 7714 were independent and 7043 were greater than $2\sigma(I)$. The final cell constants Table S4) were based on the xyz centroids 143984 reflections above $10\sigma(I)$. Analysis of the data showed negligible decay during data collection; the data were processed with CrystalClear 2.0 and corrected for absorption. The structure was solved and refined with the Bruker SHELXTL (version 2008/4) software package, using the space group $Pbca$ with $Z = 8$ for the formula $\text{C}_{31}\text{H}_{52}\text{F}_3\text{O}_7\text{Mg}_2\text{AlCl}_6$. All non-hydrogen atoms were refined anisotropically with the hydrogen atoms placed in idealized positions. The THF ligands are extensively disordered. Full matrix least-squares refinement based on F^2 converged at $R1 = 0.0807$ and $wR2 = 0.2135$ [based on $I > 2\sigma(I)$], $R1 = 0.0843$ and $wR2 = 0.2162$ for all data. Additional details are presented in Table S4 and are given as Supporting Information in a CIF file. Acknowledgement is made for funding from NSF grant CHE-0840456 for X-ray instrumentation.^{59,62}

Table 2-5 Crystal data and structure refinement for en51302a (CCDC # 962674)

| | |
|---|--|
| Identification code | en51302a |
| Empirical formula | C ₃₁ H ₅₂ AlCl ₆ Mg ₂ O ₇ |
| Formula weight | 882.03 |
| Temperature | 85(2) K |
| Wavelength | 1.54178 Å |
| Crystal system, space group | Orthorhombic, <i>Pbca</i> |
| Unit cell dimensions | <i>a</i> = 19.9228(4) Å <i>b</i> = 15.0009(3) Å <i>c</i> = 28.215(2) Å |
| Volume | 8432.4(6) Å ³ |
| <i>Z</i> , ρ_{calc} | 8, 1.390 g/cm ³ |
| Absorption coefficient | 4.679 mm ⁻¹ |
| <i>F</i> (000) | 3680 |
| Crystal size | 0.18 × 0.10 × 0.10 mm |
| θ range for data collection | 3.13 – 68.23° |
| Limiting indices | -23 ≤ <i>h</i> ≤ 24 -18 ≤ <i>k</i> ≤ 18 -33 ≤ <i>l</i> ≤ 33 |
| Reflections collected/unique | 243483 / 7714 [<i>R</i> (int) = 0.1127] |
| Completeness to $\theta = 68.23^\circ$ | 100.0% |
| Absorption correction | Semi-empirical from equivalents |
| Max. and min. transmission | 0.6519 and 0.4863 |
| Refinement method | Full-matrix least-squares on <i>F</i> ² |
| Data / restraints / parameters | 7714 / 776 / 728 |
| <i>G.o.F.</i> on <i>F</i> ² | 1.072 |
| Final <i>R</i> indices [<i>I</i> > 2σ(<i>I</i>)] | <i>R</i> 1 = 0.0807; <i>wR</i> 2 = 0.2135 |
| <i>R</i> indices (all data) | <i>R</i> 1 = 0.0843, <i>wR</i> 2 = 0.2162 |
| Extinction coefficient | 0.00066(4) |
| Largest diff. peak and hole | 0.711 and -0.726 eÅ ⁻³ |

2.5.5 Electrochemistry

Cyclic voltammograms were recorded using a CH Instruments Electrochemical Workstation 1000A with a Pt-disk working electrode and Mg-foil counter- and reference electrodes. Measurements were carried out at a scan rate of 25 mV/s, starting at OCP (ranging from 1.5 – 1.7 vs Mg^{2+/0}) and scanned cathodically. All electrolyte solutions were 0.5 M (based on Mg) in THF, and measurements were performed using a custom-designed sealed cell in an N₂ box to avoid concentration change during the measurements. Referencing to the Fc⁺⁰ couple was carried out in a 0.5M (FMPMC)₂-AlCl₃/THF solution containing 10 mM ferrocene in THF with a Pt working electrode, a Mg foil auxiliary electrode, and a Mg foil reference electrode. Electrolyte stability was interrogated by opening a vial of the electrolyte to air, and allowing it to stir for 1 hour, followed by stirring for an additional 5 hours lightly capped to minimize solvent evaporation. The slurry of Mo₆S₈ was made by mixing an 8:1:1 weight-ratio mixture of Mo₆S₈, super-P carbon powder, and polyvinylidene fluoride (PVDF) binder in

N-methyl-2-pyrrolidinone (NMP). The cathode slurry was placed on an Al current collector and dried in an oven at 120 °C. The active material loading was approximately 2 mg/cm². The cathode was placed in an electrochemical cell with a Mg foil anode and 0.5M (FMPCM)₂-AlCl₃/THF electrolyte. The charge-discharge tests of the cell were carried on a Vencon UBA4 battery analyzer charger and conditioner (Toronto, Canada) with cut-off voltages of 2.0 and 0.2 V vs. Mg^{2+/0}.

2.5.6 Synthesis

All compounds were prepared and handled using standard Schlenk techniques under N₂ and an N₂-filled glove box (Vacuum Atmospheres). All electrolyte solutions were synthesized in the exact same manner, with details for (FMPCM)₂-AlCl₃ in THF presented here. 4-(trifluoromethyl)phenol (14 mmol, 2.27 g) was dissolved in dry THF (7 mL) with stirring in a 25 mL three neck round bottom flask equipped with a stir bar, rubber septa, glass stopper and a gas inlet adapter. Then, 2 M EtMgCl in THF (14 mmol, 7 mL) was slowly added via syringe. This solution was stirred for 8 hours, giving a suspension of 4-(trifluoromethyl)phenolatemagnesium chloride (FMPCM)/THF. A solution of AlCl₃ (0.5 M in 14 mL) was prepared by mixing AlCl₃ (0.934 g, 7 mmol) with THF (14 mL) in a 25 mL three neck round bottom flask under N₂ purge that is cooled to 0 °C in an ice bath. This solution was warmed to room temperature and then added via syringe to the phenolate solution, and stirred for 5 hours, giving a clear solution of 0.5 M (FMPCM)₂-AlCl₃/THF.

2.6 References

- 40 Liebenow, C., Yang, Z., Lobitz, P. The Electrodeposition of Magnesium using Solutions of Organomagnesium Halides, Amidomagnesium Halides and Magnesium Organoborates, *Electrochemistry Communications*, **2000**, 2, 641-645
- 41 Kim, H. S., Arthur, T. S., Allred, G. D., Zajicek, J., Newman, J. G., Rodnyansky, A. E., Oliver, A. G., Boggess, W. C., Muldoon, J., Structure and Compatibility of a Magnesium Electrolyte with a Sulphur Cathode, *Nature Commun.* **2011**, 2, 427
- 42 Martin, R.P., Doub, W. H., Roberts, J. L., Sawyer, D. T. Electrochemical Reduction of Sulfur in Aprotic Solvents, *Inorg. Chem.*, **1973**, 12, 1921-1925
- 43 Mikhaylik, Y. V., Akridge, J. R. Polysulfide Shuttle Study in the Li/S Battery System, *J. Electrochem. Soc.*, **2004**, 151, A1969-A1976

- 44 Wang, F., Guo, Y., Yang, J., Nuli, Y., Hirano, S. A Novel Electrolyte System without a Grignard Reagent for a Magnesium Batteries, *Chem. Commun.* **2012**, 48, 10763-10765
- 45 Hermanek, S., Kriz, O., Fusek, J., Cerny, Z., Casensky, B. Alkoxohydridoaluminates. Part 2. The Influence of Alkyl Substituents, Solvent, and Temperature on the Molar Fractions of Components, Equilibrium Constants, and ^{27}Al N.M.R. Data for Equilibrium Mixtures Containing $\text{Bu}_4\text{N}^+\text{AlH}_{4-n}(\text{OR})_n^-$ *J. Chem. Soc. Perkin Trans. II* **1989**, 8, 987-992
- 46 Malmvik, A., Obenius, U., Henriksson, U. Equilibration of Lithium Alkoxyaluminates Derived from n-Butyl, s-Butyl, and t-Butyl Alcohols Studied by ^{27}Al Nuclear Magnetic Resonance, *J. Chem. Soc. Perkin Trans. II* **1986**, 12, 1905-1910
- 47 a.) Ohman, L., Edlund, U. **2007**, Aluminum-27 NMR of Solutions, *eMagRes*; b.) Benn, R., Rukinska, A. High-Resolution Metal NMR Spectroscopy of Organometallic Compounds, *Angew. Chem. Int. Ed. Engl.* **1986**, 25, 861-881
- 48 Mizrahim, O., Amir, N., Pollak, E., Chusid, O., Marks, V., Gottlieb, H., Larush, L., Zinigrad, E., Aurbach, D., Electrolyte Solutions with a Wide Electrochemical Window for Rechargeable Magnesium Batteries, *J. Electrochem. Soc.* **2008**, 155, A103-A109
- 49 Gizbar, H., Vestfrid, Y., Chusid, O., Gofer, Y., Gottlieb, H. E., Marks, V., Aurbach, D. Alkyl Group Transmetalation Reactions in Electrolytic Solutions Studied by Multinuclear NMR, *Organometallics* **2004**, 23, 3826-3831
- 50 Vestfried, Y., Chusid, O., Goffer, Y., Aped, P., Aurbach, D., Structural Analysis of Electrolyte Solutions Comprising Magnesium-Aluminate Chloro-Organic Complexes by Raman Spectroscopy, *Organometallics*, **2007**, 26, 3130-3137
- 51 Decken, A., Jenkins, H., Nikiforov, G., Passmore, J. The Reaction of $\text{Li}[\text{Al}(\text{OR})_4]$ $\text{R}=\text{OC}(\text{CF}_3)_2\text{Ph}$, $\text{OC}(\text{CF}_3)_3$ with NO/NO_2 giving $\text{NO}[\text{Al}(\text{OR})_4]$, $\text{Li}[\text{NO}_2]$ and N_2O . The Synthesis of $\text{NO}[\text{Al}(\text{OR})_4]$ from $\text{Li}[\text{Al}(\text{OR})_4]$ and $\text{NO}[\text{SbF}_6]$ in Sulfur Dioxide Solution, *Dalton Trans.*, **2004**, 2496-2504
- 52 Tomar, N., Ghanti, E., Bhagi, A., Nagarajan, R. Studies on the Hydrolysis of $\{\text{Cu}[\text{Al}(\text{OPr})_4]_2\}$, A Single Source Precursor for CuAl_2O_4 Spinel, *J. Non-Cryst. Solids*, **2009**, 355, 2657-2662
- 53 Wang, F., Guo, Y., Yang, J., Nuli, Y., Hirano, S. A Novel Electrolyte System without a Grignard Reagent for a Magnesium Batteries, *Chem. Commun.* **2012**, 48, 10763-10765
- 54 Anslyn, E. V., Dougherty, D. A., Modern Physical Organic Chemistry, University Science Books, California, **2006**, 445-453
- 55 Hansch, C., Leo, A., Taft, R. W. A Survey of Hammett Substituent Constants and Resonance and Field Parameters, *Chem Rev.*, **1991**, 91, 165-195
- 56 Guo, Y., Yang, J., Nuli, Y., Wang, J. Study of Electronic Effect of Grignard Reagents on their Electrochemical Behavior, *Electrochem. Commun.* **2010**, 12, 1671-1673
- 57 Lancry, E., Levi, E., Gofer, Y., Levi, M., Salitra, G., Aurbach, D. Leaching Chemistry and the Performance of the Mo_6S_8 Cathodes in Rechargeable Mg Batteries, *Chem. Mater.*, **2004**, 16, 2832-2838
- 58 a.) Guo, Y., Zhang, F., Yang, J., Wang, F., Nuli, Y., Hirano, S. Boron-based Electrolyte Solutions with Wide Electrochemical Windows for Rechargeable Magnesium Batteries, *Energy Environ. Sci.* **2012**, 5, 9100-9106; b.) Guo, Y., Zhang, F., Yang, J., Wang, F. Electrochemical Performance of Novel Electrolyte Solutions Based on Organoboron-Magnesium Salts, *Electrochem. Commun.* **2012**, 18, 24-27

- 59 G. M. Sheldrick, SHELXTL, v. 2008/4; Bruker Analytical X-ray, Madison, WI, 2008.
- 60 Saint Plus, v. 7.60A, Bruker Analytical X-ray, Madison, WI, 2009.
- 61 G. M. Sheldrick, SADABS, v. 2008/1. Program for Empirical Absorption Correction of Area Detector Data, University of Gottingen: Gottingen, Germany, 2008.
- 62 CrystalClear Expert 2.0 r12, Rigaku Americas and Rigaku Corporation (2011), Rigaku Americas, 9009, TX, USA 77381-5209, Rigaku Tokyo, 196-8666, Japan.

CHAPTER 3

Magnesium-ion Electrolyte Exhibiting Wide Potential Window and Reduced Stainless Steel Corrosion

Portions of this chapter have been published:

Nelson, E. G.; Brody S. I.; Kampf, J. W.; Bartlett, B. M. *J. Mater. Chem. A*, 2014, **2**, 18194-18198. Reproduced by permission of the Royal Society of Chemistry
<http://pubs.rsc.org/en/content/articleLanding/2014/TA/c4ta04625k>

3.1 Introduction

One of the goals of Mg-ion battery research is increasing the potential window of the electrolyte. As mentioned earlier, the first break through in Mg-ion electrolytes in the year 2000 gave a potential window of 3.2 V. Although this electrolyte was a dramatic improvement over previous electrolytes with a stability window of ~1.5 V, this window is still too small to compete with the Li-ion electrolytes which have windows approaching 5.5 V vs $\text{Li}^{+/0}$.

The lack of electrolytes exhibiting large potential window stability impedes the cultivation of novel high voltage cathode materials, which is necessary for additional progress in the field.⁶³ Many electrolytes with expanded electrochemical working windows on platinum working electrodes do not show the same stability on common non-noble metal current collectors.^{64,65} The lower potential windows shown on non-noble metals is attributed to the corrosion of the metal due to the high chloride content present in most electrolyte solution⁶⁶. One way around this dilemma is the production of new current collectors compatible with magnesium-ion electrolytes.^{67,68} However, this strategy will require a re-engineering of present battery systems, based mostly on stainless steel, to incorporate new metals. We have instead focused on altering the electrolyte solution to decrease the chloride content.

Previous work has incorporated phenolate ligands in the place of the common alkyl Lewis base as a route to decrease the air and moisture sensitivity of the Grignard Lewis bases commonly used for these electrolyte solutions.^{69,70} Even though these electrolytes perform well, they still contain high levels of chloride anion, and as such, they exhibit a reduced potential window when using non-noble metal working electrodes. Structural characterization of the electrolyte solutions showed ligand exchange creating an $[\text{Al}(\text{OR})_4]^-$ anion and a $[\text{Mg}_2\text{Cl}_3]^+$ cation pair in solution. Because of this ligand exchange, and as the use of AlCl_3 as the Lewis acid is one of the main sources of chloride in solution, we choose to incorporate alkoxide ligands onto the aluminum Lewis acid.

3.2 Results and Discussion

The alkoxide Lewis acid was synthesized through the reaction of phenol with trimethylaluminum. This was then reacted with the Grignard PhMgCl in THF to form the electrolyte. The conductivity of the electrolyte at 0.5 M, based on magnesium concentration, is 1.24 mS/cm, which is within the commonly reported range of Mg-ion electrolytes. Initial electrochemical experimentation, Figure 3.1, shows that $\text{Al}(\text{OPh})_3/\text{PhMgCl}$ exhibits surprising stability out to 5 V. This stability is approximately 1 V past the best previously reported electrolyte.⁷¹

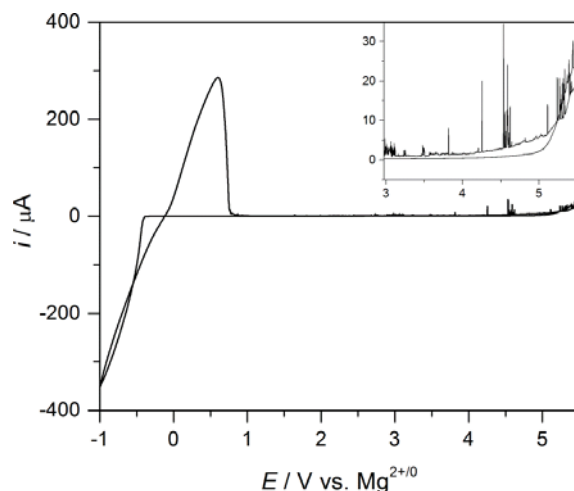


Figure 3.1 CV scan of a solution of 0.5 M $\text{Al}(\text{OPh})_3/\text{PhMgCl}$ in THF on a Pt working electrode at a scan rate of 25 mV/s. Inset shows close up of oxidation potential.

The inset clearly shows random, positive current spikes on the anodic side. Similar

behavior previously reported, as well as the limited anodic stability limit of THF solvent (3.2 V vs $\text{Mg}^{2+/0}$), suggests the formation of a quasi-passivation layer on Pt.⁷² This behavior appears to be unique to the presence of tetraphenylaluminate and it is hypothesized the phenyl groups create a specific adsorption of $\text{Al}(\text{Ph})_4^-$ molecules on the Pt surface, resulting in a break-and-repair-like mechanism.

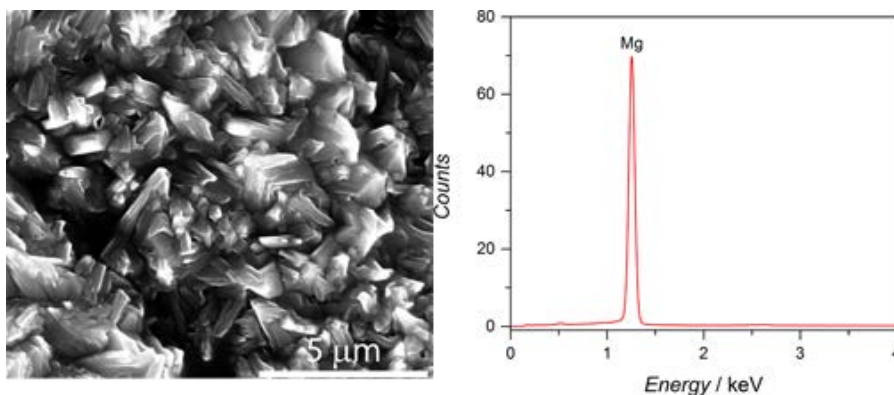


Figure 3.2 SEM and EDX of deposited Mg on Cu foil

Magnesium deposition was confirmed by analyzing a film following galvanostatic deposition (2 mA/cm^2 , 2.3 C passed) onto copper foil. The SEM and EDX analysis showed only Mg^0 deposition in a dense, dendrite free morphology (Figure 3.2). The deposition and stripping events show low overpotentials of 0.47 and 0 V vs $\text{Mg}^{2+/0}$ respectively and good coulombic efficiency ($\sim 98\%$, Figure 3.3).

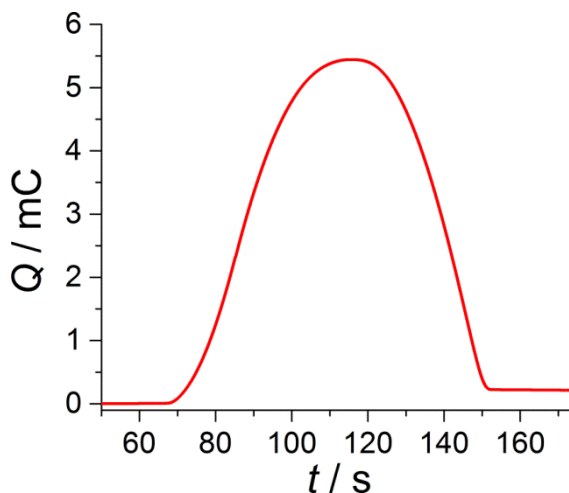


Figure 3.3 Charge balance of Mg deposition/stripping showing an $\sim 98\%$ coulombic efficiency.

The compatibility of Al(OPh)₃/PhMgCl with a WSe₂ cathode, a known intercalation materials for Mg²⁺, was tested.⁷³ The WSe₂ was synthesized via a known solid-state route.⁷⁴ A 2016-type coin cell comprised of 0.5 M Al(OPh)₃/PhMgCl in THF, WSe₂ cathode, and Mg foil anode was charged and discharged at room temperature at a rate of C/5 (12 μA/cm²). Figure 3.4 shows the capacity-voltage profile at the 5th, 10th, 20th, and 50th cycles. The discharge capacity is approximately 80 mAh/g, calculated based on the weight of the cathode mass.

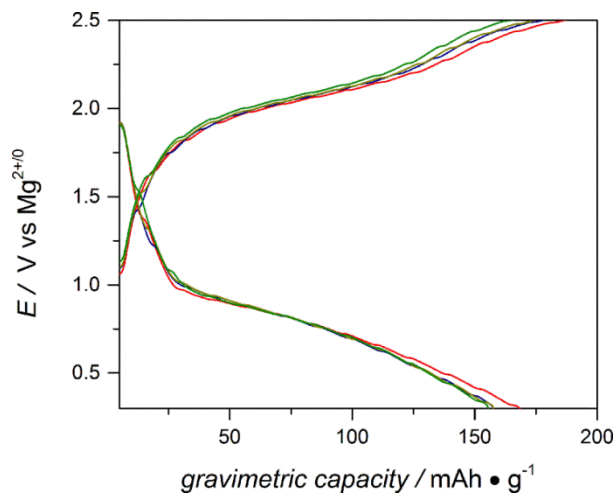


Figure 3.4 Typical charge/discharge profiles for a rechargeable battery with Al(OPh)₃/PhMgCl in THF, a Mg anode, a WSe₂ cathode at cycles 5 (black), 10 (red), 20 (blue), and 50 (green).

This voltage profile is consistent with reversible magnesium insertion into the WSe₂ cathode material. The polarization observed between charge and discharge curves is likely due to the large particle size of the WSe₂ formed from the solid state synthesis. The morphology of WSe₂ is typically large plates ranging in size from 2 – 10 μm, shown in Figure 3.5.

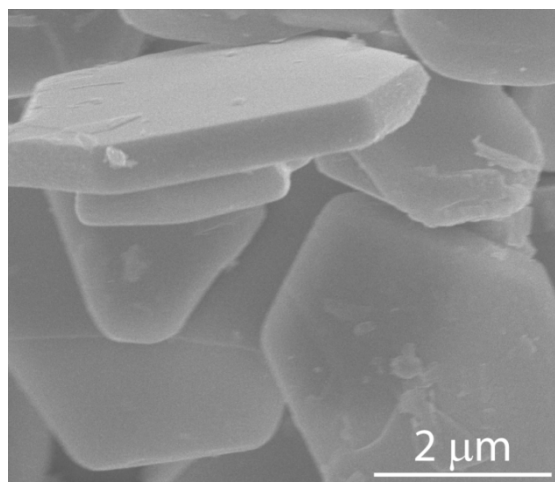


Figure 3.5 SEM image of solid state synthesized WSe_2

Using a 2.5 V cathode does not begin to approach the apparent upper limit of the electrolyte stability, though recent work has focused on higher voltage cathodes.^{75,76} Although the Mo_6S_8 Chevrel-phase cathode exhibits a lower cut off voltage of 1.2 V vs $\text{Mg}^{2+/0}$, $\text{Al}(\text{OPh})_3/\text{PhMgCl}$ was also cycled with Mo_6S_8 as the cathode material (Figure 3.6).

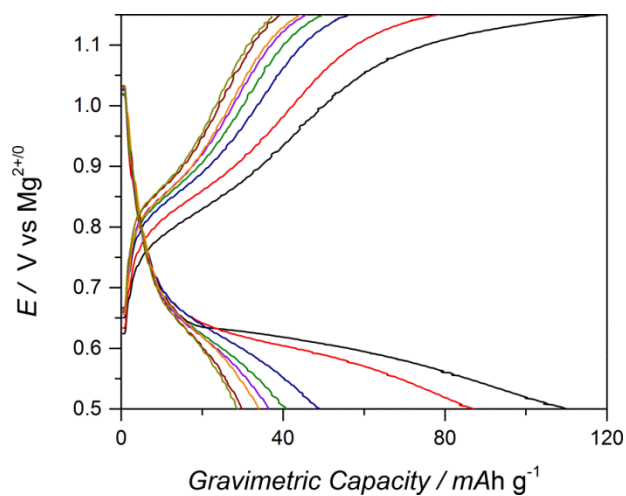


Figure 3.6 Typical charge/discharge profiles for a rechargeable battery with $\text{Al}(\text{OPh})_3/\text{PhMgCl}$ in THF, an Mg anode, a Mo_6S_8 cathode at a rate of $C/20$ ($10 \mu\text{A}/\text{cm}^2$) cycles 1 (black), 2 (red), 10 (navy), 20 (olive), 40 (violet), 60 (orange), 80 (wine), and 100 (dark yellow).

Since the $\text{Al(OPh)}_3\text{-PhMgCl}$ electrolyte contains a much lower chloride concentration, we examined the electrochemistry using stainless steel as the working electrode. A CV scan of $\text{Al(OPh)}_3\text{-PhMgCl}$ on stainless steel shows an electrochemical stability window out to ~ 5 V vs $\text{Mg}^{2+/0}$, much wider than previously reported electrochemical performances on stainless steel (Figure 3.7).

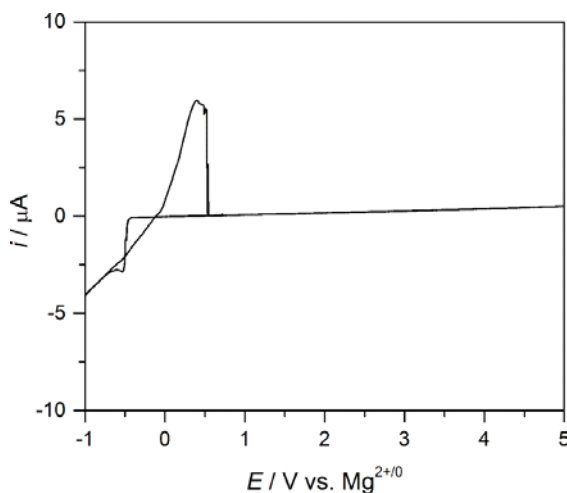


Figure 3.7 Cyclic voltammogram of an electrolyte solution of 0.5 M $\text{Al(OPh)}_3\text{/PhMgCl}$ in THF recorded on a 316 stainless steel micro-working electrode at a scan rate of 25 mV/s.

It is interesting to note the absence of the positive spikes in current in the CV experiment with stainless steel. We hypothesize that the Al(Ph)_4^- and/or benzene/phenyl species do not exhibit adsorption onto stainless steel like they do on Pt, and thus a break-and-repair-like mechanism is not observed. To investigate the increased performance on stainless steel, images of the stainless-steel foil both before and after electrolysis were taken, shown in Figure 3.8. The image of stainless steel before exposure to an electrolyte (Figure 3.8a) appears very similar to stainless steel after a single CV trace in the potential range of 0 to 5 V vs $\text{Mg}^{2+/0}$ with 25 mV s^{-1} with a three-electrode setup in the $\text{Al(OPh)}_3\text{/PhMgCl}$ solution (Figure 3.8b). To further test the stability, prolonged electrolysis experiments at 4.5 V vs. $\text{Mg}^{2+/0}$ were performed on fresh films. After electrolysis for 96 hours the stainless steel foil in $\text{Al(OPh)}_3\text{/PhMgCl}$ solution began to show some signs of pitting (Figure 3.8c) but still considerably less than the foil in the APC electrolyte. The stainless steel present in the APC solution shows a high density of

pitting after a single CV scan (Figure 3.8d). Extended electrolysis in the APC was stopped after only 24 hours as the foil was visibly disintegrating (Figure 3.8e,f).

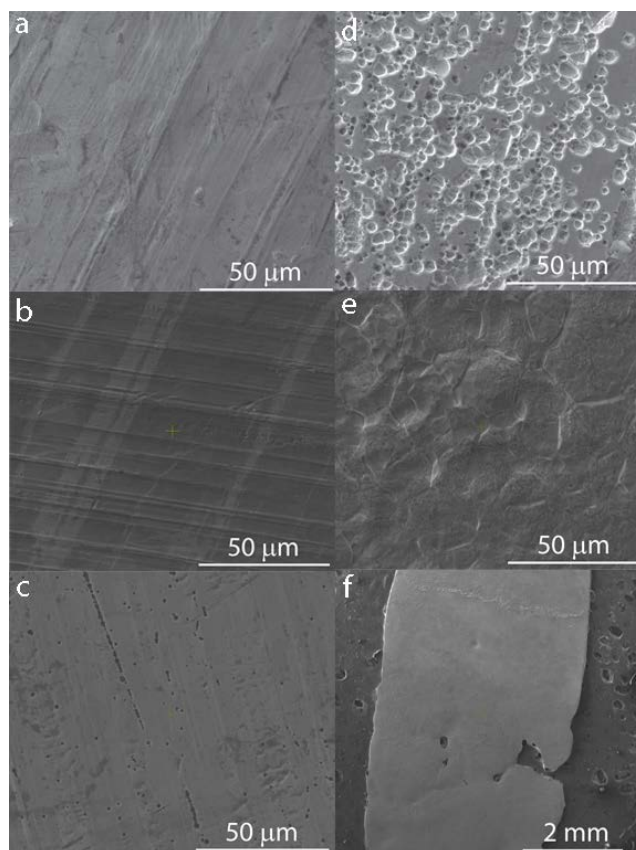


Figure 3.8 SEM images of stainless steel a) before exposure to Mg electrolyte; b) after one CV cycle from 0 – 5.0 V in $\text{Al(OPh)}_3/\text{PhMgCl}$; c) after electrolysis at 4.5 V for 96 hours in $\text{Al(OPh)}_3/\text{PhMgCl}$; d) after one CV cycle from 0 – 4.0 V in APC; e) after electrolysis at 4.0 V for 24 hours in APC; f) after electrolysis at 4.0 V for 24 hours in APC.

Energy-dispersive X-ray (EDX) spectroscopy of the pitted stainless steel after the CV trace is recorded in APC (Figure 3.9) shows that pits are devoid of iron, chromium and manganese, with the retention of nickel and molybdenum. This result correlates with recently published reports exploring the use of alternatives to stainless steel as current collectors.^{67,68} These reports show, as expected, more noble metals exhibit higher resistance to corrosion, along with tungsten, molybdenum, and carbon.

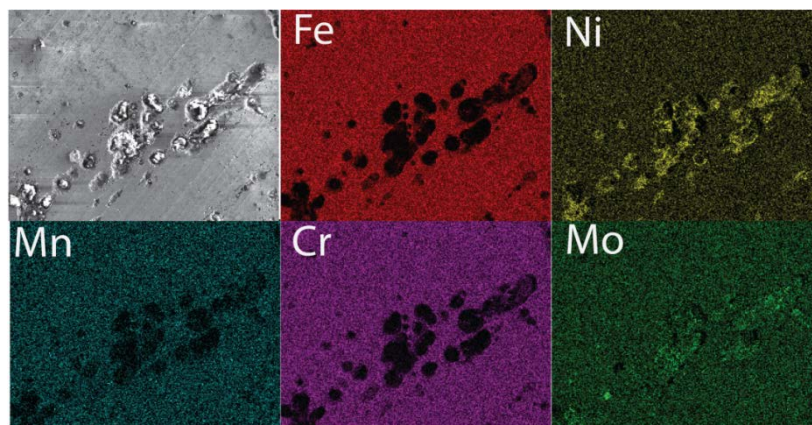


Figure 3.9 EDX map of stainless steel after CV cycling in APC

To probe the stability of stainless steel with this electrolyte in true battery cycling conditions, the coin cell was imaged after cycling with the LiMn_2O_4 cathode. The SEM images presented in Figure 3.10 show no change in the surface morphology of the stainless steel after 100 charge-discharge cycles to 3.5 V vs $\text{Mg}^{2+/0}$.

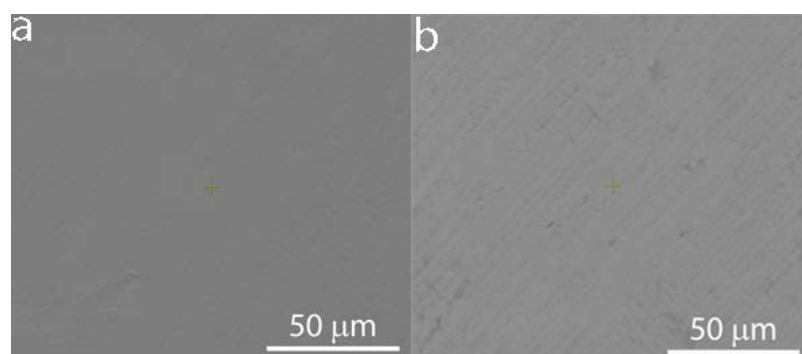


Figure 3.10 SEM images of stainless steel a) before and b) after cycling LiMn_2O_4 with 0.5 M $\text{Al}(\text{OPh})_3/\text{PhMgCl}$ in THF containing 0.5 M LiPF_6 for 100 cycles.

A similar experiment using APC and LiMn_2O_4 was attempted. However, due to the smaller stability window afforded by APC, a large overcharging current was observed and a complete charge-discharge cycle was not possible.

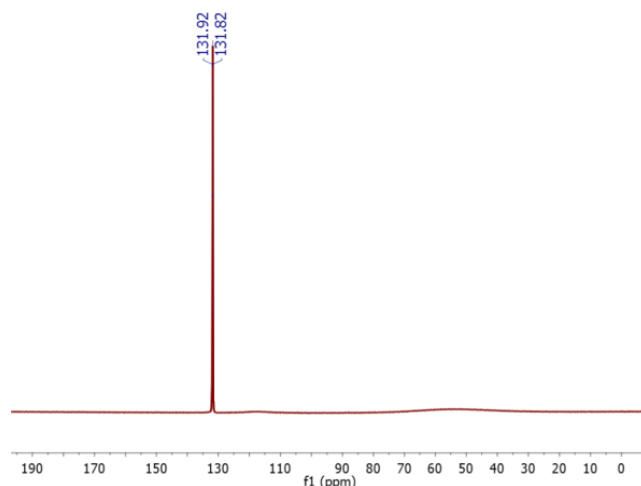


Figure 3.11 ^{27}Al NMR spectra of $\text{Al(OPh)}_3/\text{PhMgCl}$ in THF giving one peak corresponding to Al(Ph)_4^- (131 ppm)

Previous DFT reports suggested AlPh_4^- species to be more susceptible to oxidation when compared to AlCl_4 , though experimentally this was shown to not be the case.⁷⁷ Initial structural characterization via ^{27}Al NMR spectroscopy shows AlPh_4^- to be the main anion in solution (Figure 3.11), resulting from ligand exchange between the aluminum and magnesium starting materials. The ^{13}C NMR spectra and ESI-MS analysis show a more complex picture with carbon peaks assigned to Ph-Mg, Ph-Al, and PhO-Al, similar to what has previously been reported for mixed magnesium/aluminum electrolytes (Figure 3.12 and Table 3-1).⁷⁸ The ESI-MS analysis in negative-ion mode show similar products including Al(Ph)_4^- and $\text{Al(Ph)}_3(\text{OPh})^-$, as well as a few other aluminum complexes which make up smaller contributions to the solution speciation (Figure 3.13).

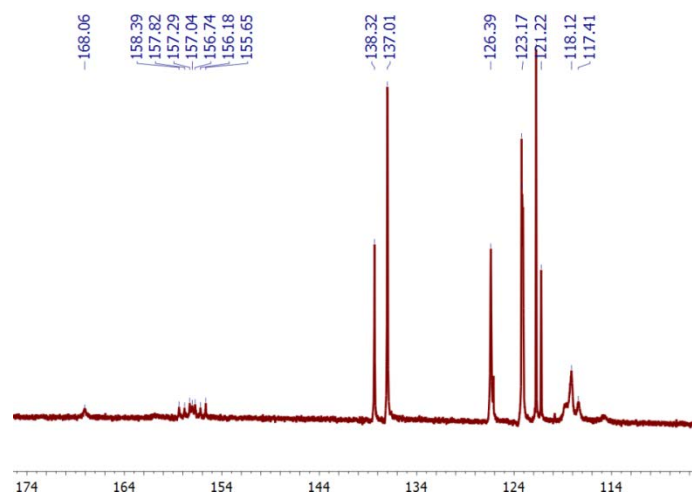


Figure 3.12 ^{13}C NMR spectrum of $\text{Al}(\text{OPh})_3/\text{PhMgCl}$ in THF; peak assignments are listed in Table 3-1.

Table 3-1 Summary of ^{13}C NMR spectra of $\text{Al}(\text{OPh})_3/\text{PhMgCl}$ electrolyte in THF.

| Peak shift (ppm) (splitting) | Peak Identity |
|------------------------------|---------------|
| 169.7 (singlet) | Ph-Mg |
| 158 (sextet) | Ph-Al |
| 158.6 (singlet) | PhO-Al |
| 139.9 (singlet) | Ph-Mg |
| 138.6 (singlet) | Ph-Al |
| 128.0 (singlet) | Ph |
| 124.7 (singlet) | Ph-Mg |
| 123.4 (singlet) | Ph-Al |
| 122.8 (singlet) | Pho-Al/Ph-Al |
| 119.7-119.0 (multiplet) | PhO-Al/PhMg |

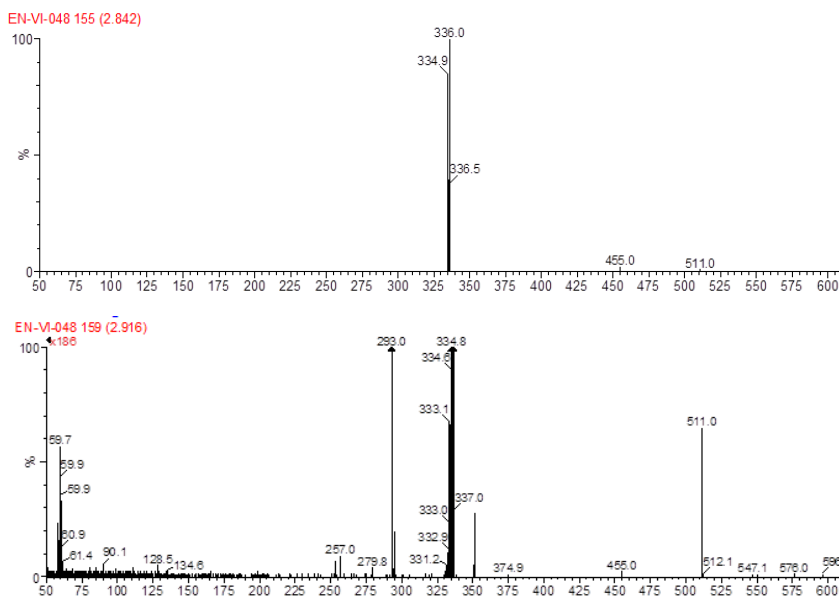


Figure 3.13 Electrospray ionization mass spectra in negative ionization mode of $\text{Al}(\text{OPh})_3/\text{PhMgCl}$ giving $\text{Al}(\text{Ph})_4^-$ (m/z 335), upon magnification the following species are found: $\text{Al}(\text{Ph})_3\text{Cl}^-$ (294), $\text{Al}(\text{Ph})_3(\text{OPh})^-$ (352).

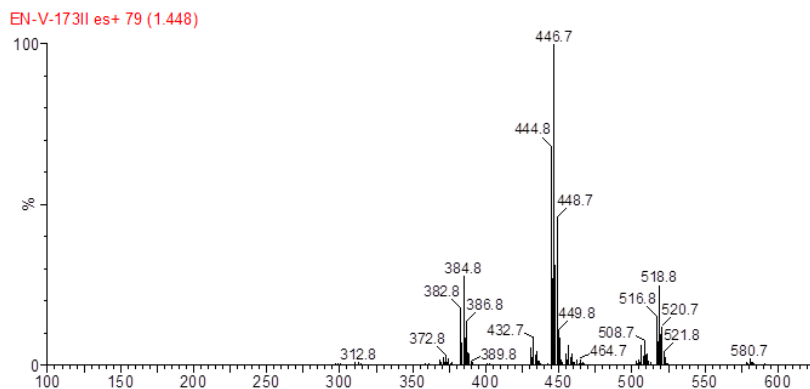


Figure 3.14 Electrospray ionization mass spectra positive ionization mode of $\text{Al}(\text{OPh})_3/\text{PhMgCl}$ giving the following species: $\text{Mg}_2\text{Cl}_3(\text{THF})_4^+$ (446), $\text{Mg}_2(\text{OPh})_3\text{Cl}(\text{THF})_2^+$ (508), $\text{Mg}_2\text{Cl}_3(\text{THF})_5^+$ (518)

Switching to positive-ion mode shows the presence of the most common $\text{Mg}_2\text{Cl}_3(\text{THF})_4^+$ dimer as well as the phenolate bridged species $\text{Mg}_2(\text{OPh})_3\text{Cl}(\text{THF})_2^+$ (Figure 3.14). Neutral Mg-phenolate complexes showing a phenolate bridge have been crystallized and are presented in Figure 3.15 and Figure 3.16. The Mg_2Cl_3^+ is most commonly named as the “active” Mg species in solution, although some recent work suggests it may only be a precursor for Mg deposition.^{79,80} Due to the presence of two

apparent binding environments of Mg in solution, it is unclear as to which one, or if both, contribute to Mg deposition.

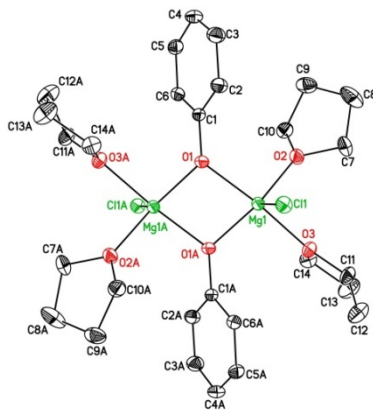


Figure 3.15 One X-ray crystal structure of the neutral Mg species, $C_{28}H_{42}Cl_2Mg_2O_6$ isolated from a 1:4 $Al(OPh)_3/PhMgCl$ electrolyte solution.

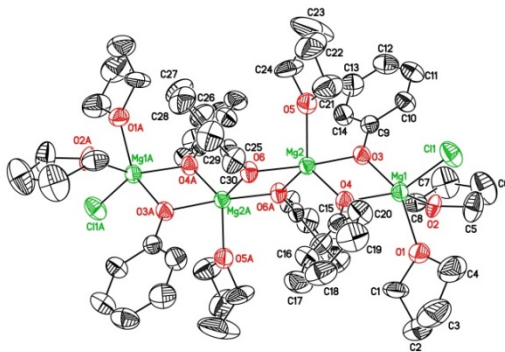


Figure 3.16 Second X-ray crystal structure of the neutral Mg species, $C_{60}H_{78}Cl_2Mg_4O_{12}$ isolated from a 1:4 $Al(OPh)_3/PhMgCl$ electrolyte solution.

The combination of the ESI-MS analysis, ^{13}C and ^{27}Al NMR spectroscopy, and the isolated X-ray crystal structures show that the ligand exchange between the magnesium and aluminum starting materials may not be complete, with some Ph-Mg and PhO-Al bonds still present. This complication along with the Schlenk equilibria among these

species at room temperature makes the complete characterization of all the species in the electrolyte solution of a functioning battery very complex.

3.3 Conclusion

Eliciting the factors relevant for controlling oxidative stability and improving the compatibility of Mg-ion electrolytes with commercially relevant current collectors and battery casings such as stainless steel is crucial for the next-generation (beyond Li-ion) electrical energy storage. Here, the decreased chloride content in Mg-ion electrolytes by switching the Lewis acid from AlCl_3 to $\text{Al}(\text{OPh})_3$ shows improved stability on both Pt and stainless-steel electrodes. We observe minimal pitting on stainless steel after electrolysis at 4.5 V vs $\text{Mg}^{2+/0}$ for 96 hours compared to the extreme pitting observed in the more widely reported APC electrolyte after only 24 hours. The unprecedented stability of this electrolyte suggests that the stability may be explained by more than simply eliminating chloride from the starting Lewis acid. In particular, an in-depth consideration of solution speciation is of interest as a way to 1) understand what molecular species result in reversible deposition/stripping, and 2) to determine what factors contribute most significantly to oxidative stability. Such an understanding would not only help in simplifying the overall electrolyte system, but would also assist in the synthetic progress of future electrolytes.

3.4 Experimental

3.4.1 General Considerations

Phenylmagnesium chloride, trimethylaluminum and phenol were purchased from Sigma Aldrich, and used as received. Tetrahydrofuran solvent was purchased from VWR, and distilled over sodium with a benzophenone-ketyl indicator. ^{27}Al NMR spectroscopy was performed on a Varian VNMR-700 MHz spectrometer in THF with chemical shifts reported relative to a solution of AlCl_3 in D_2O with a drop of concentrated HCl. ^1H , and ^{13}C NMR spectroscopy was performed on a Varian MR-400 MHz spectrometer in THF. Conductivity measurements were carried out using a YSI Model 3200 conductivity meter equipped with a 3253 conductivity cell at room temperature. Mass spectrometry was

performed on a Micromass LCT Time-of-Flight mass spectrometer with electrospray ionization.

3.4.2 Synthesis

All compounds were prepared and handled using standard Schlenk techniques under N_2 and a N_2 -filled glove box (Vacuum Atmospheres). Aluminum triphenoxide was made through the slow addition of 10 mL of $Al(Me)_3$ (2M, 20mmol) to a solution of phenol in THF (10mL, 6M, 60mmol) in a Schlenk flask. The solution was stirred for 3 hours and the solvent removed in vacuo. The powder was brought into the glove box and recrystallized from diffusion of Hexane into a THF solution. The $PhMgCl-Al(OPh)_3$ electrolyte was synthesized through addition of a 0.5 M $Al(OPh)_3$ in THF (2mL, 1mmol) to a solution of $PhMgCl$ (6mL, 4mmol) in THF. The solution was stirred for at least 6 hours.

3.4.3 Electrochemistry

Cyclic voltammograms were recorded using a CH Instruments Electrochemical Workstation 1000A with a Pt-disk working electrode and Mg-foil counter- and reference electrodes. Measurements were carried out at a scan rate of 25 mV/s, starting at OCP (ranging from 1.5 – 1.7 vs $Mg^{2+/0}$) and scanned cathodically. All electrolyte solutions were 0.5 M (based on Mg) in THF, and measurements were performed using a custom-designed sealed cell in an N_2 box to avoid concentration change during the measurements. The slurry of Mo_6S_8 or WSe_2 was made by mixing an 8:1:1 weight-ratio mixture of Mo_6S_8 , super-P carbon powder, and polyvinylidene fluoride (PVDF) binder in N-methyl-2-pyrrolidinone (NMP). The cathode slurry was placed on an Al current collector and dried in an oven at 120 °C. The active material loading was approximately 2 mg/cm^2 . The cathode was placed in an electrochemical cell with a Mg foil anode. The charge-discharge tests of the cell were carried on a Vencon UBA4 battery analyser charger and conditioner (Toronto, Canada) with cut-off voltages of 2.0 and 0.2 V vs. $Mg^{2+/0}$.

3.5 X-ray Structure Determination for C₂₈H₄₂O₆Mg₂Cl₂ (CCDC # 999561)

Colorless needles of **en52** were grown from a tetrahydrofuran/hexane solution of the compound at 22 deg. C. A crystal of dimensions 0.14 x 0.04 x 0.03 mm was mounted on a Rigaku AFC10K Saturn 944+ CCD-based X-ray diffractometer equipped with a low temperature device and Micromax-007HF Cu-target micro-focus rotating anode ($\lambda = 1.54187$ Å) operated at 1.2 kW power (40 kV, 30 mA). The X-ray intensities were measured at 85(1) K with the detector placed at a distance 42.00 mm from the crystal. A total of 4146 images were collected with an oscillation width of 1.0° in ω . The exposure time was 2 sec. for the low angle images, 10 sec. for high angle. The integration of the data yielded a total of 42069 reflections to a maximum 2θ value of 136.48° of which 2810 were independent and 2519 were greater than $2\sigma(I)$. The final cell constants (Table 3-2) were based on the xyz centroids 26696 reflections above $10\sigma(I)$. Analysis of the data showed negligible decay during data collection; the data were processed with CrystalClear 2.0 and corrected for absorption. The structure was solved and refined with the Bruker SHELXTL (version 2008/4) software package, using the space group $P2_1/c$ with $Z = 2$ for the formula C₂₈H₄₂O₆Mg₂Cl₂. The complex lies on an inversion center of the crystal lattice. All non-hydrogen atoms were refined anisotropically with the hydrogen atoms placed in idealized positions. Full matrix least-squares refinement based on F^2 converged at $R1 = 0.0436$ and $wR2 = 0.1229$ [based on $I > 2\sigma(I)$], $R1 = 0.0463$ and $wR2 = 0.1257$ for all data. Additional details are presented in Table 3-2. Acknowledgement is made for funding from NSF grant CHE-0840456 for X-ray instrumentation.

Table 3-2 Crystal data and structure refinement for en52 (CCDC #999561)

| | |
|-----------------------------|--|
| Identification code | en52 |
| Empirical formula | C ₂₈ H ₄₂ Cl ₂ Mg ₂ O ₆ |
| Formula weight | 594.14 |
| Temperature | 85(2) K |
| Wavelength | 1.54178 Å |
| Crystal system, space group | Monoclinic, $P2_1/c$ |
| Unit cell dimensions | $a = 7.23120(10)$ Å $\alpha = 90^\circ$ $b = 10.8165(2)$ Å $\beta = 92.125(7)^\circ$ $c = 19.6313(14)$ Å $\gamma = 90^\circ$ |
| Volume | 1534.43(12) Å ³ |

| | |
|--|--|
| Z, ρ_{calc} | 2, 1.286 g/cm ³ |
| Absorption coefficient | 2.616 mm ⁻¹ |
| $F(000)$ | 632 |
| Crystal size | 0.20 x 0.20 x 0.20 mm |
| θ range for data collection | 4.51 – 68.24° |
| Limiting indicies | $-8 \leq h \leq 8$ $-13 \leq k \leq 12$ $-23 \leq l \leq 23$ |
| Reflections collected/unique | 42069 / 2810 [$R(\text{int}) = 0.0751$] |
| Completeness to $\theta = 68.24^\circ$ | 100% |
| Absorption correction | Semi-empirical from equivalents |
| Max. and min. transmission | 0.6228 and 0.6228 |
| Refinement method | Full-matrix least-squares on F^2 |
| Data / restraints / parameters | 2810 / 0 / 172 |
| $G.o.F.$ on F^2 | 1.139 |
| Final R indices [$I > 2\sigma(I)$] | $R1 = 0.0436$; $wR2 = 0.1229$ |
| R indices (all data) | $R1 = 0.0463$, $wR2 = 0.1257$ |
| Largest diff. peak and hole | 0.836 and -0.548 eA^{-3} |

3.6 X-ray Structure Determination for C₆₀H₇₈O₁₂Mg₄Cl₂ (CCDC # 999562)

Colorless block-like crystals of **en5153** were grown from a tetrahydrofuran solution of the compound at 22 deg. C. A crystal of dimensions 0.25 x 0.25 x 0.25 mm was sealed in epoxy and mounted on a Rigaku AFC10K Saturn 944+ CCD-based X-ray diffractometer equipped with a low temperature device and Micromax-007HF Cu-target micro-focus rotating anode ($\lambda = 1.54187 \text{ \AA}$) operated at 1.2 kW power (40 kV, 30 mA). The X-ray intensities were measured at 250(1) K with the detector placed at a distance 42.00 mm from the crystal. A destructive phase change prevented data collection at lower temperature. A total of 4088 images were collected with an oscillation width of 1.0° in ω . The exposure time was 1 sec. for the low angle images, 8 sec. for high angle. The integration of the data yielded a total of 75202 reflections to a maximum 2θ value of 136.50° of which 5663 were independent and 5345 were greater than $2\sigma(I)$. The final cell constants (Table 3-3) were based on the xyz centroids 46672 reflections above $10\sigma(I)$. Analysis of the data showed negligible decay during data collection; the data were processed with CrystalClear 2.0 and corrected for absorption. The structure was solved and refined with the Bruker SHELXTL (version 2008/4) software package, using the space group P2(1)/n with $Z = 2$ for the formula C₆₀H₇₈O₁₂Cl₂Mg₄. All non-hydrogen

atoms were refined anisotropically with the hydrogen atoms placed in idealized positions. The complex lies on an inversion of the crystal lattice located at the mid-point of Mg2 and Mg2a. The bound THF ligands show considerable conformational disorder and were each modeled in three discrete resolved positions utilizing suitable restraints and partial occupancy atoms. Full matrix least-squares refinement based on F^2 converged at $R1 = 0.0343$ and $wR2 = 0.0915$ [based on $I > 2\sigma(I)$], $R1 = 0.0358$ and $wR2 = 0.0927$ for all data. Additional details are presented in Table 3-3. Acknowledgement is made for funding from NSF grant CHE-0840456 for X-ray instrumentation.

Table 3-3 Crystal data and structure refinement for en5153 (CCDC # 999562)

| | |
|--|---|
| Identification code | en5153 |
| Empirical formula | $C_{60}H_{78}Cl_2Mg_4O_{12}$ |
| Formula weight | 1159.36 |
| Temperature | 250(2) K |
| Wavelength | 1.54178 Å |
| Crystal system, space group | Monoclinic, $P2_1/n$ |
| Unit cell dimensions | $a = 12.8707(7)$ Å $\alpha = 90^\circ$ $b = 19.0698(4)$ Å $\beta = 102.113(4)^\circ$ $c = 12.8991(7)$ Å $\gamma = 90^\circ$ |
| Volume | $3095.5(2)$ Å ³ |
| Z, ρ_{calc} | 2, 1.244 g/cm ³ |
| Absorption coefficient | 1.810 mm ⁻¹ |
| $F(000)$ | 1232 |
| Crystal size | 0.25 x 0.25 x 0.25 mm |
| θ range for data collection | 4.64 – 68.25° |
| Limiting indices | $-15 \leq h \leq 15$ $-22 \leq k \leq 22$ $-15 \leq l \leq 15$ |
| Reflections collected/unique | 75202 / 5663 [$R(int) = 0.0523$] |
| Completeness to $\theta = 68.25^\circ$ | 99.8% |
| Absorption correction | Semi-empirical from equivalents |
| Max. and min. transmission | 0.6604 and 0.6604 |
| Refinement method | Full-matrix least-squares on F^2 |
| Data / restraints / parameters | 5663 / 448 / 631 |
| $G.o.F.$ on F^2 | 1.053 |
| Final R indices [$I > 2\sigma(I)$] | $R1 = 0.0343$; $wR2 = 0.0915$ |
| R indices (all data) | $R1 = 0.0358$, $wR2 = 0.0927$ |
| Largest diff. peak and hole | 0.203 and -0.236 eÅ ⁻³ |

Sheldrick, G.M. SHELXTL, v. 2008/4; Bruker Analytical X-ray, Madison, WI, 2008.

CrystalClear Expert 2.0 r12, Rigaku Americas and Rigaku Corporation (2011), Rigaku Americas, 9009, TX, USA 77381-5209, Rigaku Tokyo, 196-8666, Japan.

3.7 References

- 63 Ichitsubo, T., Adachi, T., Yagi, S., Doi, T. Potential Positive Electrodes for High-Voltage Magnesium-Ion Batteries, *J. Mater. Chem.*, **2011**, *21*, 11764-11772
- 64 Muldoon, J., Bucur, C., Oliver, A., Sugimoto, T., Matsui, M., Kim, H., Allred, G., Zajicek, J., Kotani, Y. Electrolyte Roadblocks to a Magnesium Rechargeable Battery, *Energy Environ. Sci.*, **2012**, *5*, 5941-5950
- 65 Guo, Y., Zhang, F., Yang, J., Wang, F., NuLi, Y., Hirano, S. Boron-Based Electrolyte Solutions with Wide Electrochemical Windows for Rechargeable Magnesium Batteries, *Energy Environ. Sci.*, **2012**, *5*, 9100-9106
- 66 Muldoon, J., Bucur, C. B., Oliver, A. G., Zajicek, J., Allred, G. D., Boggess, W. C., Corrosion of Magnesium Electrolytes: Chlorides – the Culprit, *Energy Environ. Sci.*, **2013**, *6*, 482-487
- 67 Yagi, S., Tanaka, A., Ichikawa, Y., Ichitsubo, T., Matsubara, E. Electrochemical Stability of Magnesium Battery Current Collectors in a Grignard Reagent-Based Electrolyte, *J. Electrochem. Soc.*, **2013**, *160*, C83-C88
- 68 Chen, Y., Liui, T., Shao, Y., Engelhard, M., Liu, J., Li, G. Electrochemically Stable Cathode Current Collector for Rechargeable Magnesium Batteries, *J. Mater. Chem. A.*, **2014**, *2*, 2473-2477
- 69 Nelson, E.G., Kampf, J. W., Bartlett, B.M., Enhanced Oxidative Stability of non-Grignard Magnesium Electrolytes through Ligand Modification, *Chem. Commun.*, **2014**, *50*, 5193-5195
- 70 Wang, F., Guo, Y., Yang, J., Nuli, Y., Hirano, S. A Novel Electrolyte System without a Grignard Reagent for Rechargeable Magnesium Batteries, *Chem. Commun.*, **2012**, *48*, 10763-10765
- 71 Guo, Y., Zhang, F., Yang, J., Wang, F., NuLi, Y., Hirano, S. Boron-based Electrolyte Solutions with Wide Electrochemical Windows for Rechargeable Magnesium Batteries, *Energy Environ. Sci.*, **2012**, *5*, 9100-9106
- 72 Pour, N., Gofer, Y., Major, D. T., Aurbach, D. Structural Analysis of Electrolyte Solutions for Rechargeable Mg Batteries by Stereoscopic Means and DFT Calculations, *J. Am. Chem. Soc.*, **2011**, *133*, 6270-6278
- 73 Liu, B., Luo, T., Mu, G., Wang, X., Chen, D., Shen, G. Rechargeable Mg-Ion Batteries Based on WSe₂ Nanowire Cathodes, *ACS Nano*, 2013, *7*, 8051-8058
- 74 Kershaw, R., Vlasse, M., Wold, A., The Preparation and Electrical Properties of Niobium Selenide and Tungsten Selenide, *Inorg. Chem.*, **1967**, *6*, 1599-1602
- 75 Ichitsubo, T., Adachi, T., Yagi, S., Doi, T. Potential Positive Electrodes for High-Voltage Magnesium-ion Batteries, *J. Mater. Chem.*, **2011**, *21*, 11764-11772
- 76 Huang, Z., Mases, T., Orikasa, Y., Mori, T., Minato, T., Tassel, C., Kobayashi, Y., Kageyama, H., Uchimoto, Y. MgFePO₄F as a Feasible Cathode Material for Magnesium Batteries, *J. Mater. Chem. A*, **2014**, *2*, 11578-11582

- 77 Pour, N., Gofer, Y., Major, D. T., Aurbach, D., Structural Analysis of Electrolyte Solutions for Rechargeable Mg Batteries by Stereoscopic Means and DFT Calculations, *J. Am. Chem. Soc.*, **2011**, *133*, 6270-6278
- 78 Pour, N., Gofer, Y., Major, D. T., Keinan-Adamsky, K., Gottlieb, H. E., Aurbach, D. Multinuclear Magnetic Resonance Spectroscopy and Density Function Theory Calculations for the Identification of the Equilibrium Species in THF Solutions of Organometallic Complexes Suitable As Electrolyte Solutions for Rechargeable Mg Batteries, *Organometallics*, **2013**, *32*, 3165-3173
- 79 Benmayza, A., Ramanathan, M., Arthur, T. S., Matsui, M., Mizuno, F., Guo, J., Glans, P., Prakash, J., Effect of Electrolytic Properties of a Magnesium Organohaloaluminate Electrolyte on Magnesium Deposition, *J. Phys. Chem. C.*, **2013**, *117*, 26881-26888
- ⁸⁰ Mohtadi, R., Matsui, M., Arthur, T. S., Hwang, S. J. Magnesium Borohydride: From Hydrogen Storage to Magnesium Battery, *Angew. Chem., Int. Ed.*, **2012**, *51*, 9780-9783

CHAPTER 4

Surface and Electrochemical Characterization of Carbon Passivation Layer

Portions of this chapter have been published:

Nelson, E. G.; Brody S. I.; Kampf, J. W.; Bartlett, B. M. *J. Mater. Chem. A*, 2014, **2**, 18194-18198. Reproduced by permission of the Royal Society of Chemistry
<http://pubs.rsc.org/en/content/articleLanding/2014/TA/c4ta04625k>

4.1 Introduction

Chapter 3 introduced an electrolyte in THF with an apparent oxidative stability stability out to 5 V vs $\text{Mg}^{2+/0}$. As mentioned in the previous chapter, the oxidative stability of THF alone is 3.2 V vs $\text{Mg}^{2+/0}$, which suggests a kinetically stable passivation layer forms on the surface of the working electrode. The formation of a passivation layer is a common concept in describing the stability of Li-ion batteries. Figure 4.1 shows a representation of the relative energies of the electrodes and electrolyte in a battery cell. The energy separation of the lowest unoccupied molecular orbital (LUMO) and highest occupied molecular orbital (HOMO) of the electrolyte is the so-called “working window” of the electrolyte. The two electrodes are electronic conductors with the anode and cathode chemical potentials denoted μ_A and μ_C . An anode with μ_A above the LUMO will reduce the electrolyte until a passivation layer creates a barrier to electron transfer from the anode to the electrolyte LUMO. In the case of the cathode with a μ_C below the HOMO, the electrolyte will be oxidized until a passivation layer blocks the electron transfer from the HOMO. Therefore, to ensure thermodynamic stability μ_A and μ_C are constrained to fall within the window of the electrolyte.⁸¹ This limits the open circuit voltage of the battery cell to

$$eV_{OC} = \mu_A - \mu_C \leq E_g \quad (4-1)$$

where e is the magnitude of the electron charge and E_g is the HOMO-LUMO gap energy. A passivating solid / electrolyte interface (SEI) layer at the electrode/electrolyte boundary can give kinetic stability to a larger V_{OC} providing $eV_{OC} - E_g$ is not too large.

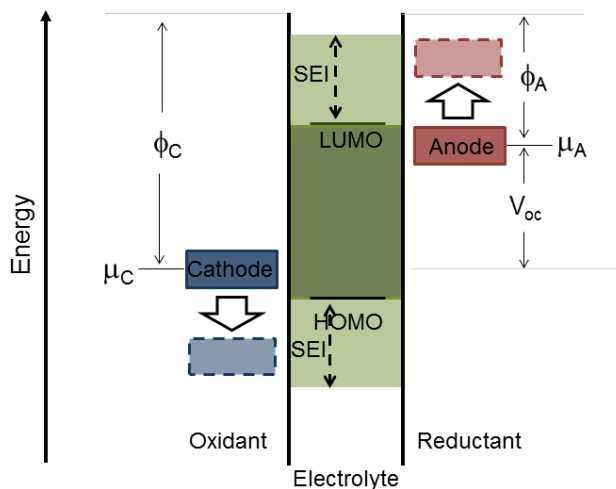


Figure 4.1 Open-circuit energy diagram of a battery system.

The SEI layer proceeds from the deposition of organic and inorganic compounds. The formation, composition, and stability of the SEI depends on both the composition of the electrolyte (solvent, additives, salt) and the charge and discharge rate.^{82,83} In all cases the SEI in Li-ion systems acts as a good electronic insulator and a good ionic conductor for Li ions.

The electrochemical performance of the $\text{Al(OPh)}_3/\text{PhMgCl}$ electrolyte discussed in chapter 3 provides a system in which to examine the possibility of an ionically conducting yet electronically isolating material, which has yet to be reported in a Mg-ion electrolyte.⁸⁴⁻⁸⁶ The focus of this chapter is to scrutinize the composition and electrochemical characteristics of this passivation layer.

4.2 Results and Discussion

As shown in Figure 3.1, the electrochemical performance of $\text{Al(OPh)}_3/\text{PhMgCl}$ at higher voltages shows positive current spikes which could suggest a break and repair mechanism in a passivating layer. In an effort to scrutinize this possibility, XP spectra of the Pt foil before and after soaking in the electrolyte and cycling the electrolyte solution

are presented in Figures 4.2 – 4.4.

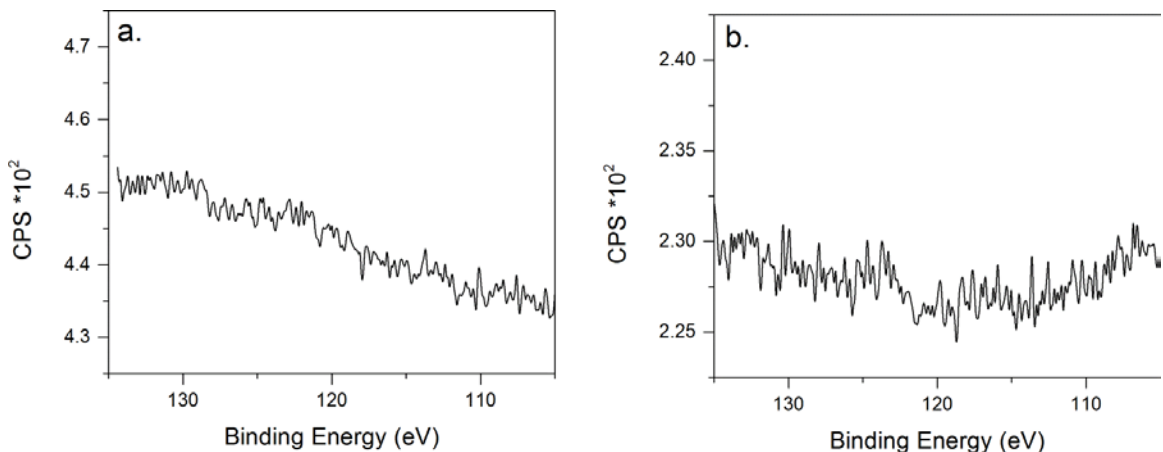


Figure 4.2 a.) Al 2s XP spectra of Pt soaked in THF for 20 minutes; b.) Al 2s XP spectra of Pt after cycling 20 times in Al(OPh)₃:4PhMgCl electrolyte from 0-5V.

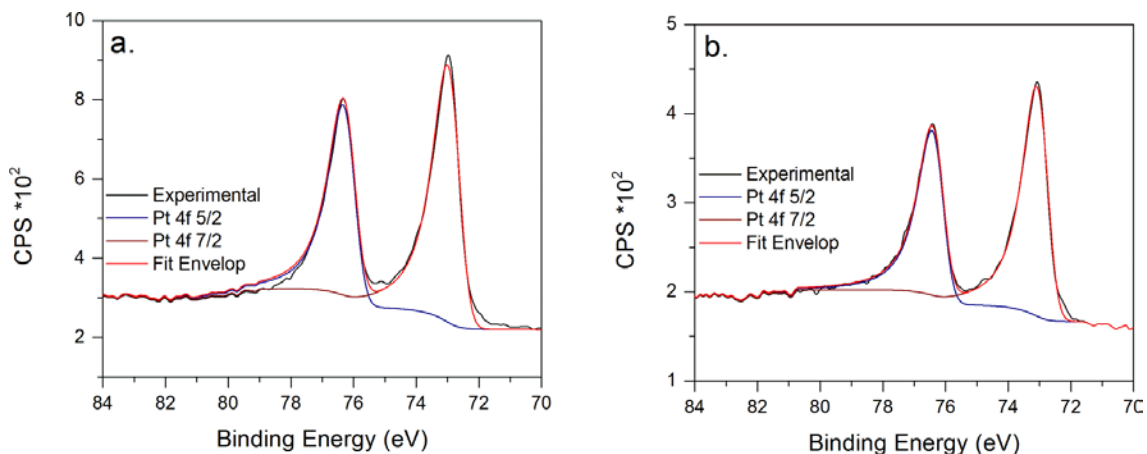


Figure 4.3 a.) Pt 4f XP spectra of Pt after cycling 20 times in Al(OPh)₃:4PhMgCl electrolyte from 0-5 V; b.) Pt 4f XP spectra of Pt soaked in THF for 20 minutes.

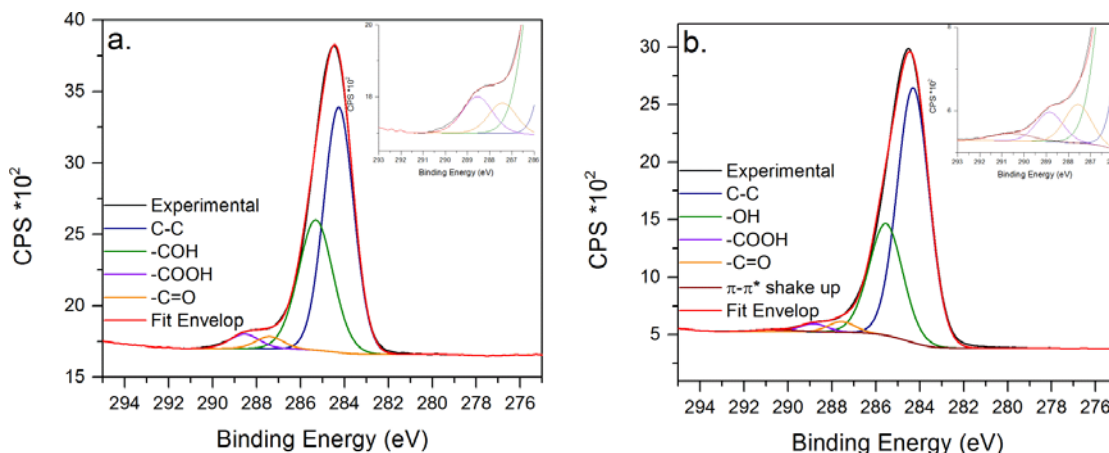


Figure 4.4 a.) C 1s XP spectra of Pt soaked in THF for 20 minutes, b.) C 1s XP spectra of Pt after cycling 20 times in $\text{Al(OPh)}_3:4\text{PhMgCl}$ electrolyte from 0-5 V.

Fitting the C(1s) peak after cycling in the electrolyte shows a new peak at 290.5 eV. This broad peak is ascribed to a $\pi - \pi^*$ shake-up peak, attributed to benzene/phenyl carbon. The complete absence of an Al(2s) peak after cycling demonstrates that the 290.5 eV peak does not result from adsorbed AlPh_4^- , but shows the possibility of free benzene/phenyl carbon adsorbed to the Pt metal surface after electrochemical cycling. The observation of an aromatic carbon adsorption layer on Pt is not surprising given that the affinity for carbon to the surface of Pt has been well reviewed.⁸⁷ The presence of this peak only after cycling shows that any possible mechanism for passivation occurs through an electrochemical phenomenon, and the absence of a change in the Pt XP spectra suggests the any interaction is non-bonding to the Pt surface.

In contrast, XP spectra recorded on stainless steel do not show the appearance of an additional carbon species cycling in the electrolyte (Figure 4.5). This absence of a $\pi - \pi^*$ shake up peak, as well as the absence of the current spikes observed on Pt suggests the benzene/phenyl species do not exhibit any significant adsorption onto stainless steel.

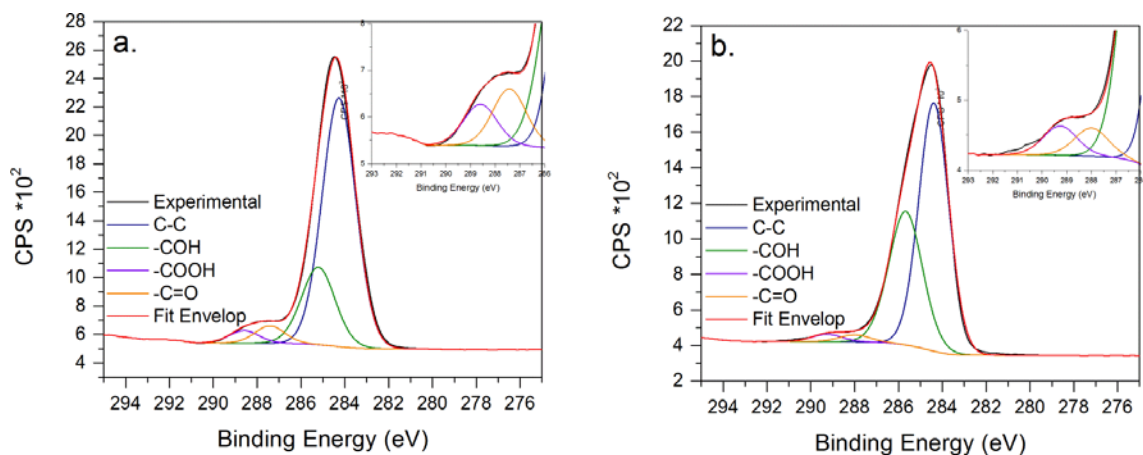


Figure 4.5 a.) C 1s XPS spectra of stainless steel soaked in THF for 20 minutes; b.) C 1s XPS spectra of stainless steel after cycling 20 times in $\text{Al(OPh)}_3\text{:4PhMgCl}$ electrolyte from 0-5 V.

Although the appearance of an additional aromatic carbon peak after cycling on Pt shows a surface interaction with the electrolyte, it does not necessarily prove that it is electrochemically passivating. Adding LiPF_6 , which oxidizes to LiF and PF_5 at 5.5 V vs $\text{Li}^{+/0}$ (~ 4.2 V vs $\text{Mg}^{2+/0}$), to the electrolyte results in a decrease of the oxidation onset (Figure 4.6), which would not be expected if the layer were fully electrochemically passivating.

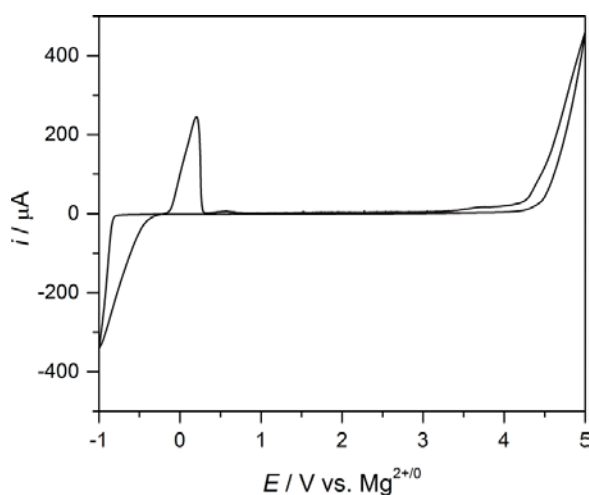


Figure 4.6 CV trace of 0.5 M LiPF_6 with 0.5 M $\text{Al(OPh)}_3\text{/PhMgCl}$ in THF

To probe how the ligands contribute to the SEI layer, the electrochemistry of APC, which has a well known oxidation potential of 3.2 V vs $\text{Mg}^{2+/0}$, with the addition of aromatic carbon species was examined. Adding benzene does not enhance the oxidative stability of the electrolyte, Figure 4.7a, showing that benzene does not play a role in the formation of an electrochemical passivation layer. However, adding phenyl lithium, (Figure 4.7b) does result in an increase in the onset of oxidation as well as a drop in the current density of Mg deposition and stripping showing the deprotonated phenyl is required for adsorption. Addition of both phenyl and benzene does, however, result in a decrease in current density for Mg deposition and stripping as well as an increase in overpotential for Mg deposition. These results suggest that a layer may inhibit both the anodic and cathodic electrode reactions.

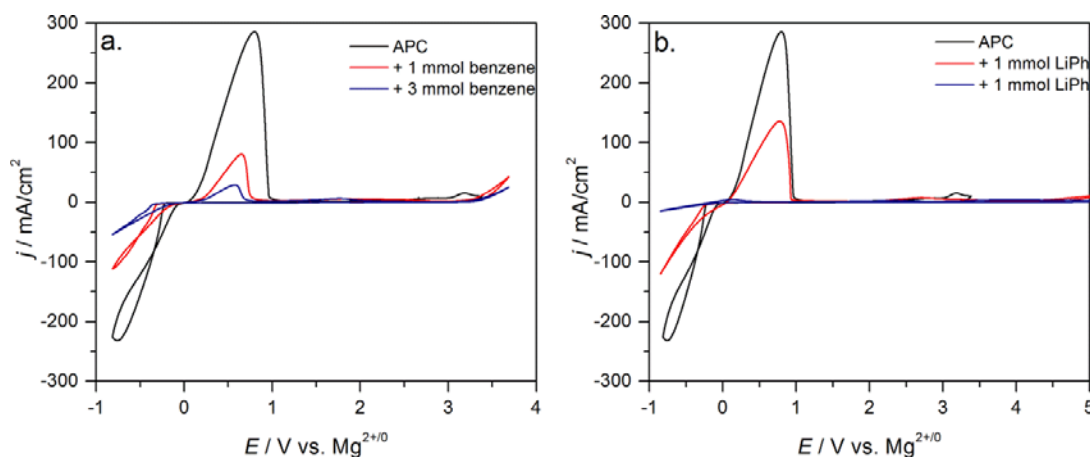


Figure 4.7 CV cycles of APC electrolyte with the addition of a.) benzene and b.) phenyl lithium with Mg foil counter and reference electrode, Pt working and scan rate of 25 mV/s.

The strong dependence on free phenyl begs the question if the additional Lewis acid is necessary for forming the passivation layer. To begin to answer this question, the electrochemistry of the Grignard reagent PhMgCl was also recorded. Figure 4.8a shows a CV trace of a 0.5 M solution of PhMgCl in THF to 3 V, with the oxidation potential of about 2 V vs $\text{Mg}^{2+/0}$, similar to what has been reported previously.⁸⁸ If this electrolysis window is expanded to 5 V (Figure 4.8b), the first scan shows the expected oxidation as well as other oxidation events at higher potentials, however, subsequent scans give an

apparent stability to 4.5 V vs $\text{Mg}^{2+/0}$. The change in the apparent oxidation potential between the first and subsequent scans again hints at the existence of a passivation layer.

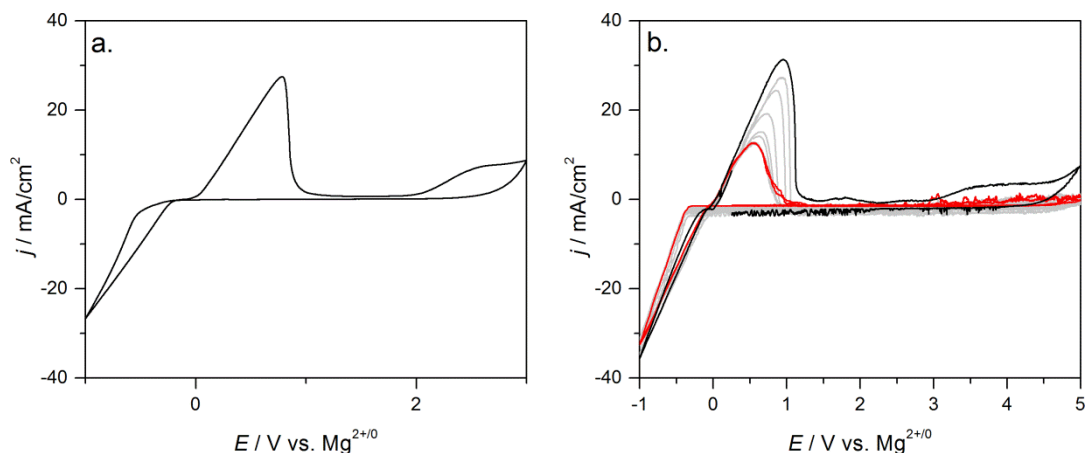


Figure 4.8 CV trace of 0.5 M PhMgCl in THF on a Pt electrode a) to 3 V and b) to 5V, the initial scan is shown in black, last scan in red, and middle scans in grey.

As the PhMgCl electrolyte is cycled, a drop in the Mg stripping current density is observed. This decrease in stripping current is not accompanied by a decrease in the deposition current, and thus a drastic decrease in the coulombic efficiency is observed, illustrated in Figure 4.9. The initial coulombic efficiency of 90% quickly drops to 30%, with occasional higher efficiencies of up to 45% observed. The absence of change in the deposition current suggests that the formed passivation layer does allow for Mg-ion conduction to the electrode. However, the drop in the Mg stripping efficiency suggests that the formed layer hinders the diffusion of Mg away from the electrode surface. In order to test this hypothesis, attempts to disrupt the formed passivation layer *in situ* were performed.

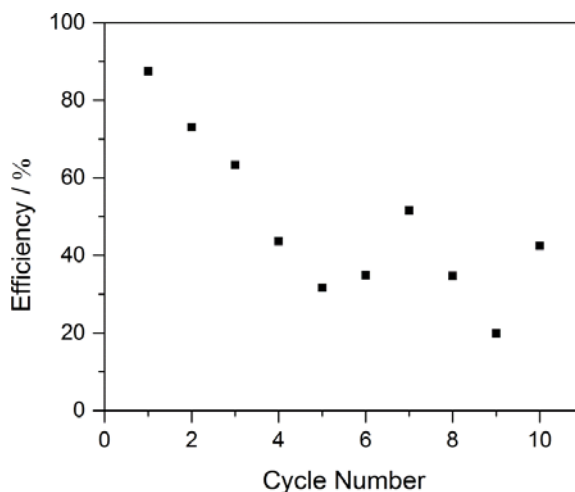


Figure 4.9 Efficiency of Mg deposition and stripping from 0.5 M PhMgCl as the electrolyte is cycled from -1 to 5 V vs $\text{Mg}^{2+/0}$.

Adding LiPF_6 to the solution after the CV curves shown in Figure 4.8b, and thus after forming the passivation layer, we observe a decrease in the onset of anodic current to 4.5 V vs $\text{Mg}^{2+/0}$ (Figure 4.10a). As with the PhMgCl/ $\text{Al}(\text{OPh})_3$ system shown in Figure 4.6, the decrease in anodic current suggests either this layer is not fully electrochemically passivating or the presence of other ions may interrupt/change the composition of the layer, allowing oxidation to occur. There is also an increase in the Mg stripping current, and although the coulombic efficiency never returns to its initial value, it does increase to a stable 50%, demonstrated in Figure 4.10b. Cycling the PhMgCl/ LiPF_6 solution with a freshly cleaned Pt electrode results in a coulombic efficiency that starts lower (70%) and then drops to 50%.

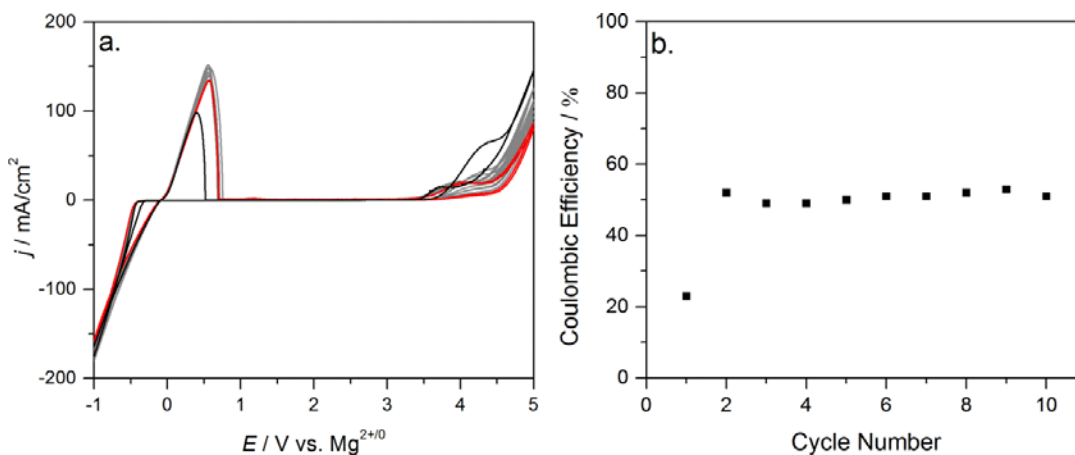


Figure 4.10 a.) CV curves of 0.5 M LiPF₆ added to 0.5 M PhMgCl after completing ten cycles prior to the addition of LiPF₆ b.) Coulombic efficiency of Mg deposition and stripping.

The decrease in oxidation potential and the restoration of the deposition-stripping efficiency in the presence of LiPF₆ suggests that the formed carbon layer is quasi-passivating, as it only appears to hinder the oxidation of certain species in solution. It also suggests that the layer is indeed Mg-ion conducting, although Mg²⁺ stripping is hindered to some extent by this layer.

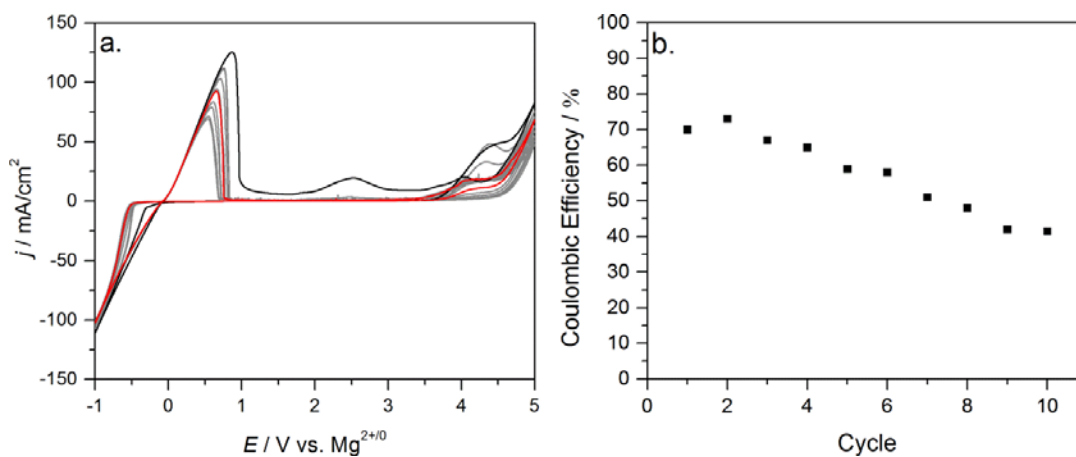


Figure 4.11 a.) CV trace of 0.5 M PhMgCl/LiPF₆ in THF on a Pt electrode 5V, the initial scan is shown in black, last scan in red, and middle scans in grey b.) Coulombic efficiency of Mg deposition and stripping.

In order to verify the apparent stability of this electrolyte and the ionic conductivity of the passivating SEI layer in a full battery system, intercalation experiments were performed. In the absence of a high-voltage magnesium cathode, reversible intercalation/deintercalation was carried out with LiMn_2O_4 . A 2016-type coin cell comprised of 0.5 M $\text{Al(OPh)}_3/\text{PhMgCl}$ in THF containing 0.5 M LiPF_6 , a LiMn_2O_4 cathode, and Mg foil anode was charged and discharged at room temperature at a rate of C/5 ($105 \mu\text{A}/\text{cm}^2$). Details of cell assembly are included in Section 4.4.

Figure 4.12 shows the charge-discharge curve in the potential window of 1 to 3.5 V vs $\text{Mg}^{2+/0}$. The initial discharge capacity is $\sim 100 \text{ mAh/g}$, but undergoes rapid capacity fade, likely due to the irreversible intercalation of Mg^{2+} into the smaller lithium-ion channels of the spinel structure. Despite the presence of this fade, the LiMn_2O_4 cathode does show the ability to intercalate/ deintercalate Li ions in the presence of the magnesium electrolyte. This observation suggests that the Mg electrolyte does not undergo electrochemical degradation within this potential window, testifying to the stability of this electrolyte, which extends at least up to 3.5 V vs. $\text{Mg}^{2+/0}$.

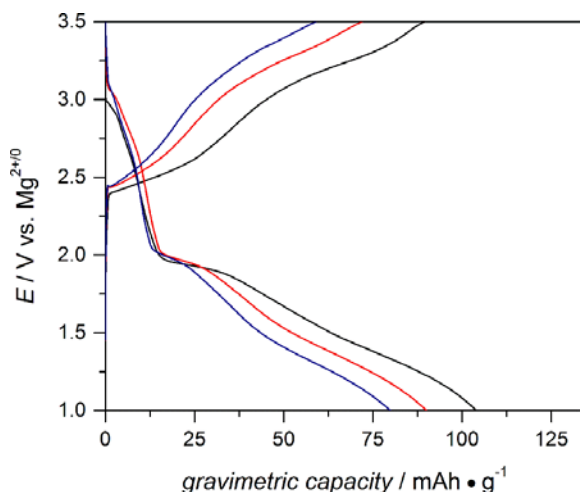


Figure 4.12 Typical charge/discharge profiles for a rechargeable battery with a LiMn_2O_4 cathode, 0.5 M $\text{Al(OPh)}_3/\text{PhMgCl}$ in THF with 0.5 M LiPF_6 , a Mg anode at cycles 1 (black), 5 (red), and 20 (blue).

Although Li^+ insertion/extraction demonstrates electrolyte stability and conduction of the passivation layer to ions, reversible Mg^{2+} insertion/extraction into a true magnesium host material must also be shown. As such, higher voltage Mg intercalation materials continue to be of interest.

4.3 Conclusion

The unique and unexpected stability of the $\text{PhMgCl}/\text{Al}(\text{OPh})_3$ system is attributed to a phenyl based passivation layer formed *in situ*. This SEI layer passivates the as-synthesized electrolyte and forms due to the presence of PhMgCl , hindering the diffusion of Mg^{2+} away from the surface of the metal electrode surface. This layer does not appear to interfere with the electrochemical cycling of battery material to 3.5 V vs $\text{Mg}^{2+/0}$. A comprehensive inspection of this phenomenon requires extensive electrochemical and surface-electrolyte analysis. Characterization of the electrochemical nature of this layer will include electrochemical impedance spectroscopy, atom probe tomography, and XPS to examine the resistance of the electrode before and after exposure to the $\text{Al}(\text{OPh})_3/\text{PhMgCl}$, APC, and PhMgCl solutions as well as before and after the deposition and stripping of Mg has taken place. An additional impedance experiment on the process of Mg deposition and stripping before and after formation of the layer is a much more complex, though profitable endeavor. The use of an electrochemical quartz crystal microbalance during Mg cycling will assist in discerning the interaction between electrolyte, electrode, and magnesium.

4.4 Experimental

4.4.1 General Considerations

Phenylmagnesium chloride, trimethylaluminum and phenol were purchased from Sigma Aldrich, and used as received. Tetrahydrofuran solvent was purchased from VWR, and distilled over sodium with a benzophenone-ketyl indicator. ^{27}Al NMR spectroscopy was performed on a Varian VNMRS-700 MHz spectrometer in THF with chemical shifts reported relative to a solution of AlCl_3 in D_2O with a drop of concentrated HCl. ^1H , and ^{13}C NMR spectroscopy was performed on a Varian MR-400 MHz spectrometer in THF. Conductivity measurements were carried out using a YSI Model 3200 conductivity meter

equipped with a 3253 conductivity cell at room temperature. Mass spectrometry was performed on a Micromass LCT Time-of-Flight mass spectrometer with electrospray ionization.

4.4.2 Synthesis

All compounds were prepared and handled using standard Schlenk techniques under N₂ and a N₂-filled glove box (Vacuum Atmospheres). Aluminum triphenoxide was synthesized through the slow addition of 10 mL of Al(Me)₃ (2 M, 20 mmol) to a solution of phenol in THF (10 mL, 6 M, 60 mmol) in a Schlenk flask. The solution was stirred for 3 hours and the solvent removed in vacuo. The powder was brought into the glove box and recrystallized from diffusion of hexane into a THF solution. The PhMgCl-Al(OPh)₃ electrolyte was synthesized through addition of a 0.5 M Al(OPh)₃ in THF (2mL, 1mmol) to a solution of PhMgCl (6mL, 4mmol) in THF. The solution was stirred for at least 6 hours. The PhMgCl-auxiliary salt electrolytes were synthesized in the same way with the addition of a 0.5 M X in THF (2 mL, 1mmol) to a solution of PhMgCl (6mL, 4mmol) in THF. The solution was stirred for at least 6 hours.

4.4.3 Electrochemistry

Cyclic voltammograms were recorded using a CH Instruments Electrochemical Workstation 1000A with a Pt-disk working electrode and Mg-foil counter- and reference electrodes. Measurements were carried out at a scan rate of 25 mV/s, starting at OCP (ranging from 0.5 – 1.2 V vs Mg^{2+/0}) and scanned cathodically. All electrolyte solutions were 0.5 M (based on Mg) in THF, and measurements were performed using a custom-designed sealed cell in an Ar box to avoid concentration change during the measurements.

4.5 References

- 81 Goodenough, J. B., Kim, Y., Challenges for Rechargeable Li Batteries, *Chem. Mater.*, **2010**, 22, 587-603
- 82 Ein-Ein, T., Markovsky, B., Aurbach, D., Carmeli, Y., Tamin, H., Luski, S. The Dependence of the Performance of Li-C Intercalation Anodes for Li-ion Secondary

- Batteries on the Electrolyte Solution Composition, *Electrochimica Acta*, **1994**, *39*, 2559-2569
- 83 Liebenow, C., Wagner, M.W., Luhder, K., Lobitz, P., Besenh. J.O. Electrochemical Behaviour of Coated Lithium-Carbon Electrodes, *Journal of Power Sources*, **1995**, *54*, 369-372
- 84 Aurbach, D., Weissman, I., Gofer, Y., Levi, E., Nonaqueous Magnesium Electrochemistry and its Application in Secondary Batteries, *Chem. Rec.* **2003**, *3*, 61-73
- 85 Gofer, Y., Pour, N., Aurbac, G. Electrolytic Solutions for Rechargeable Magnesium Batteries, *Lithium Batteries; Advanced Technologies and Applications*, Wiley-VCH: Weinheim, Germany, **2013**, 328-345
- 86 Lu, Z., Schechter, A., Moshkovich, M., Aurbach, W., On the Electrochemical Behavior of Magnesium Electrodes in Polar Aprotic Electrolyte Solutions, *J. Electroanal. Chem.* 1999, *466*, 203-217
- 87 Song, D., Sorianga, P., Hubbard, A. T. The Influence of Organic Solvents on Aromatic Adsorption at Platinum: Acetic Acid, Acetone, Acetonitrile, Dimethylacetamide, Dimethylsulfoxide, Sulfolane, and Tetrahydrofuran, *J. Electrochem. Soc.*, **1987**, *134*, 874-880
- 88 a.) Aurbach, D., Schechter, A., Moshkovich, M., Cohen, Y. On the Mechanisms of Reversible Magnesium Deposition Processes, *J. Electrochem. Soc.*, **2001**, *9*, A1004-A1014 b.) Guo, Y., Yang, J., Nuli, Y., Wang, J. Study of Electronic Effect of Grignard Reagents on their Electrochemical Behavior, *Electrochem. Commun.* **2010**, *12*, 1671-1673

CHAPTER 5

Molybdenum-Oxo Complex for Proton Reduction

5.1 Introduction

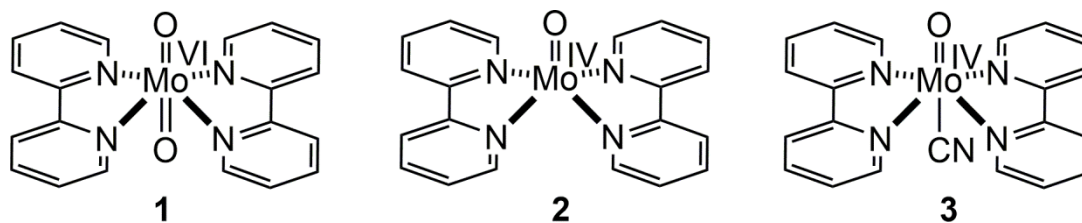
One of the current interests in the catalysis field focuses on catalyzing the small-molecule transformations of compounds for chemical energy storage. The increasing global demand for energy has made the search for renewable sources an important challenge.⁸⁹⁻⁹¹ Hydrogen is potentially an ideal energy carrier as it is non-polluting and gives up both of its electrons upon oxidation with oxygen to form water.⁹² However, to reach the full environmental benefits of hydrogen as an energy carrier, low-carbon intensive, low polluting, and lower cost processes for generating hydrogen from renewable resources need maturation. Current methods for hydrogen production are based on fossil fuels and lead to emissions of greenhouse gases.⁹³

Nature catalyzes the production and activation of hydrogen using the hydrogenase family of enzymes. These enzymes use metal-ion cores composed of iron and nickel, and show rapid hydrogen evolution of over 10^6 turnovers per second per active site.⁹⁴⁻⁹⁶ Synthetic catalysts have yet to reach turnover numbers of this magnitude, although this goal continues to drive research in the field.⁹⁷ Despite the increasing interest in photochemical catalysis, establishing an efficient photoactive complex remains a challenge.^{98,99} The production of H_2 from water involves multi-proton, multi-electron transfer reactions, along with formation and disassociation of chemical bonds. Thus, a catalyst must perform both proton-coupled electron transfer and bond making/breaking reactions¹⁰⁰

Early research in photo- and photoelectrochemical hydrogen production focused on molecular catalysts composed of precious metals such as iridium, rhodium and ruthenium.¹⁰¹ The reduction of ruthenium bipyridyl produced 3×10^{-6} mol of H_2 after

37 min of photolysis.^{102,103} Reducing protons by cobaltocene proceeded through a first-order reaction in both catalyst and protons with an observed rate constant of $42 \text{ M}^{-1}\text{s}^{-1}$.¹⁰⁴ In an effort to achieve higher turnover numbers and rates, research has begun to focus on biological mimics that take advantage of the ligand coordination sphere around the metal to assist with proton reduction.¹⁰⁵

Incorporating suitably basic ligands in the coordination sphere of a metal complex has allowed for creating efficient catalysts that employ more abundant metals such as nickel, iron and molybdenum.^{106,107} Recent work on molecular catalysts has led to the establishment of a pyridine based molybdenum-oxo electrocatalyst.¹⁰⁶ The proposed mechanism involves a two-electron reduction and protonation of the terminal oxo, forming bound water. This species is then proposed to undergo hydride abstraction forming a hydride-hydroxo species that finally releases molecular hydrogen through α -abstraction. This catalyst has turnover numbers of 8,500 moles of H_2 per mole of catalyst per hour in water.¹⁰⁸ Although this complex is a key step towards affordable, non-polluting H_2 , it still requires the input of 1 V of electrical energy to function. The ideal hydrogen catalyst would only use solar energy to function and incorporate only earth abundant metals.¹⁰⁹ Herein, we demonstrate electrocatalytic hydrogen evolution from *p*-toluenesulfonic acid (tosylic or tosic acid) in DMSO (effective $\text{p}K_{\text{a}} = 0.9$) using the molecular catalyst, $[(\kappa^2\text{-}2,2'\text{-bipyridyl})_2\text{Mo}\equiv\text{O}]^{2+}$. The advantage of this compound is that the supporting ligands are commercially available, and the compound is prepared straightforwardly in two steps and isolated as its hexafluorophosphate salt.



5.2 Results and Discussion

The successful synthesis is accomplished using freshly prepared $\text{MoO}_2(\text{acac})_2$ ¹¹⁰, which undergoes facile ligand substitution with 2,2'-bipyridine to yield the dioxo

bis(bipyridine) complex, $[(bpy)_2MoO_2](OH)_2$ (**1**), evidenced by 1H NMR spectroscopy and characteristic FTIR bands at 884 and 913 cm^{-1} , typical of *cis*-dioxomolybdenum(VI) complexes.¹¹¹ The reduction of (**1**) was completed using diphenylmethylphosphine. Anion exchange with tetraethylammonium hexafluorophosphate yields the desired molybdenum(IV) product, $[(bpy)_2MoO](PF_6)_2$ (**2**)^{112,113} The FTIR spectrum of the product shows conversion to one band in the metal-oxo stretching region at 946 cm^{-1} , illustrated in Figure 5.1.

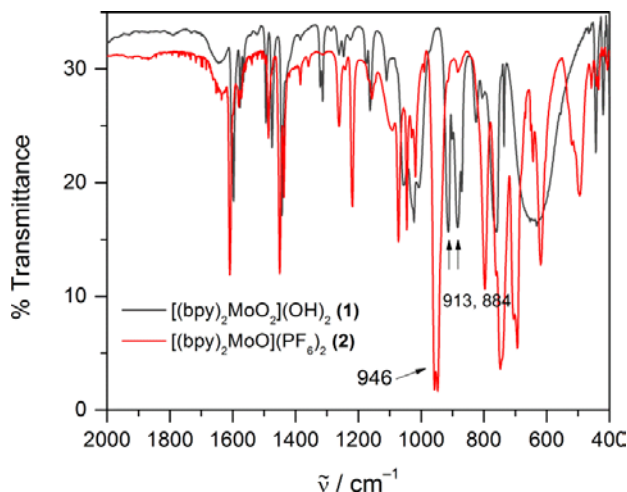


Figure 5.1 Infrared spectrum of $[(bpy)_2MoO_2](OH)_2$ (**1**) (gray) and $[(bpy)_2MoO](PF_6)_2$ (**2**) (red). The Mo–O vibrational stretches for the dioxo and mono-oxo are noted.

To establish the ability of complex **2** to catalyze proton reduction, the electrochemistry by cyclic voltammetry in the presence of acid was considered. First, Figure 5.2 shows a set of CV scans of **2** dissolved in DMSO (0.5 mM) with 0.1 M Bu_4NPF_6 as the supporting electrolyte. The experiment is performed using a glassy carbon working electrode, a platinum mesh auxiliary electrode, and the saturated calomel electrode in the presence of 0.5 M ferrocene as an internal reference. All scans start from -0.5 V $Fc^{+/0}$, the rest potential. In the absence of acid, no discernible electrochemistry is observed (lower black trace). However, adding 1 mol equivalent of TsOH results in the appearance of two irreversible redox couples: one at -1.5 V and the other at -1.85 V vs $Fc^{+/0}$ (0 V $Fc^{+/0}$ corresponds to $+0.624$ V NHE). The appearance of observable electrochemistry only after the addition of acid suggests a mechanism in which protonation of the complex of **2** occurs prior to the first electron transfer step.

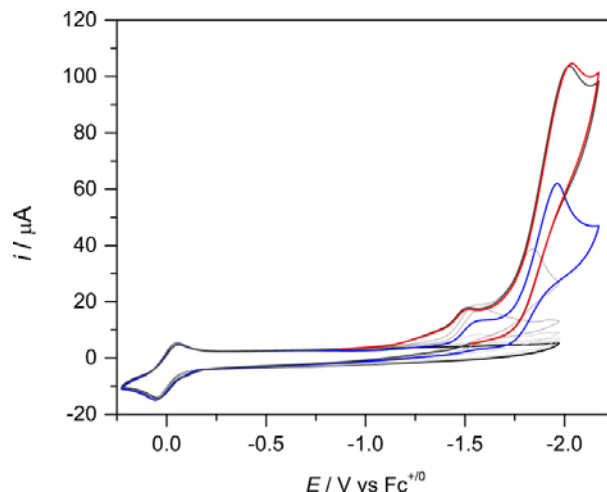


Figure 5.2 Cyclic voltammogram of a 0.5 M solution of **2** in DMSO containing 0.1 M Bu_4NPF_6 using a scan rate of 50 mV/s with a 1 mm diameter glass carbon working electrode. The concentration of TsOH increases from 0 mM (black), 25 mM (blue) and 50 mM (red). Intermediate concentrations 0.5, 1, 2.5, 5, 12.5 mM are shown in gray with the final concentration of 62.5 mM shown in black, overlaying with 50 mM [TsOH].

To determine if protonation occurs, the dependence of the first reduction at -1.5 V vs. $\text{Fc}^{+/0}$ on the amount of acid added can be inspected. If the first redox wave is considered to be a simple case where the reduced form of the redox couple is a strong Bronsted base, and the oxidised form is a weak base, the following reaction can be written:



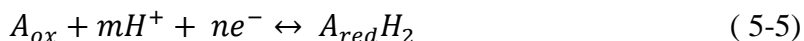
The Nernst equation for this reaction now includes the acidity (H^+)

$$E = E^o + \frac{2.3RT}{2F} \log \frac{[A_{ox}][H^+]^2}{[A_{red}H_2]} \quad (5-2)$$

$$E = E^o + \frac{2.3RT}{2F} \log \left(\frac{[A_{ox}]}{[A_{red}H_2]} \right) - 2 \left(\frac{2.3RT}{2F} \right) pH \quad (5-3)$$

$$E = E^o + \frac{2.3RT}{2F} \log \left(\frac{[A_{ox}]}{[A_{red}H_2]} \right) - 0.059VpH \quad (5-4)$$

The pH dependence term is written in red, and shows the reduction potential will decrease by 0.059 V per pH unit. In general a pH dependent reaction can be written as:



And the pH dependence is given by $-\left(0.059 \frac{m}{n}\right) pH$, where m is the number of protons and n the number of electrons.

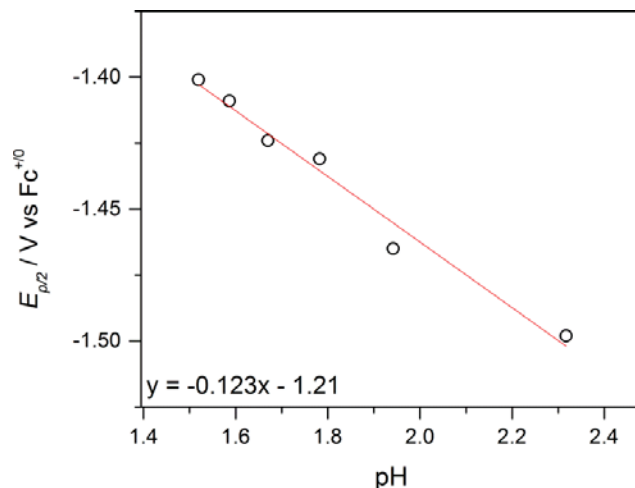


Figure 5.3 Plot of first reduction potential, $E_p/2$, versus pH of 0.5 mM (2) in DMSO with a scan rate of 0.5 mV/s. The linear least-squares fitted slope is 123 mV.

Using the concentration of acid and pK_a of TsOH in DMSO (0.9), a plot of the potential of the first reduction at $-1.5 \text{ V vs } Fc^{+/0}$ versus pH shows a linear fit with a slope of 123 mV, shown in Figure 5.3. Using the Nernst equation, the slope is twice the expected slope of 59 mV for a single proton coupled electron transfer (PCET) event, suggesting the first redox wave is a one-electron, two-proton reaction ($m=2$, $n=1$). Coupling this information with the necessity of acid for observable electrochemistry, the results suggest that the first step in the catalytic cycle is a single electron reduction and di-protonation of the terminal oxo group.

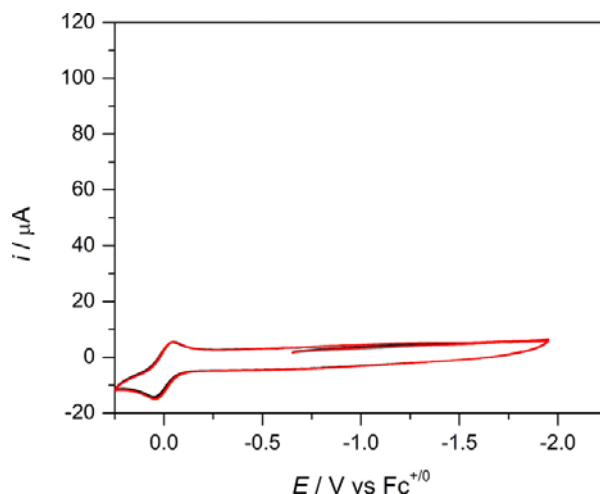


Figure 5.4 Cyclic voltammogram of a 0.5 mM **2** showing no change in behavior as NaOTs concentration is varied from 1 mM (black) to 25 mM (red). Overlapping traces in gray represent 2.5, 5, and 12.5 mM NaOTs.

Increasing the acid concentration from 5 mM to 12.5 mM triggers the appearance of a catalytic wave that grows from the irreversible feature at -1.85 V. As the acid concentration is doubled from 12.5 mM to 25 mM, the current density also doubles. At high acid concentration, the voltage window was extended out to -2.15 V to demonstrate that the current response maintains a peak maximum throughout the addition of acid. This behaviour suggests that the electrocatalytic reduction of protons is limited by diffusion to the electrode surface.¹¹⁴

Since molybdenum is pentacoordinate in this ligand system, there was concern the appearance of current was due to the binding of the tosylate anion in the open position *cis* to the terminal oxo. To investigate this possibility, a control experiment in which the CV scan is performed using sodium tosylate shows no such catalytic wave, thus confirming that the redox chemistry requires the addition of protons, and is not due to binding of a sixth ligand (Figure 5.4).

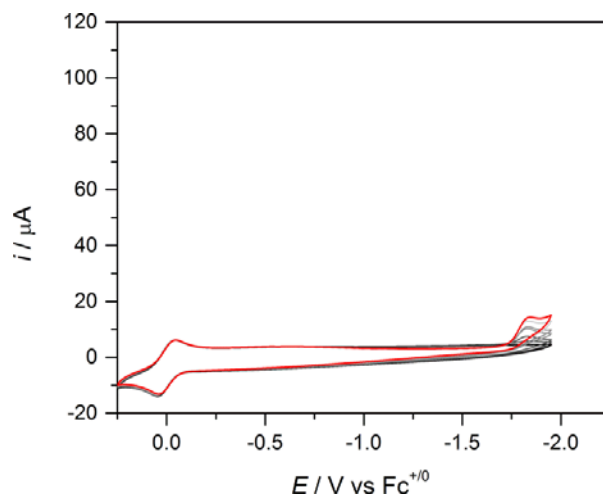


Figure 5.5 Background cyclic voltammetry of a TsOH solution in DMSO and electrolyte at a glassy carbon working electrode. The concentration of TsOH increases from 0 mM (black) to 50 mM (red) with intermediate concentrations 1, 5, and 10 mM shown in gray.

Performing electrolysis in the absence of catalyst **2** (Figure 5.5) with the same acid concentrations noted above does show a small background reaction on the glassy carbon working electrode. However, at 25 mM acid concentration, the current density at -1.85 V observed in the presence of **2** is 5 times greater than that measured in the absence of catalyst.

In order to interrogate the electronic structure of the catalytically active species, spectroelectrochemistry was performed using a custom-built optically transparent thin layer electrochemical (OTTLE) cell using a mercury gold amalgam mesh working electrode. Platinum and silver were the auxiliary and reference electrodes respectively. Figure 5.6 shows the evolution of the UV-vis spectrum over the course of a CV experiment with a scan rate of 10 mV/s. Spectra were recorded every 10 seconds, and arrows indicate the change in the absorption bands over time. Notably, the intensity of the MLCT band at 437 nm increases upon the cathodic sweep, indicating that molybdenum is reduced. This band then decreases upon the corresponding anodic scan.

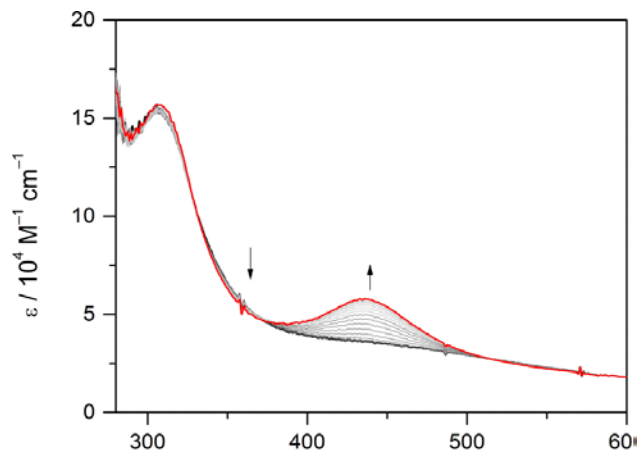


Figure 5.6 UV-Vis spectroelectrochemistry of 5 mM **2** in a solution of 0.1 M TBAPF₆ in DMSO with 1.5 mmol tosic acid during the cathodic scan of a cyclic voltammogram with a scan rate of 10 mV/s with a mercury-gold mesh amalgam working electrode. Spectra were recorded every 10 second.

The electrochemistry and spectroelectrochemistry elicit a proposed reaction mechanism in which the complex undergoes a one-electron, two-proton reaction, with protonation most likely occurring on the nucleophilic terminal oxo, followed by a one-electron reduction. The reductions both occur at the metal as evidenced by the growth of the MLCT band in the spectroelectrochemistry, and supported by the DFT calculation that shows large metal character of the LUMO, Figure 5.7 .

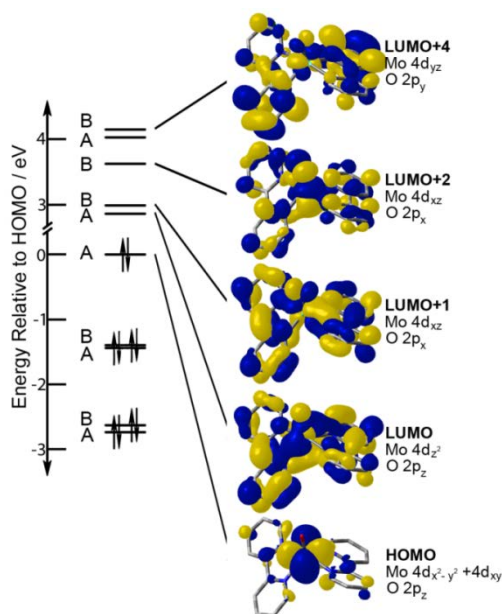


Figure 5.7 DFT of **2**, showing large metal character in LUMO.

The reduced complex then eliminates H₂, which is the rate-determining step as evidenced by the linear dependence of catalytic current on acid concentration at low acid concentrations (Figure 5.9).¹¹⁵ Hydrogen elimination could proceed in a similar fashion to the computationally proposed reductive cleavage of water and α-H abstraction on a molybdenum center.¹¹⁶ This proposed mechanism is shown in Figure 5.8.

This mechanism is consistent with the observations described above and with previous reports of similar complexes. In this catalytic cycle, step 4, the reductive elimination of hydrogen, is the rate determining step. The protonation step (step 1) will be governed by equilibria that determines the fraction of the complex that is in the doubly protonated Mo^{IV} form. As a result, the catalytic reaction is expected to obey Michaelis-Menton kinetics with the rate expression shown in Eq. (5-6).

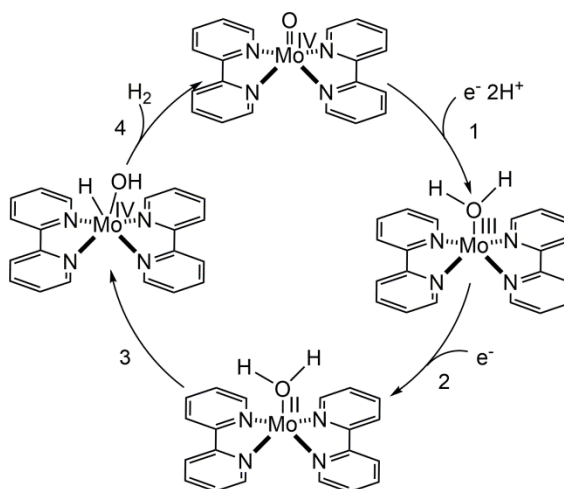


Figure 5.8 Proposed mechanism for reduction of H⁺ to H₂ by catalyst (2).

$$rate = \frac{k_3[H^+]^2}{\frac{k_{-1}+k_3}{k_1} + [H^+]^2} [Cat]_T = k_{obs}[Cat]_T \quad (5-6)$$

The equation for catalytic current, i_c , for cyclic voltammetry is given by Eq. (5-7) Where n is the number of electrons consumed in the catalytic cycle, F is the Faraday constant, $[cat]_T$ is the total or initial concentration of the catalyst, D is the diffusion coefficient of the catalyst, and k_{obs} is the observed rate constant for the particular catalytic reaction under consideration.

$$i_c = nF[cat]_T(Dk_{obs})^{1/2} \quad (5-7)$$

The derivation of this equation assumes the concentration of the substrate, in this case $[H^+]$, is sufficiently large that it remains constant at the initial value of the bulk solution. The value of n in Eq. (5-7) will be 2 because two electrons are consumed in the catalytic cycle, steps 1 and 2. Substitution of Eq. (5-6) into Eq. (5-7) gives Eq. (5-8)

$$i_c = nFAD^{1/2}[cat] \sqrt{\frac{k_3[H^+]^2}{\frac{k_{-1}+k_3}{k_1}+[H^+]^2}} \quad (5-8)$$

The relationship between the peak current, i_p , the catalyst concentration $[cat]$, and the sweep rate v is given by Eq. (5-9) for a reversible, one-electron wave.

$$i_p = 0.446FA[cat]_T(FvD/RT)^{1/2} \quad (5-9)$$

In Eq. (5-9), R is the ideal gas constant, T is the absolute temperature, and v is the scan rate. Dividing Eq. (5-8) by Eq. (5-9) gives Eq. (5-10)

$$\frac{i_c}{i_p} = \frac{2}{0.4463} \sqrt{\frac{RT}{Fv}} \sqrt{\frac{k_3[H^+]^2}{\frac{k_{-1}+k_3}{k_1}+[H^+]^2}} \quad (5-10)$$

At low acid concentrations, Eq. (5-10) indicates a linear dependence will be observed for i_c/i_p , as observed experimentally in Figure 5.9 (0-40 mmol TsOH). The linear dependence at low acid concentrations indicates the reaction is second-order in acid as expected for the reduction of two protons into hydrogen. At these low concentrations, the observed rate constant is a composite of constants for several elementary steps. At high acid concentrations Eq. (5-10) simplifies to Eq. (5-11) and the observed rate constant corresponds to the simple unimolecular elimination of H_2 for step 4.

$$\frac{i_c}{i_p} = \frac{2}{0.4463} \sqrt{\frac{RTk_3}{Fv}} \quad (5-11)$$

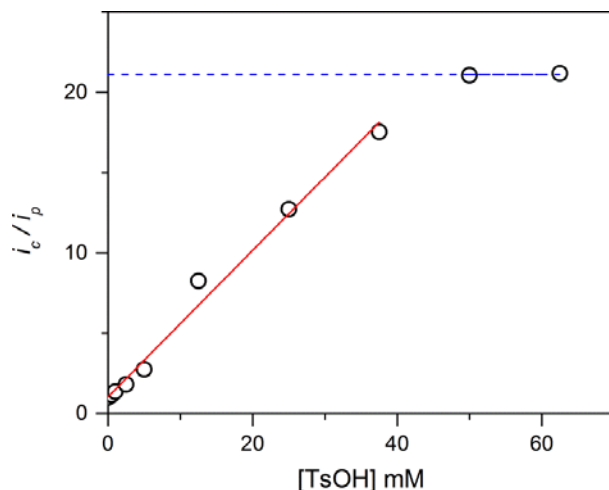


Figure 5.9 i_c/i_p vs. acid concentration of 0.1 mM **2** in a 0.1 M solution of TBAPF₆ in DMSO.

Using Eq. (5-11) a rate constant of 43 s^{-1} can be obtained for step 4 from the acid independent region of the plot shown in Figure 5.9 (50 – 60 mmol TsOH). This number represents the number of times a catalyst molecule produces a molecule of H₂ in a second, or the turnover frequency of this catalyst under these conditions. Calculating the rate at various catalyst concentrations shows a linear relationship between rate and catalyst concentration, indicating that the reaction is first order in **2** (Figure 5.10).¹¹⁷

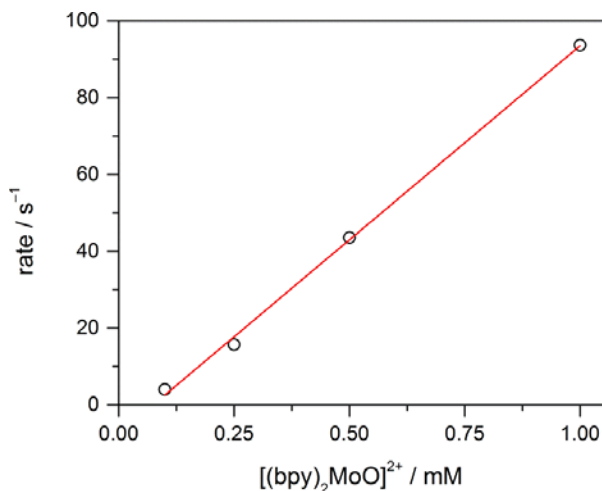


Figure 5.10 Rate of **2** in a solution of 0.1 M TBAPF₆ in DMSO as a function of the catalyst concentration.

With this understanding of the mechanism, controlled potential coulometry (CPC) was carried out at $-1.85\text{ V vs Fc}^{+/0}$ to probe the steady-state behavior of the reaction. Figure 5.11 shows that upon adding 100 mol-eq. of TsOH, the current density is nearly constant over the first 3 hours with a linear increase in charge passed as a function of time, indicative of a catalytic reaction occurring.

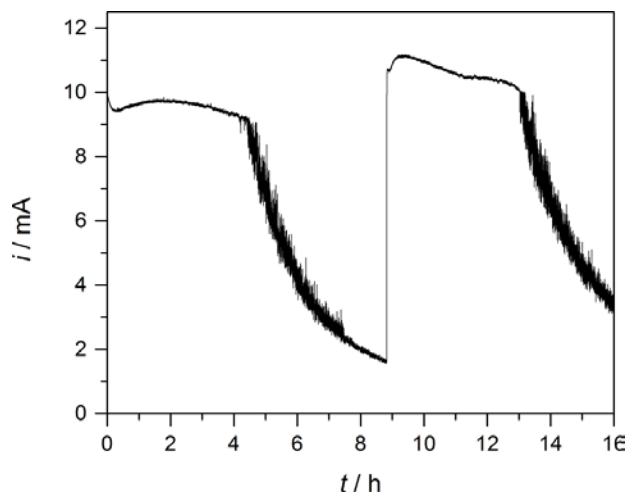


Figure 5.11 Bulk electrolysis of 0.5 M **2** in solution of 0.1 M TBAPF₆ and 50 mM TsOH in DMSO. Electrolysis was done at a potential of $-1.8\text{ V vs. Fc}^{+/0}$ with a carbon felt working electrode, platinum mesh counter electrode and SCE reference electrode.

As the TsOH concentration goes to zero, the current drops, as expected. However, adding another 100 mol-eq. TsOH results in an immediate recovery of catalytic activity. Similarly, controlled potential coulometry with MoO₂(acac)₂ and (**1**) at $-1.85\text{ V vs Fc}^{+/0}$ show that these synthetic intermediates have significantly slower reaction rates and stabilities, shown in Figure 5.12.

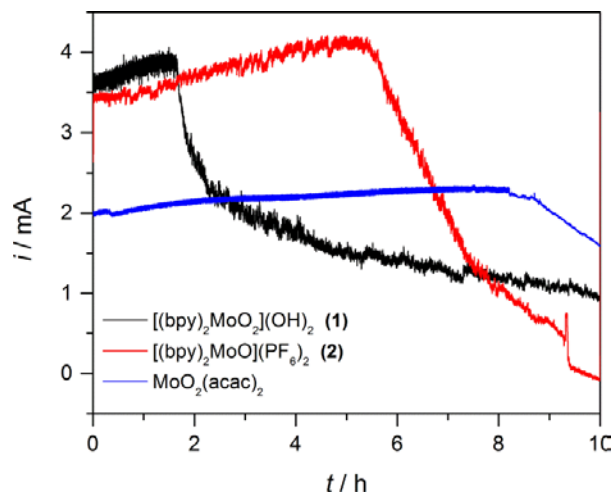


Figure 5.12 Bulk electrolysis of 0.5 mM **1** (black), $\text{MoO}_2(\text{acac})_2$ (blue), and **2** (red) in solution of 0.1 M TBAPF_6 and 50 mM TsOH in DMSO . Electrolysis was done at a potential of -1.8 V vs. $\text{Fc}^{+/0}$ with a carbon felt working electrode, platinum mesh counter electrode and SCE reference electrode.

Hydrogen gas evolution is monitored in a separate experiment in which the cell is connected to an in-line mass spectrometer. Figure 5.13 plots the rate of H_2 evolution over a 3 h experiment. In reporting our results, the background reaction on the glassy carbon has been subtracted such that the reported yields correspond only to those observed under homogeneous conditions.

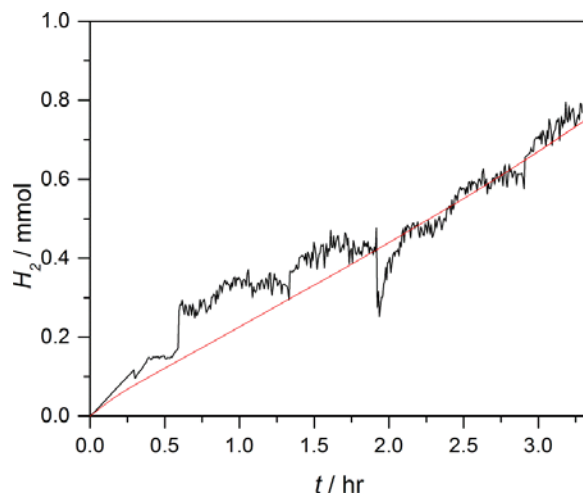


Figure 5.13 Hydrogen evolution over a 3 hour electrolysis of 0.5 mM **2** in a solution of 0.1 M TBAPF_6 and 100 mM TsOH in DMSO . Electrolysis was done at a potential of -1.8 V vs. $\text{Fc}^{+/0}$ with a carbon felt working electrode, platinum mesh counter electrode and SCE reference electrode. The red line shows the expected hydrogen evolution based on the charge passed during electrolysis.

The red line in Figure 5.13 gives the amount of hydrogen expected based on the current passed during electrolysis, the experimental and theoretical show good agreement suggesting all the current generated is used for the desired reaction. The turnover number (TON) over the 3 hour CPC was 40, establishing a catalytic reaction.

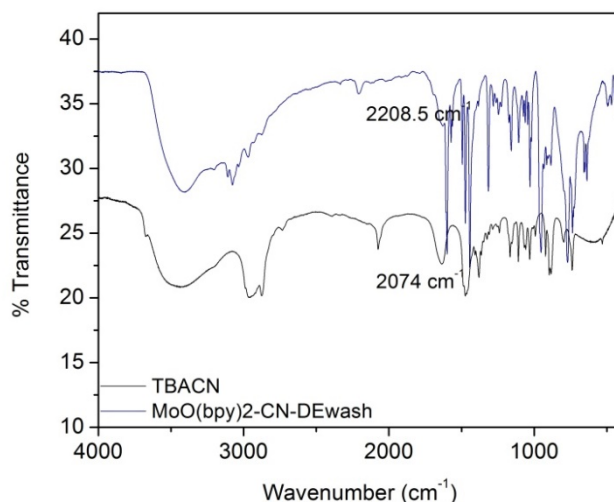


Figure 5.14 Infrared spectrum of tetrabutylammoniumcyanide (gray) and $[(bpy)_2MoO_2CN](PF_6)_2$ (**3**) (red). The $C\equiv N$ vibrational stretches for the bound and unbound cyanide are noted.

In an effort to lower the overpotential required for this catalyst, complex **2** was stirred in a solution of tetrabutylammonium cyanide ((TBA)CN). IR spectra of isolated complex **3** shows a shift in the CN stretch to 2208 cm^{-1} (Figure 5.14), suggesting the binding of CN to the position trans to the terminal oxo. There is also an increase in the metal-oxo stretching frequency, to 955 cm^{-1} , signifying the weakening of this bond as would be expected with the addition of a π -backbonding ligand. Electrochemical characterization of this complex, Figure 5.15, shows that upon adding TsOH, two irreversible couples appear at -1.2 and $-1.5\text{ V vs Fc}^{+/0}$, an anodic shift of approximately 300 mVs. The control experiment with electrolysis of acid in the presence of (TBA)CN shows no appreciable current until $-1.75\text{ V vs Fc}^{+/0}$

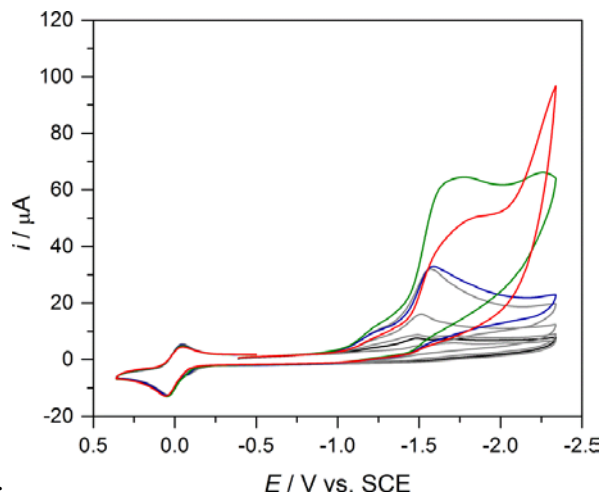


Figure 5.15 Cyclic voltammogram of a 0.5 M solution of **3** in DMSO containing 0.1 M Bu_4NPF_6 using a scan rate of 50 mV/s with a 1 mm diameter glass carbon working electrode. The concentration of TsOH increases from 0 mM (black), 25 mM (blue) and 50 mM (green). Intermediate concentrations 0.5, 1, 2.5, 5, 12.5 mM are shown in gray with the final concentration of 62.5 mM shown in red.

The catalytic current increases with added acid until the concentration reaches 62.5 mM TsOH, in which case the current at -1.5 V decreases and a sharp increase in current is observed starting at -2.0 V. This change in current onset may be the result of a loss of the bound cyanide because of the higher acid concentration.

The decrease in overpotential is accompanied with decreased current, with complex **3** exhibiting a little over half the current of complex **2**. This lower current is also observed in the CPC at -1.5 V vs $\text{Fc}^{+/0}$ where upon the addition of 50 mol-eq or TsOH, the current density is nearly constant for the first 18 hours (Figure 5.16). As the concentration of TsOH drops, so does the current, but added aliquots of TsOH result in the immediate recovery of current.

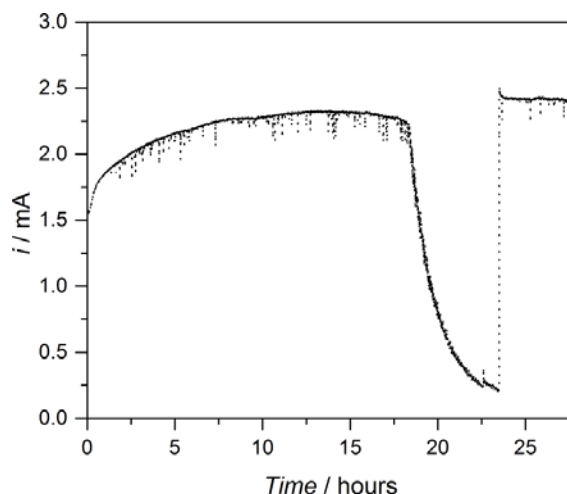


Figure 5.16 Bulk electrolysis of 0.5 M **3** in solution of 0.1 M TBAPF₆ and 50 mM TsOH in DMSO. Electrolysis was done at a potential of -1.8 V vs. Fc⁺⁰ with a carbon felt working electrode, platinum mesh counter electrode and SCE reference electrode.

5.3 Conclusion

In summary, a synthetically simple molybdenum-oxo complex, [MoO(bpy)₂], using a commercially available ligand set was fabricated for electrocatalytic reduction of protons in organic media. The catalyst exhibits a Faradaic efficiency of 95% at an applied potential of -1.85 V vs Fc⁺⁰. Although the simplicity of the synthesis is a benefit of this complex design, the absence of a fifth ligand results in lower performance than the pentadentate molybdenum oxo catalysts that have been previously published.¹⁰⁶ Adding cyanide results in some improvement of the catalyst, but the apparent loss of the ligand with higher acid concentrations, and lower activity make it unsuitable for a working catalytic system.

The relative simplicity of the complex lends itself toward designing a photocatalyst for H₂ evolution through simple modifications of the ligand scaffold, such as the addition of carboxyl, phosphate, or hydroxymate, allowing the binding the complex to a light absorbing metal oxide surface. Alternatively, the bipyridine could be switched to a bipyrimidine to allow for a photosensitizer such as ruthenium bipyridine to be used in conjunction with the catalyst. However, the low current density afforded of this catalyst suggests this may not be the best candidate for incorporation into photo catalytic systems.

5.4 Materials and Methods

5.4.1 General Considerations

Ammonium molybdate tetrahydrate, acetyl acetone, and 2,2'-bipyridyl were used as received. All solvents were reagent grade or higher purity, and were dried and distilled using standard methods under nitrogen. Tetrabutylammonium hexafluorophosphate was recrystallized from 200 proof ethanol. Tetrabutylammonium chloride was recrystallized from acetone and diethyl ether. Infrared spectra were measured on a Perkin–Elmer spectrum BX. NMR spectra were recorded on a Varian MR400 400 MHz spectrometer. Mass spectra data was collected on a Hiden Analytical HPR-20 QIC gas analysis system. The starting material bis(acetylacetonate) dioxomolybdenum(VI), $[\text{MoO}_2(\text{acac})_2]$, was prepared from ammonium molybdate tetrahydrate and acetyl acetone following the published procedure.¹¹⁸

5.4.2 Synthesis of bis(2,2'-bipyridine) dioxomolybdenum (VI) $[\text{MoO}_2(\text{bpy})_2][\text{OH}]_2$, (1)

The complex was prepared by a modification of literature methods.¹¹⁹ Bipyridine (3.12 g, 20 mmol) was dissolved in ethanol. $\text{MoO}_2(\text{acac})_2$ (3.26 g, 9.99 mmol). The solution was refluxed for 3 h and the precipitate filtered in air, washed with water and dried in vacuo yielding 2.1 g (47%) of white powder. FT–IR (KBr disk): 3078 (C–H), 1597(C=C), 1445 (C=C), 1055 (C–N), 913(Mo=O), 883 (Mo=O), 443, 420 cm^{-1} . ¹H NMR (400 MHz, DMSO): δ (ppm): 8.65 (d, 4H, J =), 8.36 (d, 4H, J =), 7.93 (t, 4H, J =), 7.43 (t, 4H, J =)

5.4.3 Synthesis of bis(2,2'-bipyridine) oxomolybdenum (IV) $[\text{MoO}(\text{bpy})_2][\text{PF}_6]_2$, (2)

PPh_2Me (365 mL, 1.705 mmol) was added to a solution of $\text{MoO}_2(\text{bpy})_2$ (300 mg, 0.682 mmol) in pyridine (40 mL). The reaction mixture was heated at reflux for 2 h. To the cooled solution was added $(\text{Bu})_4\text{N}(\text{PF}_6)$ (544 mg, 1.40 mmol) and the solution stirred at RT for 2 h. The reaction was filtered followed by suspension in cyclohexane and the solution concentrated. This was repeated until all residual pyridine was removed. The solid was then dried *in vacuo*. The product was isolated as a red–orange powder (208 mg, 43%). FT–IR (KBr disk): 3048 (C–H), 1608 (C=C), 1449 (C=C), 1071 (C–N), 946 (Mo=O), 457, 434 cm^{-1} . ¹H NMR (CDCl_3): δ (ppm): 7.68 (d, 4H), 7.38 (d, 4H), 6.94 (t, 4H), 6.78 (t, 4H).

5.4.4 Electrochemistry

Both cyclic voltammetry and controlled potential coulometry were performed using a CH Instruments Electrochemical Workstation 660. Cyclic voltammetry was carried out in a typical 3-electrode set-up employing a glassy carbon working electrode, a Pt mesh auxiliary electrode, and a saturated calomel reference electrode (SCE). DMSO is used as the solvent, and since these experiments are performed in non-aqueous conditions, ferrocene was added as an internal reference and all potentials are reported against the $\text{Fc}^{+/0}$ for comparison, noting that $0 \text{ V Fc}^{+/0} = +0.38 \text{ V SCE}$. $100 \text{ mM Bu}_4\text{NPF}_6$ is the electrolyte in all experiments and all sweeps are performed at a scan rate of 50 mV/s . Controlled potential coulometry was carried out in a double compartment cell separated by a fine frit at a potential of $-1.8 \text{ V vs Fc}^{+/0}$. Spectroelectrochemistry was done in a glass cell equipped with a mercury-gold amalgam working electrode; platinum counter electrode and silver reference electrode.

5.4.5 Mass Spectrometric analysis of electrolysis-cell headspace

A controlled potential electrolysis was conducted on a 0.5 mM solution of **(2)** in 40 mL of $100 \text{ mM Bu}_4\text{NPF}_6$ in DMSO in a gas-tight electrolysis cell at an applied potential of $-1.8 \text{ V vs Fc}^{+/0}$ for 3 hours. During electrolysis the production of H_2 was monitored with an inline mass spectrometer.

5.5 References

- 89 Bard, A. J., Fox, M. A. Artificial Photosynthesis: Solar Splitting of Water to Hydrogen and Oxygen, *Acc. Chem. Res.* **1995**, *28*, 141-145
- 90 Lewis, N. S., Nocera, Daniel G. Power the Planet : Chemical Challenges in Solar Energy Utilization, *PNAS*, **2006**, *103*, 15729-15735
- 91 Nocera, D. G. Living Healthy on a Dying Planet, *Chem Soc . Rev .* **2009**, *38*, 13-15
- 92 Lubitz, W.; Tumas, W. Hydrogen: An Overview, *Chem. Rev.* **2007**, *107*, 3900-3903
- 93 Abbas, H. F., Daud, W. M. A. W. Hydrogen Production by Methane Decomposition: A Review, *International Journal of Hydrogen Energy*, **2010**, *35*, 1160-1190
- 94 Peck, H. D.; San Pietro, A.; Gest, H. On the Mechanism of Hydrogenase Action, *Proc. Natl. Acad. Sci.* **1956**, *42*, 13-19
- 95 LeGall, J., Ljungdahl, P.O., Moura, I., Peck, H. D., Xavier, A. V., Moura J. J., Teixeira, M., Huynh, B. H., DerVartanian, D. V. The Presence of Redox-Sensitive

- Nickel in the Periplasmic Hydrogenase from *Desulfovibrio Gigas*, *Biochem. Biophys. Res. Commun.* **1982**, *106*, 610-616
- 96 Adams, M. W. The Structure and Mechanism of Iron-Hydrogenases, *Biochim. Biophys. Acta.* **1990**, *1020*, 115-145
- 97 Adams, M. W. W.; Stiefel, E. I. Biological Hydrogen Production: Not So Elementary, *Science*, **1998**, *282*, 1842-1843
- 98 Bolton, J. R. Solar Photoproduction of Hydrogen: A Review *Solar Energy*, **1996**, *57*, 37-50
- 99 Amouyal, E. Photochemical Production of Hydrogen and Oxygen from Water: A Review and State of the Art, *Solar Energy Materials and Solar Cells*, **1995**, *38*, 249-276
- 100 Hang, M.; Huynh, V.; Meyer, T. J. Proton-Coupled Electron Transfer, *Chem. Rev.* **2007**, *107*, 5004-5064
- 101 Eidem, P. K.; Maverick, A. W.; Gray, H. B. Production of Hydrogen by Irradiation of Metal Complexes in Aqueous Solutions, *Inorg. Chim. Acta.* **1981**, *50*, 59-64
- 102 Durham, B.; Dressick, W. J.; Meyer, T. J. *J. Chem. Soc. Chem. Comm.* 1970, 381-382
- 103 Koelle, U.; Infelta, P. P.; Gratzel, M. Kinetics and Mechanism of the Reduction of Protons to Hydrogen by Cobaltocene, *Inorg. Chem.* **1988**, *27*, 879-883
- 104 Jain, A., Lense, S., Linehan, J. C., Raugei, S., Cho, H., DuBois, D. L., Shaw, W. J. Incorporating Peptides in the Outer-Coordination Sphere of Bioinspired Electrocatalysts for Hydrogen Production, *Inorg. Chem.* 2011, *50*, 4073-4085
- 105 Gloaguen, F.; Rauchfuss, T. B. Small Molecule Mimics of Hydrogenases: Hydrides and Redox, *Chem. Soc. Rev.* **2009**, *38*, 100-108
- 106 Karunadasa, Hemamala; Chang, Christopher J.; Long, Jeffery R. A Molybdenum-Oxo Catalyst for Generating Hydrogen from Water, *Nature* **2010**, *464*, 1329-1333
- 107 Esslin, A. J.; Nocera, D. G. Hydrogen Production by Molecular Photocatalysis, *Chem. Rev.* **2007**, *107*, 4022-4047
- 108 Davies, E., S., Beddoes, R. L., Dollison, D., Dinsmore, A., Docra, A., Joulde, A. J., Wilson, C. R., Garner, C. D. Synthesis of Oxomolybdenum Bis(Dithiolene) Complexes Related to the Cofactor of the Oxomolybdoenzymes, *J. Chem. Soc., Dalton Trans.*, **1997**, 3985-3995
- 109 Stiefel, E. I. Chemical Keys to Molybdenum Enzymes, *J. Chem. Soc., Dalton Trans.*, **1997**, 3915-3923
- 110 Chen, G. J.-J., McDonald, J. W., Newton, W. E. Synthesis of Molybdenum (IV) and Molybdenum (V) Complexes using Oxo Abstraction by Phosphines. Mechanistic Implications, *Inorg. Chem.*, **1976**, *15*, 2612-2615

- 111 J. Dirand, L. Richanrd and R. Weiss., Preparation and Molecular Structure of Oxodihalogenobis(Dialkyldithiocarbamato)Molybdenum (VI) Complexes, *J. Chem. Soc. Dalton Trans.*, **1976**, 278-282
- 112 Reynolds, M. S., Berg, J. M., Holm, R. H. Kinetics of Oxygen Atom Transfer Reaction Involving Oxomolybdenum Complexes. General Treatment for Reaction with Intermediate Oxo-Bridged Molybdenum (V) Dimer Formation, *Inorg. Chem.*, **1984**, 23, 3057-3062
- 113 Kanagavel, D., Krishnan, C. N., Syntheses and Characterization of Doubly-Bidentate bis(Carboxy-amide) Complexes of Oxomolybdenum (IV), *Transition Met. Chem.*, **1996**, 21, 570-572
- 114 (a) Savèant, J. M., Su, K. B. Homogeneous Redox Catalysis of Electrochemical Reaction. Part VI. Zone Diagram Representation of the Kinetics Regimes, *J. Electroanal. Chem.*, **1984**, 171, 341-377 (b) C. P. Andrieux, C. Blocman, J. M. Dumas-Bouchiat, F. M'Halla and J. M. Savèant, Homogeneous Redox Catalysis of Electrochemical Reactions. V. Cyclic Voltammetry, *J. Electroanal. Chem.*, **1980**, 113, 19-29
- 115 A. M. Appel, D. L. DuBois, and M. R. DuBois, Molybdenum-Sulfur Dimers as Electrocatalysts for the Production of Hydrogen at Low Overpotentials, *J. Am. Chem. Soc.*, **2005**, 127, 12717-12726
- 116 Li, J., Yoshizawa, K. Computational Evidence for Hydrogen Generation by Reductive Cleavage of Water and α -H Abstraction on a Molybdenum Complex, *Angew. Chem. Int. Ed.*, **2011**, 50, 11972-11975
- 117 (a) Savèant, J. M., Vianello, E. Potential-Sweep Chronoamperometry: Kinetic Currents for First-Order Chemical Reaction Parallel to Electron-Transfer Process (Catalytic Currents), *Electrochim. Acta*, **1965**, 10, 905-920 (b) Nicholson, R. S., Shain, I., Theory of Stationary Electrode Polarography. Single Scan and Cyclic Methods Applied to Reversible, Irreversible, And Kinetic Systems, *Anal. Chem.* **1964**, 36, 706-723 (c) Yang, J. Y., Bullock, R. M., Shaw, W. J., Wamley, B. T., Frazee, K., Dubois, M. R., DuBois, D. L. Mechanistic Insights in to Catalytic H₂ Oxidation by Ni Complexes Containing a Diphosphine Ligand with a Positioned Amine Base, *J. Am. Chem. Soc.*, **2009**, 131, 5935-5945 (d) Goodman, A.J., Nelson, E., Bartlett, B. M. Homogeneous Hydrogen Evolution Catalyst Assessment and Design towards the Development of a Photocatalytic Molecular Device. B.S. Honors Thesis, University of Michigan, April 2012.
- 118 Chen, G. J.-J., McDonald, J. W., Newton, W. E. Synthesis of Molybdenum(IV) and Molybdenum(V) Complexes using Oxo Abstraction by Phosphines. Mechanistic Implications, *Inorg. Chem.*, **1976**, 15, 2612-2615
- 119 Khojasteh, R. R., Saremi, S. L., Ahmadzadeh, M. Synthesis and Characterization of Dioxomolybdenum (VI) Complexes with 1,10-Phenanthroline and 2,2'-Bipyridyl, *Asian Journal of Chemistry* **2011**, 8, 3769-3770

CHAPTER 6

Perspectives and Conclusion

6.1 Introduction

This thesis focuses on establishing a deeper understanding in electrolyte composition and its connection to electrochemical performance and how that connection can be used to guide the advancement of novel Mg electrolyte systems. Although some understanding and connections between the two has been made, many questions remain in the electrolyte systems that have been established. Some questions can be answered using similar techniques presented in this dissertation, others will require more in-depth and fundamental inquiries, which are described in the sections below, to fully analyze and move forward.

6.2 Perspectives

6.2.1 Air Stable Electrolyte Systems

The concept of an air stable Mg electrolyte was first published by Hirano.¹²⁰ The improvements and solution characterization of this system presented in Chapter 2 shows progress based upon the incorporation of electron withdrawing groups into the ligand structure of the electrolyte. Although the electronics of improving these electrolytes is fairly straight forward and easily predicted, the role of alkyl substitution, hinted at in Chapter 2, is not so easy to understand but may prove useful in expanding the electrochemical window of this system. The combination of electron withdrawing substituents in the para positions and alkyl substituents in ortho or meta positions may provide a larger stability window than could be predicted *a priori*. The approach of incorporating electron withdrawing groups may also work with other ligand structures, or

may be used to improve the oxidation potential of the most common solvents (glymes) used for Mg electrolyte systems which have stability windows around 3.5 V vs $\text{Mg}^{0/2+}$.

Although the use of alkoxide/ phenoxide ligands in place of the traditional alkyl (Grignard-derived) Lewis bases does help decreased reactivity to air, it does not impart actual air stability, in which no alteration in the electrochemical characteristics upon exposure is expected. The change in the performance, and NMR spectra could suggest the reaction upon air and moisture exposure is simply slowed down. One report showed that after air exposure, addition of starting materials brings the electrolyte back to pre-exposure performance.¹²¹ Although the addition of starting materials has not been tried in the phenoxide electrolyte systems in this thesis, this approach does not address the underlying concern, the reaction with air and moisture.

Fabricating an electrolyte with actual air stability will help in the construction of Mg-O₂ and Mg-air battery systems, which promises a high theoretical energy density (6.8 kWh/kg). Interest in Mg-air systems has increased recently, although they experience similar issues as Li-air systems.¹²² The ambition of creating a Mg-air system currently appears to be less likely than the Li counterpart, indeed the only rechargeable system reported relies on the incorporation of an I₂/DMSO couple.¹²³ The quest to design a rechargeable Mg-air system may be assisted by the formulation of an electrolyte that shows long term stability (months to years) in air and moisture at high oxidation potentials, thus preventing any side reactions, even minor ones, which can interfere with the desired electrochemical reaction.

6.2.2 Non-corrosive Electrolyte Systems

If the goal of a higher voltage cathode is to be achieved, an electrolyte that shows stability to those potentials is required. A few electrolytes showing high stability have been reported, but the high potentials are reported in cyclic voltammogram conditions usually using a Pt working electrode. Although initial electrolyte performance testing on Pt ensures the electrochemistry observed is strictly that of the electrolyte, given the inert nature of platinum, moving to a less inert metal will often show a much lower oxidation potential due to metal corrosion as discussed in chapter 3.

Scrutinizing the performance of a cathode is carried out in much the same way, with cyclic voltammograms of thin cathodes on stable conductive surfaces such as fluorinated tin oxide or metal films. Although these simple electrochemical tests are necessary, they do not inform how these cathode materials will perform under full battery cycling conditions. Attempts to test the cathode material in a full battery will often result in overcharging which can be a result of a number of parasitic reactions such as instability of the cathode or electrolyte. For magnesium electrolytes, another cause of overcharging is the corrosion of the stainless steel casing by chloride in the electrolyte solution. This overcharging will often occur at potentials lower than would be predicted from CV scans using stainless steel working electrodes. The lower observed potential is due to the slower kinetics on stainless steel preventing the true oxidation potential from being observed in the relatively fast time scale of a CV experiment.

Chapter 3 shows that the replacement of the chloride rich aluminum chloride Lewis acid with the aluminum phenoxide results in a marked decrease in the corrosion of stainless steel. Some corrosion was still observed after extended electrolysis due to incomplete removal of all sources of chloride. Although the present chloride did not appear to interfere with cycling a battery at potentials as high as 3.5 V vs $\text{Mg}^{2+/0}$, attempting to cycle at potentials closer to the apparent stability may show overcharging. This cycling was done in the presence of a Li-ion salt which may affect the reactivity of the chloride anions, although there is no evidence to suggest this is the case.

Future generations of electrolytes should focus on systems that exclude all halides to ensure stainless steel corrosion is no longer a complication. Work in this area includes magnesium with alkoxides and phenoxides, amido, and borohydride ligands. Although these electrolytes do not contain chloride, they often suffer in terms of conductivity, current density as well as low oxidation potentials. Adding a secondary electrolyte, often AlCl_3 , results in the improvement of the electrolyte performance but again incorporates chloride. For $\text{Mg}(\text{BH}_4)_2$, adding LiBH_4 greatly improves the current density and conductivity, but has little effect on the oxidative stability. Nevertheless improved anodic stability was observed when stainless steel was used as the working electrode due to slower kinetics of borohydride oxidation.¹²⁴ Moving forward, incorporation of a ligand

system with much higher oxidative stability while retaining the high current density, kinetics, and conductivity of the borohydride system would be a great advancement.

6.2.3 Electrolyte/ Electrode Interfaces

The inability of magnesium to deposit and strip from simple salts in common organic solvents such as acetonitrile and carbonate based solvents is commonly attributed to an ionically passivating layer that is formed on Mg metal. Despite this oft quoted reason, experimental evidence for this conclusion has yet to surface. The ability to image and map the composition of the electrode surface will be invaluable for understanding this phenomenon as well as understanding why the phenyl-based passivation SEI layer explored in Chapter 4 gives rise to a greater anodic stability. This electrolyte system appears to be the first reported system with a passivation layer formed *in situ* that continues to show some Mg^{2+} conduction. Characterization of how Mg ions are prevented from leaving the surface will prove useful in grasping how the surface chemistry of Mg-ion electrolytes have prevented Mg-ion efficiencies from reaching the same efficiency as their Li-ion counterparts. Techniques such as Atom Probe Tomography will also provide insight into how passivation layers maybe applied for further augmentation of higher voltage Mg-ion batteries.

6.2.4 Solution Speciation and Synthetic Approaches

One of the goals of this thesis was to increase the connection between electrochemical performance and the chemical species in solution. Mg-ion electrolyte chemistry is considerably more complex than Li-ion, mostly due to the fact that a simple Mg salt does not have all required electrochemical characteristics to perform as an electrolyte (mainly reversible Mg^0 deposition and high electrochemical oxidation potentials). Although simple Li salts, most notably LiPF_6 , do show these properties, working Mg electrolytes are usually comprised of Grignard based Lewis bases and aluminum Lewis acids. These mixtures undergo complex equilibria that make characterization of the solution as discussed in chapters 2 and 3. Also, as previously mentioned the characterization of the Mg species, the complexes of most interest, is quite difficult. This difficulty is partially due to its high quadrupole moment, which makes

distinguishing species via NMR spectroscopy infeasible. One way to circumvent the struggle of complex characterization is to synthesize discrete molecular complexes. This approach has been attempted, and suggested previously as a continuation of the borohydride based systems.¹²⁵ To expand upon the systems presented in this thesis, the target complexes would be $\text{Mg}[\text{Al}(\text{OPh}_4)]_2$ and $\text{Mg}[\text{Al}(\text{Ph}_4)]_2$. These independently synthesized and isolated complexes should allow for a detached Mg^{2+} solvated with solvent molecules creating a contact ion pair with the organo-aluminum anions. This complex should not only help facilitate Mg deposition and stripping kinetics, but also allow for exploring other solvents for the electrolyte.

6.3 Conclusion

The exploration of both the electrolyte and cathode materials will be necessary for Mg-ion technology to reach a level that will allow for replacement of Li-ion batteries or even commercial application. The first breakthrough in cathode materials, Mo_6S_8 , is now considered the standard for appraising electrolyte performance. However, the variance in performance and purity from batch to batch make it not only an unlikely target for commercial application, but also a bane for fundamental researchers. The conception of a cathode material with the best properties of the Chevrel cathode with the reproducibility common to Li cathode materials will open the door for commercial applications.

Magnesium suffers from a somewhat perplexing inability to reach the same efficiency of its lithium cousin. Although complete Li battery systems have reached essentially 100% coulombic efficiency, Mg electrolytes themselves have yet to pass 98% efficiency. Obtaining an understanding of why Mg ion chemistry suffers from this lower efficiency will be crucial for the future of commercial Mg-ion batteries, which will require a very high efficiency to guarantee a suitable battery lifetime.

One route to improving the efficiency is the exploration of novel Mg electrolytes with the goal of increasing the efficiency of the Mg deposition and stripping. A second approach is the careful interrogation of the chemistry taking place at the electrolyte-electrode interface. I believe this approach will be the most beneficial to the future of the Mg-ion battery community. Having a better understanding of the interfacial chemistry will give insight into the reasons behind the comparatively low efficiency of Mg ion

stripping and will enable the determination of whether this is a fundamental obstacle for Mg or allow for a targeted approach in electrolyte chemistry to solve this hindrance. If Mg-ions battery technology is ever to replace or compete with the current Li-ion technology greater exploration and creative solutions and ideas will be required to address the current limitations of magnesium-ion technology.

6.4 References

- 120 Wang, F., Guo, Y., Yang, J., Nuli, Y., Hirano, S. A Novel Electrolyte System without a Grignard Reagent for Rechargeable Magnesium Batteries, *Chem. Commun.*, **2012**, *48*, 10763-10765
- 121 Guo, Y., Zhang, F., Yang, J., Wang, F., Nuli, Y., Hirano, S. Boron-based Electrolyte Solutions with Wide Electrochemical Windows for Rechargeable Magnesium Batteries, *Energy Environ. Sci.*, **2012**, *5*, 9100-9106
- 122 a.)Cheng, F., Chen, J. Metal-Air Batteries: from Oxygen Reduction Electrochemistry to Cathode Catalysts, *Chem. Soc. Rev.*, **2012**, *41*, 2172-2192 b.) Zhang, T., Tao, Z., Chen, J. Magnesium-Air Batteries: From Principle to Application, *Mater. Horiz.*, **2014**, *1*, 196-206
- 123 Shiga, T., Hase, Y., Kato, Y., Inoue, M., Takechi, K. A Rechargeable Non-Aqueous Mg-O₂ Battery, *Chem. Commun.*, **2013**, *49*, 9152-9154
- 124 Mohtadi, R., Matsui, M., Arthur, T. S., Hwang, S. J. Magnesium Borohydride: From Hydrogen Storage to Magnesium Battery, *Angew. Chem. Int. Ed.*, **2012**, *51*, 9780-9783
- 125 Carter, T. J., Mohtadi, R., Arthur, T., Mizuno, F., Zhang, R., Shirai, S., Kampf, J. W. Boron Cluster as Highly Stable Magnesium-Battery Electrolyte, *Angew. Chem. Int. Ed.*, **2014**, *53*, 3173-3177